2018-03-26

Photonic Strategies for Bioimaging and Modulation of Biological Systems

Lorenzo Sansalone
University of Miami, lo.sansalone@gmail.com

Recommended Citation

Sansalone, Lorenzo, "Photonic Strategies for Bioimaging and Modulation of Biological Systems" (2018). *Open Access Dissertations*. 2020.
https://scholarlyrepository.miami.edu/oa_dissertations/2020

UNIVERSITY OF MIAMI

PHOTONIC STRATEGIES FOR BIOIMAGING AND MODULATION OF BIOLOGICAL SYSTEMS

By

Lorenzo Sansalone

A DISSERTATION

Submitted to the Faculty
of the University of Miami
in partial fulfillment of the requirements for
the degree of Doctor of Philosophy

Coral Gables, Florida
May 2018

UNIVERSITY OF MIAMI

A dissertation submitted in partial fulfillment of
the requirements for the degree of
Doctor of Philosophy

PHOTONIC STRATEGIES FOR BIOIMAGING AND MODULATION OF BIOLOGICAL SYSTEMS

Lorenzo Sansalone

Approved:

________________ Françisco M. Raymo, Ph.D. Professor of Chemistry	________________ Roger M. Leblanc, Ph.D. Professor of Chemistry
________________ James N. Wilson, Ph.D. Associate Professor of Chemistry	________________ Guillermo Prado, Ph.D. Dean of the Graduate School
________________ James D. Baker, Ph.D. Professor of Biology	

SANSALONE, LORENZO (Ph.D., Chemistry)

Photonic Strategies for Bioimaging and Modulation of Biological Systems (May 2018)

Abstract of a dissertation at the University of Miami.

Dissertation supervised by Professor Françisco M. Raymo.
No. of pages in text. (129)

The last two decades have seen how the development of photoactivatable fluorophores significantly implemented imaging and spectroscopic techniques applied to the "biological world".[1] In fact, molecules that switch from a nonemissive to an emissive state upon illumination at an activating wavelength (λ_{ac}) and then emit after irradiation at an exciting wavelength (λ_{exc}) opened a new field of research and, beside the generation of super resolved subdiffracted images, they permit the monitoring of dynamic processes in real time.[2] In the context of our work, an oxazine-based molecular switch has been designed to generate photoactivatable fluorophores suitable for bioimaging. The second and third chapters of this thesis focus on the development of a new class of NIR photoactivatable fluorophores based on a 2-Nitrobenzyl photoswitch. The best representative of the series has been tested to monitor dynamic cellular processes in Drosophila melanogaster embryos. In the last chapter, the very same phototrigger has been used to generate a light activatable version of Diazepam (Prodrug of Diazepam) that was tested on the locomotor behavior of Zebrafish larvae.

ACKNOWLEDGMENTS

First, I must thank my research advisor Dr. Françisco M. Raymo for guiding me through these intense years of research. His constant advice, incredible knowledge and *modus operandi* have been an extremely valuable lesson for my professional future. I'm immensely grateful for the chance he gave me to become a scientist under his name.

A special thank goes to Dr. Roger M. Leblanc: the first person that really cared about me once I started my "Ph.D. adventure" at the University of Miami. His invaluable scientific approach and incredible wisdom lessons have shaped my personality over these years from being an impulsive student to a methodic learner. Once again, I am extremely grateful.

I want to thank Dr. James Baker for his precious hints on Confocal Microscopy, for having taught me how to work properly with Drosophila melanogaster and for all the scientific knowledge he shared with me over these years.

I want to thank Dr. Julia Dallman, a truly wonderful person. I never met anyone with such a great positive attitude. I'm very grateful for all the hints she gave me on how to work with Zebrafish and for all the many conversations we had, about science and, most importantly, about life.

I want to thank Dr. Burjor Captain for the many things I learned from him since the first few months of graduate classes at the University of Miami. An amazing Professor.

Moreover, I want to thank him for all the time and care he spent in solving my crystal structures.

I want to thank Dr. James Wilson for the few but valuable moments he spent sharing his unique scientific knowledge with me.

I would like to thank Dr. Marc Knecht, Dr. Leslie Knecht, Dr. Orlando Acevedo, Dr. Thomas K. Harris, Dr. Tegan Eve for all the times I had the opportunity to interact with them and learn something.

I must express my gratitude to my current and ex colleagues Mercedes Mazza, Francesca Cardano, Sicheng Tang, Yiqun Zhou, Dr. Yang Zhang, Dr. Ek Raj Thapaliya, Dr. Zhili Peng, Dr. Jaume Garcia-Amorós, Dr. Janet Cusido, Dr. Shanghao Li and Dr. Eduardo Veliz for their precious help and the good times spent together.

Finally and most importantly, I would like to thank my friends, the persons that were the real backbone of my adventure at the University of Miami: Anthony Cauley, Catherine Munro and Brian Doherty. There are not enough words to describe how grateful I am for all the good, bad and crazy moments spent together.

And the last special thank goes to the staff of the Department of Chemistry at the University of Miami. Thanks to Raul Hernandez, Ana Parr, Noel Urbina, Juana Hernandez and Nyisha Alexander!

TABLE OF CONTENTS

LIST OF FIGURES

LIST OF TABLES

Chapter 1: Introduction: What Do You Need to Know?

1.1 Fluorescence: Principles and New Trends

Fluorescence imaging is an invaluable tool to investigate biological processes[3-4] and shine light on poorly understood and critical pathological conditions,[5] such as cancer[6-7] and neurological disorders.[8-9] While various forms of luminescence have been used for biological applications,[10-12] it's without a doubt that, among photoluminescence techniques, fluorescence is the most versatile and, most importantly, tunable for the purpose. Small molecules,[13] macromolecules[14-15] and nanoparticles[16] have all been used for biological applications and, while a never-ending debate is ongoing about which is the best, a smart scientist can certainly take advantage of the individual benefits of each, such as the simplicity of genetic expression in the case of fluorescent proteins, the lack of interaction of nanoparticles with cellular proteins and the wide tunability and functionalization potential for small organic molecules. Regardless of the chemical nature of the emitter and/or the wavelength of the light absorbed, fluorescence is a univocal phenomenon by definition and schematically represented by the Jablonski Diagram below (Figure 1.0).[17] Usually, upon absorption of the exciting radiation by a fluorophore (**A**, $h\nu$), an electron in the ground state (S_0) is excited to higher energetic levels (i.e. S_1, S_2, $S_{3...}$). Following internal conversion (**IC**), where the electron reaches the lowest vibrational level of the S_1 state, the light can be emitted in the form of fluorescence (**F**, $h\nu^I < h\nu$) with the deexcited fluorophore repopulating higher vibrational levels of the ground state to quickly reach thermal equilibrium. Additionally, the electron could return to S_0 through a non-radiative decay (**ND**) or fully thermal dissipation of energy. To keep in mind is the spin state of the electron in the excited state: while fluorescence is a spin allowed process, where the excited electron possesses opposite spin compared to its original counterpart in the ground state, phosphorescence is a spin forbidden process. In fact, an intersystem crossing (**ISC**) is required for the electron to invert its spin and generate a triplet state from which light can be emitted in the form of phosphorescence (**P**). This important difference is reflected in the timescale of the two phenomena, fluorescence emission rates are on the order of 10^9 s^{-1} while phosphorescence emission occurs on the order of 10^0 -10^3 s^{-1}. Many other important and fundamental photophysical phenomena can be represented and explained through a Jablonski diagram but, because the description of such would deviate from the main purpose of this thesis, the reader is invited to find the exquisite details of these processes in the many reviews and books published over the years.[18-25]

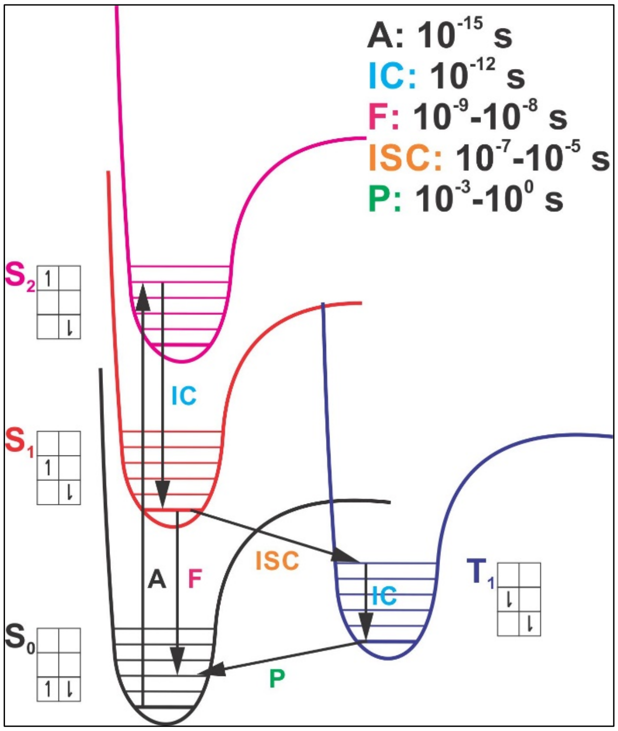

Figure 1.0. A schematic representation of a Jablonski diagram showing the ground state S_0, two singlet excited states S_1 and S_2 and a triple state T_1 with the relative photophysical transitions (A: Absorption, IC: Internal Conversion, F: Fluorescence, ISC: Intersystem Crossing, P: Phosphorescence).

Since the first applications of the fluorescence phenomena to the biological world,[26] their impact in the clinical world has been key for the diagnosis of many pathological conditions[27] and for the imaging of biological specimens that culminated in 2014 with the assignment of the Nobel Prize in Chemistry to Eric Betzig, Stefan Hell and William Moerner for the development of super-resolved fluorescence microscopy.[28] Nonetheless, fluorescence keeps channeling itself in delightful ways into further applications. In fact, surgeons can now operate guided by the light of fluorescent agents targeting specific proteins or cell parts.[29] Despite many advances, imaging of biological tissues is challenging: the presence of light sensitive biomacromolecules, the intrinsic fluorescence of DNA and/or protein residues and physical barriers impermeable to light complicate the whole scenario. The wavelength (λ) of the light used is thus critical for success. While many molecules, naturally occurring or easily synthesized, are absorbers and emitters in the Ultraviolet region (UV, $100<\lambda<400$ nm), this light remain a poor choice for the following reasons: i) It damages the biological specimen, creating irreversible damage to DNA [30-31] ii) Aromatic amino acid residues in proteins and many other intrinsic chromophores absorb and emit UV light, generating an autofluorescence background[32] iii) Photon penetration in living tissue is highly dependent on its components and on the nature of the light used.[33-34]

These limitations resulted in many efforts that lead to the development of Near-Infrared (NIR) probes for in-vivo imaging.[35] NIR light (650-900 nm) causes minimal photo-damage to biological tissues, has a deeper tissue penetration compared to UV and visible light and doesn’t interfere with the emission of intrinsic fluorophores leading to a significantly reduced sample autofluorescence.[36-37] (Figure 1.1)

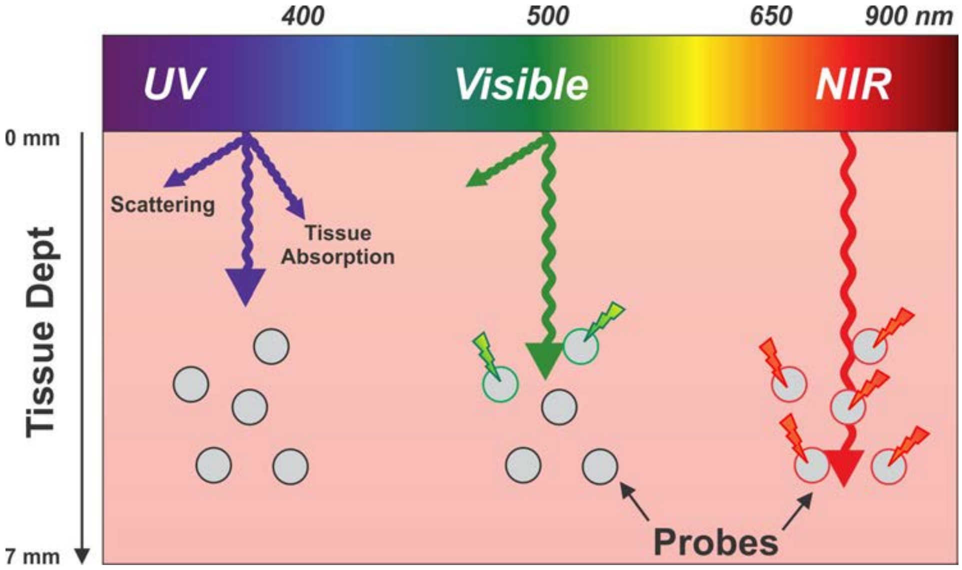

Figure 1.1. Schematic representation showing how NIR light penetrates deeper into biological tissues leading to the activation of more fluorescent probes compared to UV and Visible light

Classical approaches to bathochromically tune the probe absorption are to extend the conjugation of the molecule π system or to create push-pull structures (D-A fluorophores).[38] Although both methods effectively reduce the HOMO-LUMO gap,[39] the conformational freedom gained by the molecule often overweighs the decrease in orbitals energy and new non-radiative pathways predominate over the fluorescence radiative process. Thus, NIR probes generally have optimal absorption/emission profiles with very low quantum yields.

Although many excellent NIR probes have been developed, these emitters are conventional fluorophores and it is still very challenging to control the spatial and temporal distribution of fluorescence in biological samples. With the development of photoactivatable fluorophores, it is possible to implement new imaging and spectroscopic schemes. In fact, molecules that switch from a nonemissive to an emissive state upon illumination at an activating wavelength (λ_{ac}) and then emit after irradiation at an exciting wavelength (λ_{exc}

in Figure 1.2), opened a new field of research and, beside the generation of super resolved subdiffracted images,[40] they permit the monitoring of dynamic processes in real time.[41]

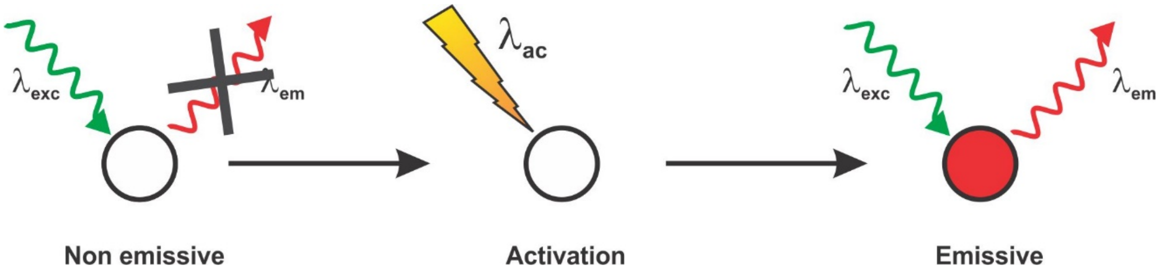

Figure 1.2. Schematic mechanism showing the probe emission quenched before photoactivation.

In this context, while fluorescence recovery after photobleaching (FRAP) remains the preferred method to study dynamic processes,[42-43] it has been shown how fluorescence photoactivation can overcome FRAP limitations.[2] (Figure 1.3) In fact, the identification of alternative strategies to turn on the emission of chromophores with concomitant changes in absorption can be extremely valuable to achieve outstanding fluorescence contrast and selective product bleaching.

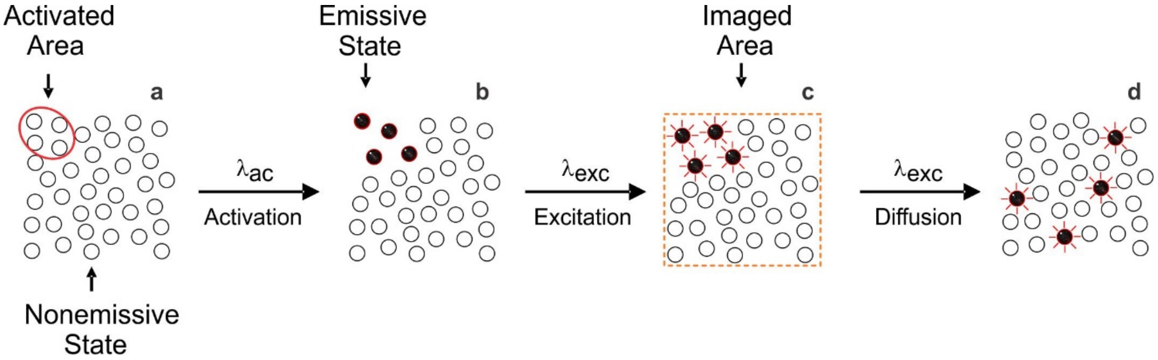

Figure 1.3. Photoactivation of a specific area in a biological specimen (a) leads to the conversion of non emissive probes to emissive ones (b) and the subsequent irradiation of the entire specimen allows the specific excitation of the photoconverted species (c) and the relative recording of the spatiotemporal translocation of the probes (d).

Specifically, two chapters of this thesis are focused on the synthesis, photophysical characterization and biological applications of photoactivatable fluorophores and, for ease of comprehension by the reader, the next subchapter will be dedicated to the description of the mechanistic photoactivation principles that have been exploited for the development of a library of the aforementioned compounds based on an oxazine switch discussed in Chapter 2 and 3.

1.2 Strategy of Photoactivation: an o-Nitrobenzyl Group in an Oxazine Scaffold

1.2.1 General Remarks

In order to design a proper photoactivatable fluorophore, the main factors to be considered are the chemical nature of the chromophore, the ease of extension of the molecular π system and the mechanism through which the emission is suppressed and activated.

Among the many chromophores used for biological applications (acridines, cyanines, rhodamines, fluorones), the BODIPY (4,4-Difluoro-4-bora-3a,4a-diaza-s-indacene) scaffold has been exploited tremendously thanks to its high quantum yield and molar absorption coefficient, narrow emission bandwidth and absorption in the visible region of the electromagnetic spectrum. Moreover, its chemical structure has been shown to withstand an incredible number of synthetic modifications that finely tune its photophysical properties.[44] For these characteristics, BODIPY has been chosen as the main molecular chromophore (highlighted in red in Figure 1.4) where its further conjugation with a functionalizable auxochrome (indolenine moiety in Figure 1.4) generated a new molecular entity with a bathochromically shifted absorption profile represented in Figure 1.4.

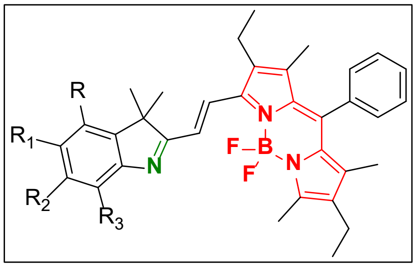

Figure 1.4. General structure of BODIPY derivatives discussed in chapter 2.

The ketimine functionality in the auxochrome (green in Figure 1.4) connecting the π systems of the benzene and the BODIPY could be seen as a *molecular switch*. In fact, saturating the carbon-nitrogen double bond, exploiting its reactivity towards 2-Halomethylphenols, introduces a molecular interruption in the π-communicating system between the two parts (red in Figure 1.5) and, as a result, the new species presents a hypsochromically shifted absorption (black profile in Figure 1.5). Upon the condition that the oxazine moiety is in the form of a 2-Nitrobenzyl derivative, a photosensitive trigger (blue in Figure 1.5), then the imine can be "regenerated" upon light irradiation to and a photoactivatable fluorophore was thus conceived.

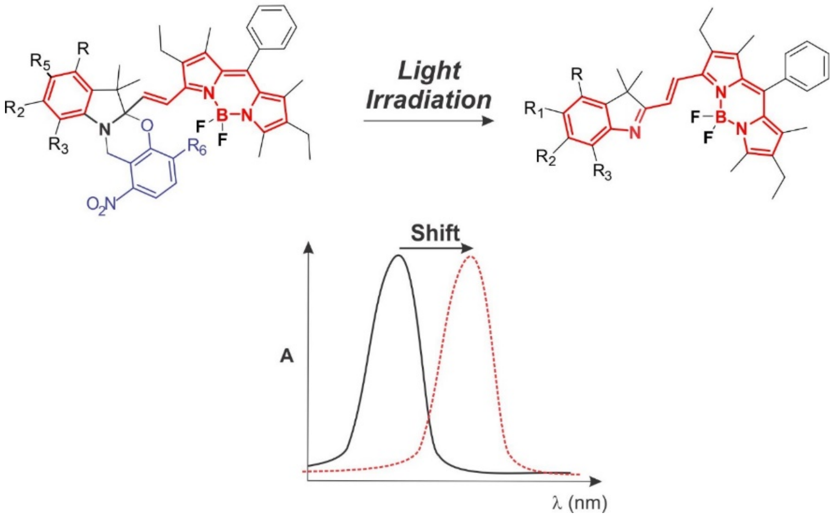

Figure 1.5. Photoactivation of a generic BODIPY derivative with consecutive extension of conjugation as depicted in the illustration with concomitant bathochromic shift shown in the bottom absorption spectrum.

Thus, this molecular design offers a new strategy to regulate the absorption characteristics of the emissive component under optical control with a different mechanism than the usual photocleavable PET-based quencher used in the majority of photoactivatable systems.[1, 45] Moreover, the selective excitation of the photogenerated product in the presence of the corresponding reactant allows a 2-channels monitoring of dynamic processes suppressing significantly background fluorescence.[2] In the next subchapter the reader will find the details of the cleavage mechanism of 2-Nitrobenzyl derivatives.

1.2.2 Uncaging Mechanism

Among the many photoremovable protecting groups that have been exploited to selectively release molecules of biological interest *in situ*, the 2-Nitrobenzyl scaffold is probably the most commonly studied.[46] First reported by Barltrop in 1966,[47] many authors tried to define the photoreaction mechanism over the years using various model compounds (Figure 1.6).

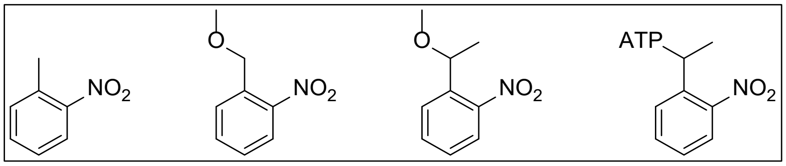

Figure 1.6. Some of the model compounds, based on the 2-Nitrobenzyl motive, used to study the reaction mechanism.

The latest studies on the photochemistry of 2-Nitrotoluene by Gilch,[48] together with the exquisite investigation performed by Wirz,[49] confirmed the complete picture on the full transformation. Here are reported the key mechanistic steps of the process using 2-Nitrobenzylmethylether as model compound (Figure 1.7)

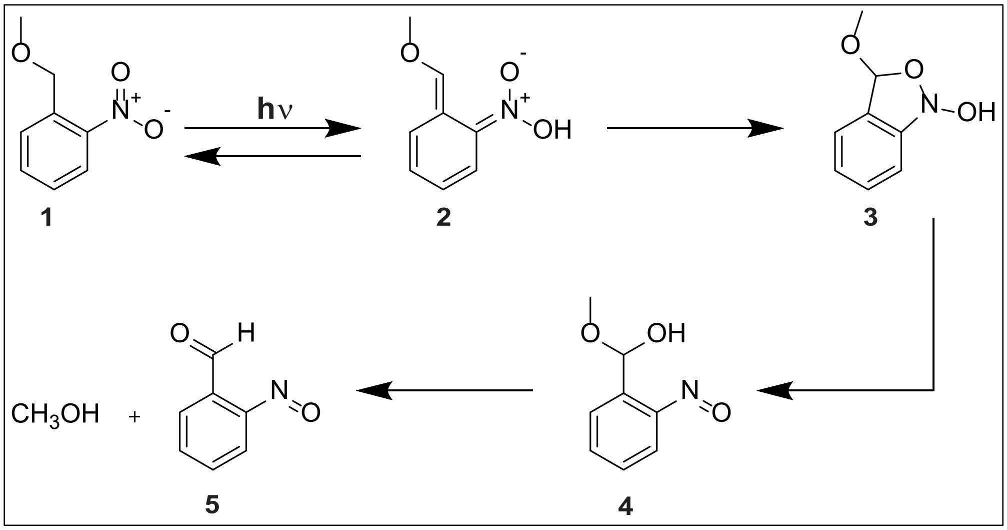

Figure 1.7. Photoconversion mechanism of 2-Methyloxymethyl-nitrobenzene (**1**) in Nitroso benzaldehyde (**5**) and Methanol.

The photorelease of methanol from **1** proceeds via three intermediates: the primary *aci*-nitro derivative **2,** the 1,3-Dihydrobenz[*c*]isoxazol-1-ol derivative **3** and 2-Nitrosobenzyl hemiacetal **4**. Irradiation of **1** with UV light ($300<\lambda<400$ nm) generates the aci-nitro tautomers **2** that can be detected by flash photolysis at $\lambda_{max} = 400$ nm. Subsequent attack on the monosubstituted ethene carbon by the nitronic acid anionic oxygen generates irreversibly the isoxazole derivative **3** that, upon ring opening, affords the nitroso derivative **4**. The rate-limiting step for the release of methanol is associated with the conversion **4** > **5** via dehydration of the hemiacetal to the aldehyde form.

1.2.3 Applications to Oxazines

While the previous subchapter treated the mechanism on a model compound, the leaving group connected to the benzylic position of the photoactivatable fluorophores developed in the ambit of our research (Chapter 2) is of different nature.

In fact, the nitrogen atom of the indolenine moiety is covalently attached to the benzylic position and the o-Nitrobenzyl derivative is masked in the form of an 1,3-oxazine. Thus, upon irradiation two different mechanisms can be conceived (Figure 1.8):

- **A.** The absorption of the radiation by the nitro group induces the phototransformation to generate the hemiaminal **3** that undergoes a cascade reaction with ring opening and formation of the photoproducts **4** and **5**.
- **B.** The C-O bond at the junction of the two heterocyclic fragments opens up to generate the zwitterionic form **1** that undergoes the photochemical transformation to afford the hemiaminal **2** which subsequent deamination leads to the photoproduct **4** and the 2-Nitrosobenzaldehyde **5**.

Although both mechanisms seems to be reliable, it hasn’t been proven which pathway governs the photochemical transformation.

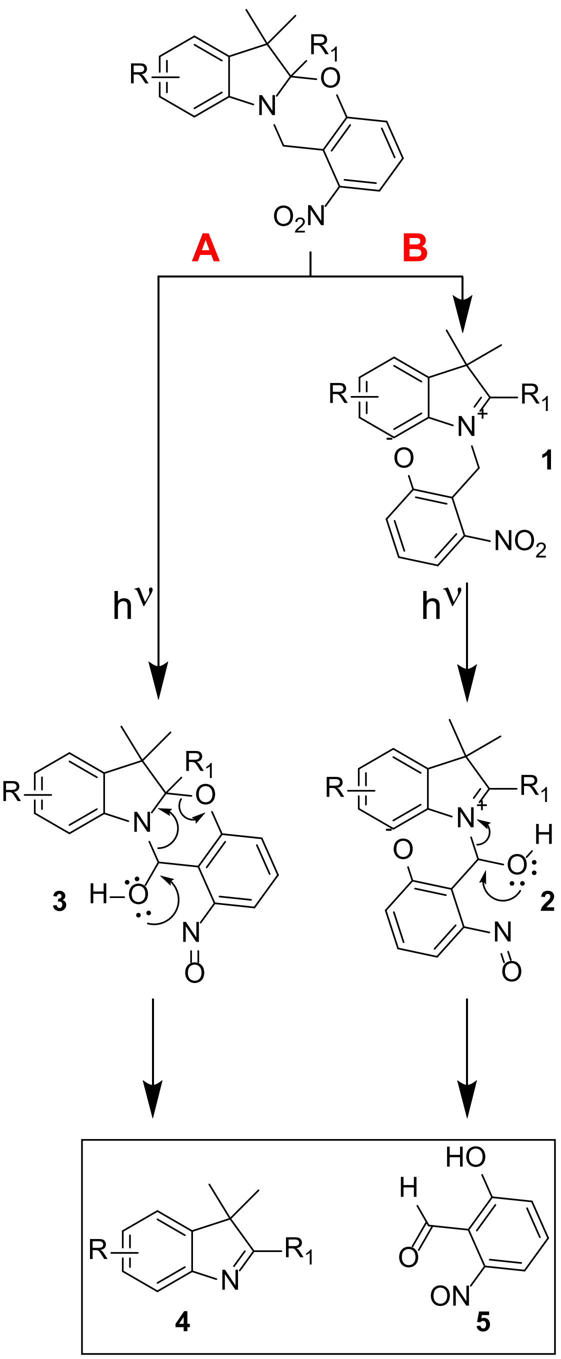

Figure 1.8. Illustration of the two pathways **A** and **B** hypothesized for the photoconversion mechanism.

1.3 Polymeric Nanocarriers

The molecular fragments of the photoactivatable fluorophores described in these thesis (Figure 1.4) are generally hydrophobic and it’s practically impossible dissolve them in aqueous solutions. However, the design of specific amphiphilic polymers can solve the issue solubilizing the aforementioned compounds in aqueous buffer solutions (i.e. PBS).[50] Specifically the amphiphilic polymer represented in Figure 1.9 was used:

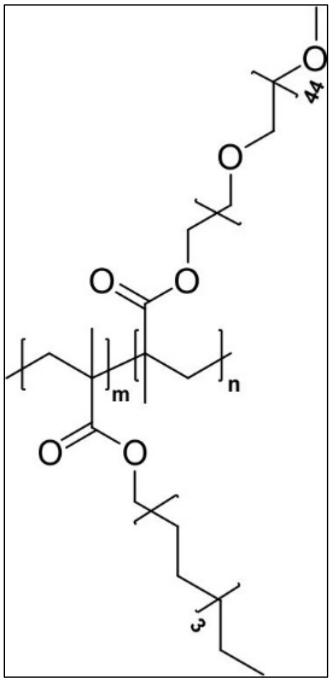

Figure 1.9. Structure of the amphiphilic polymer used for the delivery of the photoactivatable fluorophores described in chapter 2.

When mixed with water at relatively low concentrations, the polymer migrates to the air/water interface to avoid exposure of its lipophilic part to the aqueous environment creating a superficial chain made of the hydrophilic part in direct contact with water. If the amphiphile concentration is gradually increased, upon crowding of the air/water interface, the molecule starts to be forced to remain within the aqueous phase and, above a certain concentration threshold, denoted critical micellar concentration (CMC), the polymer molecules self-assemble into micellar aggregates. These supramolecular assemblies present the alkyl chain in the interior of the nanoconstructs while the PEG chain is directly exposed to the water. Increasing the concentration of polymer translates into an increase of micelles dissolved in the aqueous phase. The supramolecular assemblies, of spherical shape, remain isolated from each other with no spatial correlation. (Figure 1.10)

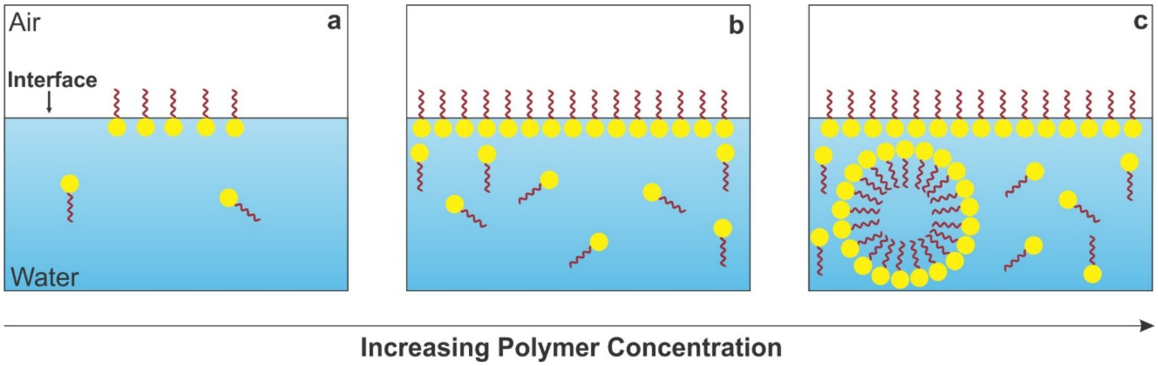

Figure 1.10. Schematic illustration of micelles formation in relation to the concentration of the amphiphilic polymer in solution. At low concentration the polymer molecules are ordered at the Air-Water interface (**a**) until the surface gets crowded enough to induce the self-assembly of the polymer into micelles (**c**).

Specifically these nanoconstructs encapsulate the photoactivatable fluorophores that retain their photochemical and photophysical properties and assure the delivery of the same in biological specimens (Chapter 2).

Chapter 2: Photoactivatable NIR Fluorophores to Monitor Cell Dynamics in Living Organisms

2.1 Background

The Borondipyrromethene (BODIPY) chromophore is a versatile platform for the construction of fluorescent probes for bioimaging and biosensing applications.[44-45, 51-56] Efficient and relatively simple synthetic procedures for the preparation of this heterocyclic scaffold, as well as for the introduction of substituents on its boron center and pyrrole rings, are well established. Additionally, BODIPY chromophores absorb in the visible region of the electromagnetic spectrum with large molar absorption coefficients and, when the conformational freedom of their substituents is restricted, emit with large fluorescence quantum yields. Furthermore, their absorption and emission bands can be shifted bathochromically into the far-red/near-infrared region, to overcome the characteristic autofluorescence of biological samples, with appropriate structural modifications of the heterocyclic platform aimed at extending electronic conjugation. In spite of the attractive combination of synthetic accessibility and outstanding photophysical properties, structural designs for the photochemical activation of their fluorescence remain limited to a few representative examples.[57-61] Yet, photoactivatable fluorophores are becoming a powerful tool to investigate a diversity of specimens with spatiotemporal control.[62-67] Indeed, the ability to switch fluorescence on exclusively after a photochemical reaction offers the opportunity to generate an emissive species in any region of a given sample of interest at a specific interval of time. In turn, the control of light emission in space and time permits the monitoring of dynamic events[41, 68-70] and the overcoming of diffraction[71-73] with the sequential acquisition of fluorescence images. The identification of viable strategies to photoactivate BODIPY fluorescence efficiently would, therefore, have significant implications in these emerging bioimaging methodologies by providing molecular probes with unrivaled synthetic and photophysical characteristics.

The photoactivatable BODIPYs developed so far rely on the photoinduced disconnection of a quenching component from the emissive chromophore.[57-61] Generally, excitation of the chromophore at an appropriate wavelength (λ_{Ex}) encourages the transfer of an electron to or from the quencher. This process deactivates the excited chromophore nonradiatively to decrease drastically its fluorescence quantum yield. Illumination at a suitable activation wavelength (λ_{Ac}) cleaves the quencher from the chromophore. The physical separation of the two prevents electron transfer and allows the chromophore to deactivate radiatively after excitation. The overall result is the detection of intense fluorescence only if the sample is illuminated at λ_{Ex} after irradiation at λ_{Ac}. However, unitary quenching efficiencies are hard, if at all possible, to achieve in the initial state and the emission intensity only increases from a low to a high value, rather than switching form off to on. In search of strategies to activate BODIPY fluorescence with infinite contrast, our laboratories developed an alternative mechanism to switch the emission of these compounds.[1-2, 74] It is based on the attachment of a photoswitchable auxochrome to the BODIPY chromophore, which enables the latter to absorb at λ_{Ex} exclusively after illumination at λ_{Ac}. The selective excitation of the photochemical product translates into fluorescence activation with contrast levels that are impossible to achieve with mechanisms based on quenching. Nonetheless, the absorption and emission bands of the photoactivatable BODIPYs based on this mechanism are confined within the visible region. The extension of these operating principles to activate fluorescence in the far-red/near-infrared portion of the electromagnetic spectrum instead would provide the opportunity to avoid the autofluorescence of biological samples and would be especially valuable for possible bioimaging applications *in vivo*. These considerations prompted us to explore structural modifications of our original design aimed at extending the electronic conjugation of the BODIPY platform and shift bathochromically its absorption and emission bands. This article reports the synthesis and photophysical characterization of these emissive compounds, the photoactivation of the far-red/near-infrared fluorescence of a representative member of these extended BODIPYs and its application to monitor cellular dynamics in developing embryos.

2.2 Results and Discussion

2.2.1 Design, Synthesis and Structural Characterization

The operating principles to activate the fluorescence of our original photoactivatable BODIPY (**1** in Figure 2.0) relied on the irreversible cleavage of a 2*H*,4*H*-[1,3]oxazine heterocycle upon illumination at λ_{Ac}.[1] This photochemical reaction extends the electronic delocalization of the BODIPY chromophore over the adjacent 3*H*-indole auxochrome in the resulting product (**3** in Figure 2.0). Concomitantly, the $S_0 \rightarrow S_1$ absorption shifts bathochromically to allow the excitation of **3** at a λ_{Ex} where **1** cannot absorb and, hence, the activation of fluorescence with infinite contrast. However, the absorption and emission bands of the photogenerated fluorophore remain in the visible region with maxima at 588 and 602 nm (λ_{Ab} and λ_{Em} in Table 2.0) respectively in acetonitrile solution.

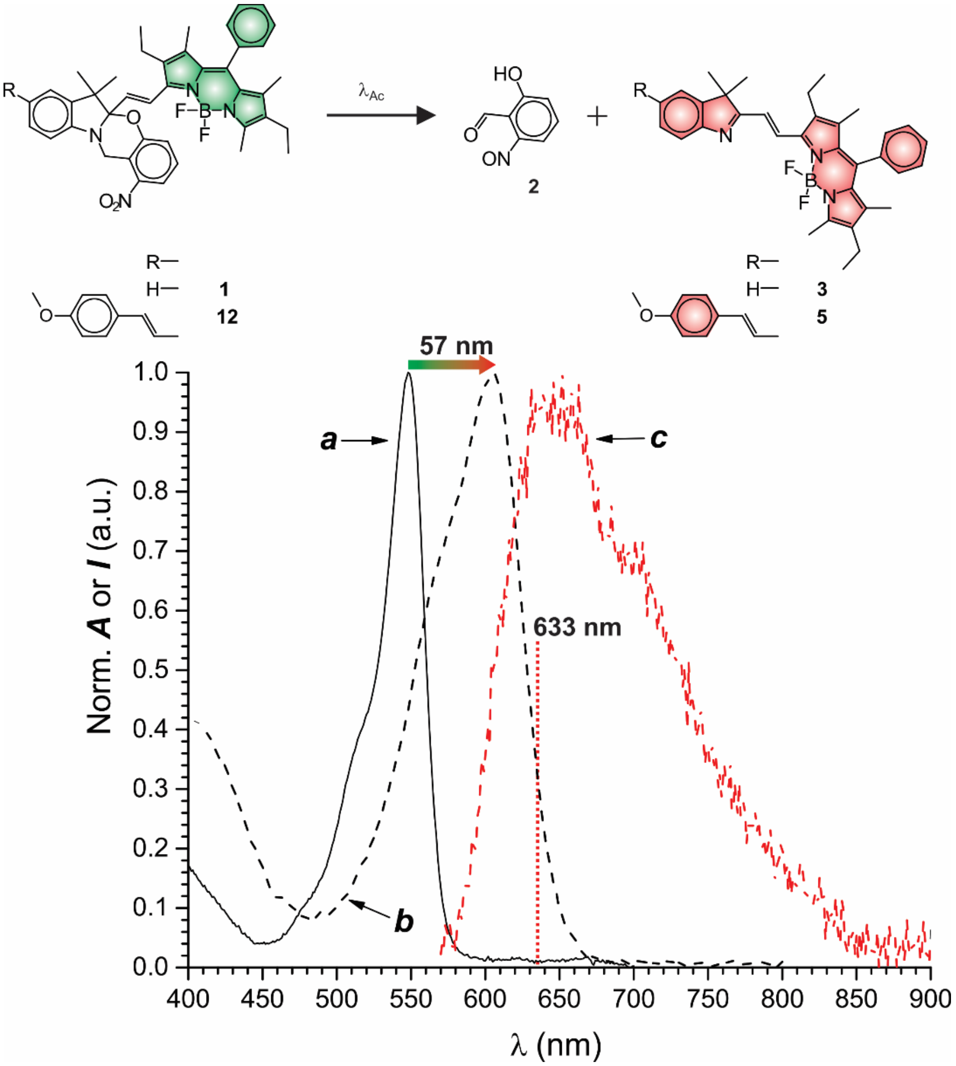

Figure 2.0. Abs and emission (λ_{Ex}=560 nm) spectra of MeCN solutions (10 μM) of either **12** (***a***) or **5** (***b*** and ***c***) at 20 °C.

Table 2.0. Wavelengths at the absorption (λ_{Ab}) and emission (λ_{Em}) maxima, Stoke's shift ($\Delta\lambda$), absorbance (A_{633}) at 633 nm reported relative to that at λ_{Ab} and fluorescence quantum yield (Φ_F) of 3–12 in aerated MeCN at 20 °C.[a]

	λ_{Ab} (nm)	λ_{Em} (nm)	$\Delta\lambda$ (nm)	A_{633} (%)	Φ_F
3	588	602	14	1	0.50
4	594	606	12	7	0.52
5	605	652	47	37	0.04
6	605	623	18	33	0.09
7	600	612	12	53	0.007
8	600	618	18	21	0.19
9	600	617	17	14	0.15
10	603	614	11	35	0.004
11	605	—	—	31	—

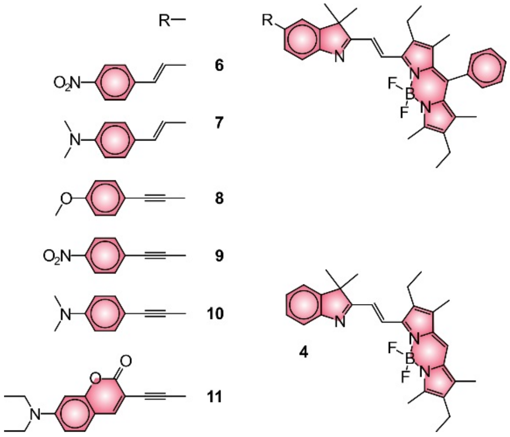

[a] The data for **3** and **8** are literature values (ref. [1] and [2]). The values of ϕ_F for **4**–**11** were determined against a MeCN solution of **3**.

In principle, the π-system of **3** can be extended even further with the attachment of appropriate substituents to position 5 of the 3*H*-indole heterocycle. Such a structural transformation should shift bathochromically the absorption and emission bands of the BODIPY chromophore and, possibly, enable the photoactivation of far-red/near-infrared fluorescence. These considerations suggested the introduction of either ethenyl (**5**–**7** in

Figure 2.0 and Table 2.0) or ethynyl (**8**–**11** in Table 2.0) groups on this particular position. The resulting compounds were synthesized in one–five steps from known precursors (Figures 2.6–2.12) and their structural identity was confirmed by electrospray ionization mass spectrometry (EISMS) and nuclear magnetic resonance (NMR) spectrometry. Additionally, single crystals suitable for X-ray diffraction analysis (Table 2.2) could be obtained in the case of **5**. The resulting structure (Figure 2.1) confirms the presence of a 2-(4-methoxyphenyl)ethenyl group in position 5 of the 3*H*-indole heterocycle with a dihedral angle about the intervening [C–C] bond of 16°. Similarly, the BODIPY chromophore is twisted by 18° about the [C–C] bond connecting it to the adjacent olefinic bridge. The [C=C] bond between the BODIPY chromophore and the 3*H*-indole auxochrome as well as the one connecting this heterocycle to the 4,4'-phenylene ring adopt *trans* configurations. Consistently with this geometrical arrangement about both [C=C] bonds, the ^{1}H NMR spectrum of **5**, recorded in deuterated chloroform, reveals AB systems for the olefinic protons with coupling constants greater than 16 Hz. This particular compound was further functionalized with a 2*H*,4*H*-[1,3]oxazine heterocycle in an additional synthetic step (Figure 2.13) to generate an analog (**12** in Figure 2.1) of **1** with extended π-conjugation. Once again, the structural identity of the target molecule was confirmed by EISMS and NMR spectrometry.

Figure 2.1. ORTEP (50 % thermal ellipsoid probability) representation of the geometry adopted by **5** in a single crystal.

2.2.2 Photochemical and Photophysical Properties

The absorption and emission spectra (Figures 2.14–2.23) of **3–11** confirm that the attachment of a π-system to position 5 of the 3*H*-indole auxochrome shifts bathochromically the bands of the BODIPY chromophore. The largest shifts are observed for **5** (***b*** and ***c*** in Figure 2.0), which has absorption and emission maxima at 605 and 652 nm (λ_{Ab} and λ_{Em} in Table 2.0) respectively in acetonitrile. Consistently with significant electronic communication along the extended π-system of these molecules, the absorption spectrum of **5** differs from the sum of the spectra of the parent system (**3**) and 4-methoxystyrene (Figure 2.26). However, π-substitution appears to facilitate the nonradiative deactivation of the excited BODIPY in this particular solvent. As a result, the fluorescence quantum yield (Φ_F in Table 2.0) of **5–11** is significantly lower than that of **3**.

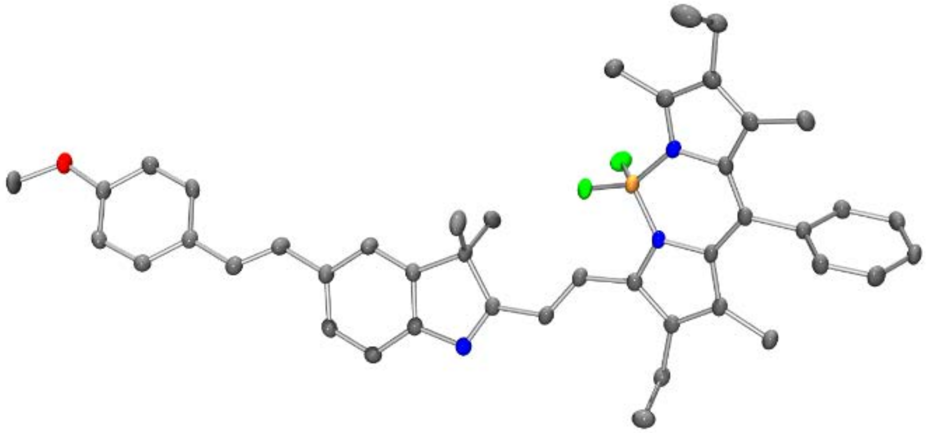

Additionally, the conformational freedom about the four [C–C] bonds present along the extended π-system of these compounds translates into the co-existence of multiple conformations in solution to impose wavelength-dependence on the excitation spectra (Figure 2.27).

The transition from acetonitrile to toluene has negligible influence on the absorption and emission spectra of **3**, but has a pronounced effect on those of **5** (Figure 2.2). Specifically, the fluorescence quantum yield (Φ_F in Table 2.0) of **5** increases from 0.04 in acetonitrile[1] to 0.26 in toluene and raises further to 0.31 in hexane. In fact, both the absorption and emission spectra of this compound display a significant solvent dependence (Figure 2.29). The corresponding Lippert–Mataga plot (Figure 2.29), however, shows a nonlinear dependence of Stoke's shift on the orientation polarizability. This trend is indicative of the occurrence of a process in the excited state, in addition to solvent relaxation. Furthermore, the emission intensity of **5** decreases monotonically with temperature in viscous media (Figure 2.30), suggesting that a pronounced geometrical change is responsible for promoting the nonradiative decay of the excited state.

---

[1] The absorption spectrum of **5** in acetonitrile scales linearly with concentration (Figure 2.28), indicating that this compound does not aggregate under the experimental conditions used to measure the fluorescence quantum yield.

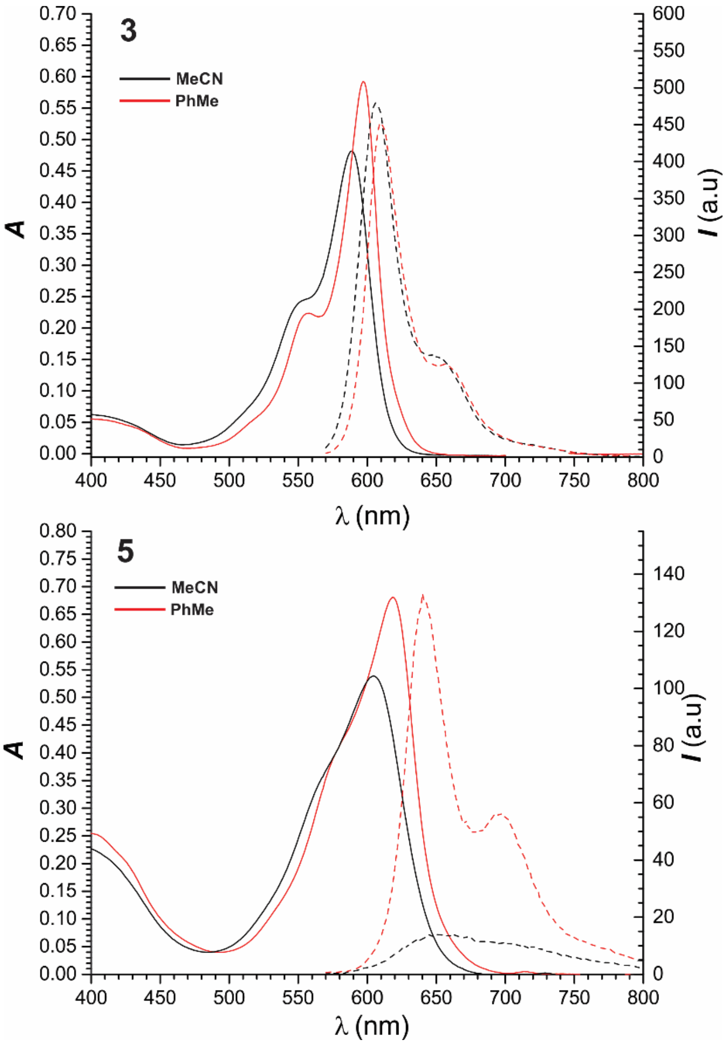

Figure 2.2. Absorption and emission (λ_{Ex} = 560 nm) spectra of MeCN and PhMe solutions (10 μM) of either **3** or **5** at 20 °C.

Table 2.1 Wavelengths at the absorption (λ_{Ab}) and emission (λ_{Em}) maxima, Stoke's shift ($\Delta\lambda$), absorbance (A_{633}) at 633 nm reported relative to that at λ_{Ab}. fluorescence quantum yield (Φ_F) and activation quantum yield (Φ_A) of **5** and **12** in aerated solutions at 20 °C.[a]

	Solvent	λ_{Ab} (nm)	λ_{Em} (nm)	$\Delta\lambda$ (nm)	A_{633} (%)	Φ_F	Φ_A (10^{-4})
5	MeCN	605	640	35	37	0.04	—
	PhMe	619	640	21	64	0.26	—

	H_2O	614	628	14	63	0.10	—
	Hexane	612	629	17	30	0.31	—
12	MeCN	548	581	33	0.7	0.004	0.3
	PhMe	554	566	12	0.8	0.04	4.2
	H_2O	551	560	9	1.6	0.11	7.9

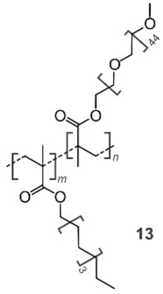

13

[a] The values of Φ_F were determined against a MeCN solution of **3**. Those of Φ_A were determined against a ferrioxalate actinometer. The measurements in H_2O were performed in the presence of **13**.

The emission intensity of **3** decays monoexponentially in acetonitrile and toluene (Figure 2.32) with a lifetime of 5.3 ns (Table 2.3) in both instances. That of **5** decays monoexponentially in toluene (Figure 2.33) with a lifetime of 1.9 ns and biexponentially in acetonitrile with an average lifetime of 0.7 ns. Time-resolved spectra further reveal the emission band of **5** to shift from 661 to 618 nm (Figure 2.34) within 5 ns from excitation in acetonitrile. Global analysis of the fluorescence decays shows the component at 661 nm to have a lifetime of 0.6 ns (96%) and that at 618 nm to have a lifetime of 3.7 ns (4%). Thus, excitation of **5** results in the adiabatic formation of a weakly emissive species with fast kinetics in acetonitrile. A decrease in solvent polarity hinders the formation of this species and both fluorescence lifetime and quantum yield increase in toluene. Furthermore, this process does not occur in **3**, suggesting that it must be associated with the presence of a 2-(4-methoxyphenyl)ethenyl substituent on the 3*H*-indole heterocycle of **5**.

The observed increase in fluorescence quantum yield with an increase in viscosity and a decrease in polarity suggests that the process occurring upon excitation of **5** is a conformational change leading to the formation of a twisted intramolecular charge transfer (TICT) state.[75] In principle, rotation about any one of the four [C–C] bonds flanking the two olefinic bridges of **5** should disrupt electronic conjugation along the extended π-system and possibly populate a TICT state. Indeed, density functional theory[76] (DFT) calculations on an optimized geometry of **5** reveal the highest occupied molecular orbital (HOMO) and the lowest unoccupied molecular orbital (LUMO) to extend over the entire π-platform (Figure 2.35). Rotation of the BODIPY chromophore about the [C–C] bond connecting it to the adjacent olefinic bridge disrupts conjugation and localizes the HOMO on the substituted 3*H*-indole auxochrome and the LUMO on the BODIPY chromophore (Figure 2.35). Time-dependent (TD) DFT[77] calculations (Table 2.4) on this particular geometry indicate that the first singlet excited state is predominantly associated with this orbital pair, has a vertical energy of 2.40 eV and is essentially forbidden with an oscillator strength of 0.05. These observations suggest that this particular species is the TICT state governing the excitation dynamics of **5**. Indeed, rotation about any of the other three [C–C] bonds also disrupts electronic conjugation, but localizes both HOMO and LUMO on the BODIPY chromophore. Consistently, TD DFT calculations on the corresponding geometries reveal the vertical transitions to the first singlet excited state to have the large oscillator strengths characteristic of BODIPY excitation. On the basis of these considerations, the excitation dynamics (Figure 2.36) of **5** can be postulated to involve (1) a vertical transition to a locally-excited (LE) state, (2) the adiabatic population of the TICT state in a solvent with high polarity and low viscosity and (3) the predominant nonradiative decay of the TICT state back to the ground state. The calculated vertical energies (Table 2.4) of the LE and TICT states suggest that only 1.7 kcal are sufficient to populate the latter from the former, which is therefore thermally accessible, and agree with the hypsochromic shift observed in the time-resolved emission spectra (Figure 2.34).

The fusion of a 2*H*,4*H*-[1,3]oxazine heterocycle on the 3*H*-indole fragment of **5** to generate **12** interrupts electronic conjugation along the extended π-system of the former. As a result, the main BODIPY absorption shifts from 605 to 548 nm (λ_{Ab} in Table 2.1, ***a*** and ***b*** in Figure 2.0) in acetonitrile with this structural transformation. The resulting compound, however, is essentially not emissive under these experimental conditions (Φ_F in Table 2.1, Figure 2.25). The relatively electron rich 3*H*-indole heterocycle is, presumably, donating an electron to the excited BODIPY chromophore, preventing its radiative deactivation. Indeed, cyclic voltammograms (Figure 2.37) of **12** suggest this photoinduced electron transfer process to be exergonic with a free-energy change of –0.44 eV.[2]

Illumination of **12** at a λ_{Ac} where its 2-nitrobenzyl fragment absorbs cleaves the 2*H*,4*H*-[1,3]oxazine heterocycle irreversibly to produce **2** and **5**, in agreement with the photochemical behavior of the parent system (**1**).[1] Consistently, absorption spectra (Figure 4), recorded sequentially during the photolytic transformation in toluene, reveal a decrease in the BODIPY absorption of **5** with the concomitant appearance and growth of the characteristic band of **5**. Similarly, the corresponding emission spectra (inset of Figure

---

[2] The free-energy change ($\Delta G°$) for the electron transfer process was calculated with equation (1) (Kavarnos, G. J. *Fundamentals of Photoinduced Electron Transfer*; VCH: New York, 1993). The oxidation potential (E_{Ox}) of the donor and the reduction potential (E_{Red}) of the acceptor in both instances were estimated from the cyclic voltammograms (Figure 2.37) of **12**. The energy change (ΔE_{00}) for the $S_0 \rightarrow S_1$ transition of the BODIPY chromophore was estimated to be +2.20 eV from the absorption and emission spectra of **12**. The donor–acceptor distance (d) was approximated to 0.5 nm.

$$\Delta G° = e\,E_{Ox} - e\,E_{Red} - \Delta E_{00} - \frac{e^2}{4\,\pi\,\varepsilon_0\,\varepsilon_r\,d} \quad (1)$$

2.3) show the developing fluorescence of the photochemical product and high-performance liquid chromatography (HPLC) traces (Figure 2.3) further confirm the gradual conversion of **12** into **5**. Analysis of the temporal evolutions of the absorbance for the product indicates the quantum yield (Φ_A in Table 2.1) for this photochemical transformation to be 4.2×10^{-4} under these experimental conditions. The very same process can be implemented also in aqueous environment with the aid of an amphiphilic polymer (**13** in Table 2.1). Indeed, **12** is relatively hydrophobic and, essentially, insoluble in water. However, it readily dissolves in the presence of sufficient amounts of **13** (Figure 2.25), in analogy to the behavior of the parent system (**1**).[1] Illumination of the resulting solution at an appropriate λ_{Ac} also converts **12** into **2** and **5** with spectral changes analogous to those detected in organic solution and a Φ_A of 7.9×10^{-4} (Table 2.1, Figure 2.31).

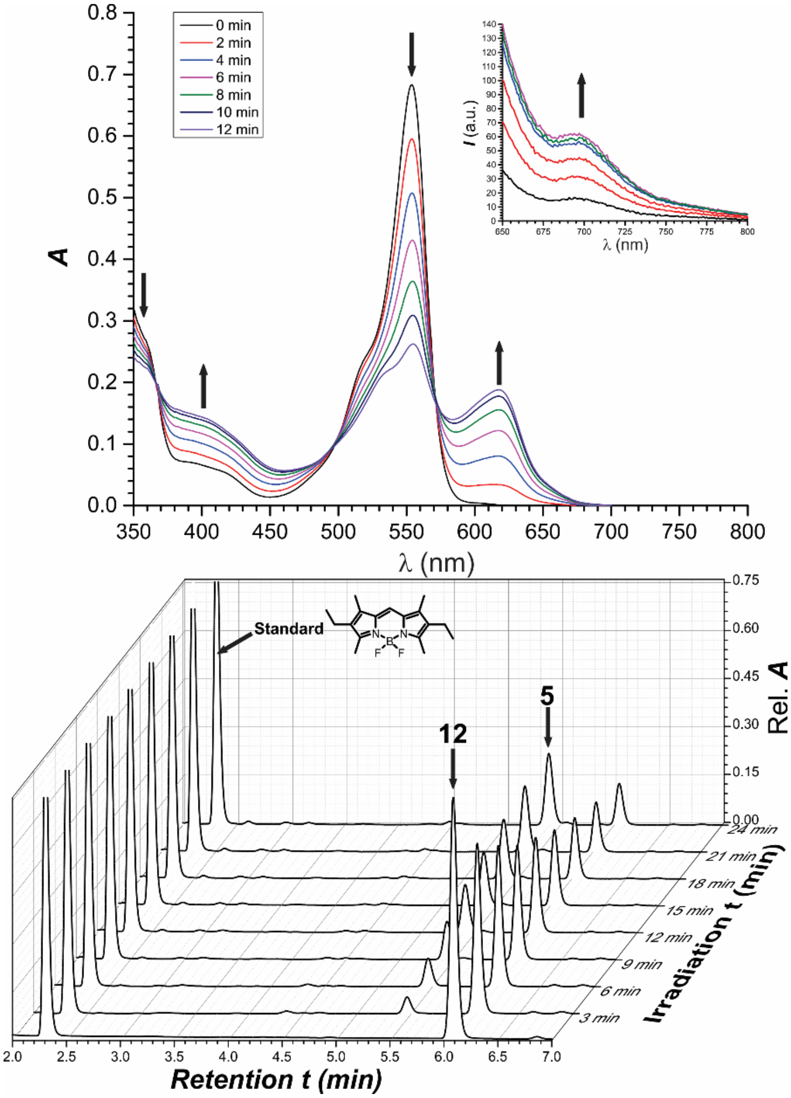

Figure 2.3. Absorption spectra and HPLC traces of a PhMe solution (20 μM) of **12** recorded before and after irradiation (350 nm, 4.2 mW cm^{-2}) at 20 °C.

2.2.3 Fluorescence Imaging

The structural transformation associated with the photochemical conversion of **12** into **5** shifts bathochromically the BODIPY absorption (***a*** and ***b*** in Figure 1, Figure 2.3) to allow the selective excitation of the product and the activation of significant emission in the far-red/near-infrared region (***c*** in Figure 1, inset of Figure 2.3). The very same process can be reproduced within poly(methyl methacrylate) (PMMA) films and visualized with the aid of a confocal laser-scanning microscope. Specifically, images (Figure 2.38) of a PMMA film, doped with **12**, recorded before and after the illumination at λ_{Ac} of a square at the center of the imaging field clearly reveal fluorescence activation with optimal contrast.

The visible wavelength (405 nm) and low power (<0.1 mW) sufficient to convert **12** into **5** suggest that this protocol can be adapted to activate fluorescence *in vivo* with minimal toxic effects. In order to test its possible implementation in biological preparations, the photoactivatable fluorophore (**12**) was dissolved in phosphate buffer saline (PBS) with the assistance of the amphiphilic polymer (**13**) and microinjected into *Drosophila melanogaster* embryos at stage 2–4 of their development. Images of two embryos, recorded before and after (***a*** and ***b*** in Figure 2.4) illumination at λ_{Ac} of part of the cellular blastoderm of one of them only, show fluorescence exclusively in the activated region. Indeed, the photophysical properties of the photochemical product allow excitation (633 nm) and detection (700–800 nm) conditions that ensure no autofluorescence from the biological specimen. Magnifications (Figure 2.5, Video 2.0) of the activated region reveal the localization of the rather hydrophobic fluorescent probes in the membranes of the many cells in the blastoderm. These additional images were collected sequentially over the course of 9 min after activation. Their comparison shows that that the visualized cells translocate gradually in the antero → postero direction. For example, the movement of one cell (yellow arrow in Figure 2.5) relative to a reference marker (dotted line in Figure 2.5) can be tracked in time with this image acquisition protocol.

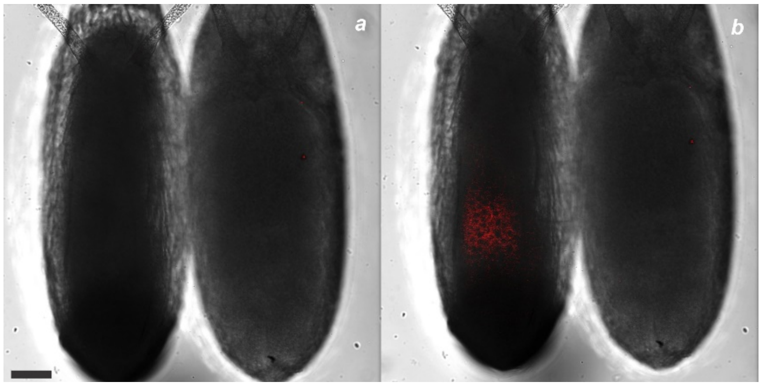

Figure 2.4. Overlaid fluorescence and transmittance images (scale bar = 50 µm, λ_{Ex} = 633 nm, λ_{Em} = 700–800 nm) of two *Drosophila melanogaster* embryos, recorded upon injection of a PBS solution of nanoparticles of **13**, containing **12**, into one of them only before (*a*) and after (*b*) irradiation (λ_{Ac} = 405 nm, 22 µW, 60 s) of a selected area within the labeled embryo.

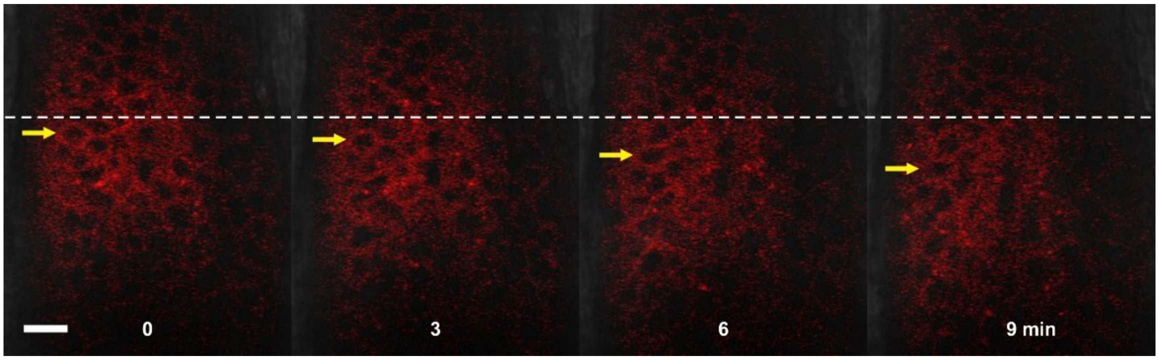

Figure 2.5. Overlaid fluorescence and transmittance images (scale bar = 20 µm, λ_{Ex} = 633 nm, λ_{Em} = 700–800 nm) of a *Drosophila melanogaster* embryo, recorded sequentially over 9 min after injection of a PBS solution of nanoparticles of **13**, containing **12**, and irradiation (λ_{Ac} = 405 nm, 22 µW, 60 s) of a selected area within the cellular blastoderm.

2.3 Conclusion

Our results showed that extending the molecular π-system, introducing appendages of aromatic nature at the 5th position of the indolenine auxochrome, bathochromically shifted the photophysical profile of the fluorophores. While the benefit of such an extension allows these emitters to be used as Near-Infrared agents, the increase of nonradiative deactivation from the photogenerated excited state upon irradiation complicates the scenario. Nevertheless, we showed that a photoactivatable version of the best representative of the synthesized library (**12**) can be used in Drosophila melanogaster embryos to monitor cellular translocation in the NIR range with excellent contrast.

2.4 Experimental Section

Synthesis. Chemicals were purchased from commercial sources and used as received. CH_2Cl_2 and MeCN were distilled over CaH_2. Tetrahydrofuran (THF) was distilled over Na and benzophenone. H_2O (18.2 MΩ cm) was purified with a Barnstead International NANOpure Diamond analytical system. Compounds **1**, **3**, **8**, **13**, **20**, **22** and **29** were prepared following literature protocols.[1-2] Compounds **14**, **15**, **17**, **19**, **21** and **23**–**28** were synthesized adapting reported protocols.[78-83] EISMS was performed with a Bruker micrOTO-Q II spectrometer. NMR spectra were recorded with Bruker 300, 400 and 500 spectrometers.

4. Trifluoroacetic acid (TFA, 240 µL, 408 µmol) was added to a solution of 2,3,3-trimethylindolenine (203 µL, 1.26 mmol) and **16** (0.2 g, 0.63 mmol) in EtOH (20 mL). The mixture was heated under reflux for 17 hours. After cooling down to ambient temperature, the solvent was distilled off under reduced pressure. The residue was dissolved in EtOAc (20 mL) and washed with a saturated aqueous solution of $NaHCO_3$ (2 × 20 mL). The organic phase was dried over Na_2SO_4 and the solvent was distilled off under reduced pressure. The residue was purified by column chromatography [SiO_2, hexane/EOAc (30:10, v/v)] to give **4** (58 mg, 20%) as a blue solid. HRESIMS: *m/z* calcd for

$C_{28}H_{32}BF_2N_3$: 459.2657; found: 460.2738 [M + H]$^+$; ^{1}H NMR (500 MHz, $CDCl_3$): δ = 8.05 (d, 17.5 Hz, 1H), 7.67 (d, 7.5 Hz, 1H), 7.36–7.34 (m, 2H), 7.30–7.26 (m, 2H), 7.03 (s, 1H), 2.76 (q, 7.5 Hz, 2H), 2.61 (s, 3H), 2.43 (q, 7.5 Hz, 2H) 2.22 (s, 6H), 1.62 (s, 6H), 1.26 (t, 7.5 Hz, 3H), 1.11 (t, 7.5 Hz, 3H).

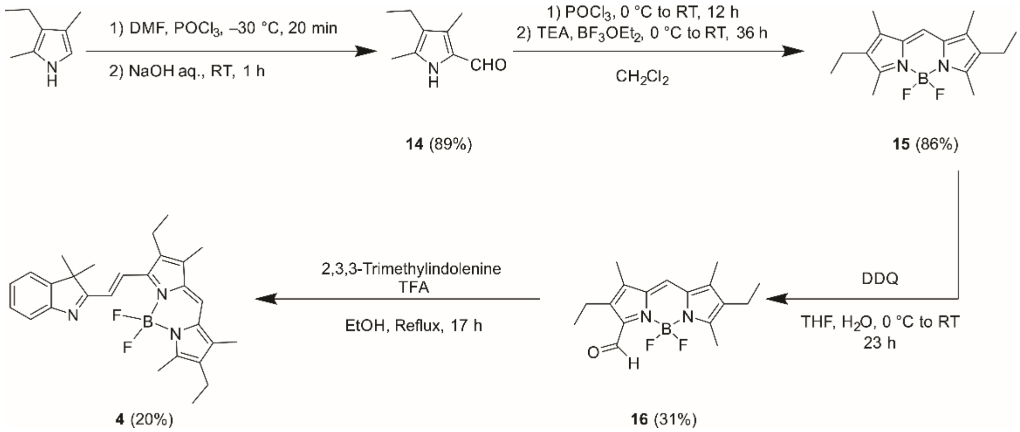

Figure 2.6. Synthesis of **4**.

5. *Method A*: TFA (20 µL, 34 µmol) was added to a solution of **19** (50 mg, 0.17 mmol) and **20** (67 mg, 0.17 mmol) in EtOH (10 mL) maintained under Ar. The mixture was heated under reflux for 24 hours. After cooling down to ambient temperature, the solvent was distilled off under reduced pressure. The residue was dissolved in CH_2Cl_2 (10 mL) and washed with a saturated aqueous solution of $NaHCO_3$ (2 × 20 mL). The organic phase was dried over Na_2SO_4 and the solvent was distilled off under reduced pressure. The residue was purified by column chromatography [SiO_2, hexane/EtOAc (60:20, v/v)] first and then by preparative thin-layer chromatography [SiO_2, hexane/EtOAc/MeAc (50:10:1.8 v/v)] to give **5** (7 mg, 6%) as a blue solid. *Method B:* A solution of **21** (16.2 mg, 91 µmol), $Pd(PPh_3)_4$ (3 mg, 2.5 µmol) and K_2CO_3 (32 mg, 0.23 mmol) in H_2O (1 mL) was added to a degassed solution of **22** (50 mg, 76 μmol) in THF (5 mL) maintained under Ar. The mixture was heated under reflux for 4 hours. After cooling down to ambient temperature, it was filtered over a Celite plug and the solvent was distilled off under reduced pressure. The residue was dissolved in EtOAc (15 mL) and washed with a saturated aqueous solution of NaCl (3 × 15 mL). The organic phase was dried over Na_2SO_4 and the solvent was distilled off under reduced pressure. The residue was purified by column chromatography [SiO_2, hexane/CH_2Cl_2/EtOAc (40:10:10, v/v)] to give **5** (40 mg, 79%) as a blue solid. HRESIMS: *m/z* calcd for $C_{43}H_{44}BF_2N_3O$: 667.3545; found: 668.3646 $[M + H]^+$; ^1H NMR (400 MHz, $CDCl_3$): δ = 8.13 (d, 17.3 Hz, 1H), 7.62 (d, 8.0 Hz, 1H), 7.58 – 7.43 (m, 7H), 7.39–7.20 (m, 3H), 7.11 (d, 16 Hz, 1H), 7.09 (d, 16 Hz, 1H), 6.93 (d, 8.3 Hz, 2H), 3.86 (s, 3H), 2.75–2.55 (m, 5H), 2.35 (q, 7.0 Hz, 2H), 1.67 (s, 6H), 1.33 (s, 3H), 1.32 (s, 3H), 1.18 (t, 7.5 Hz, 3H), 1.02 (t, 7.5 Hz, 3H).

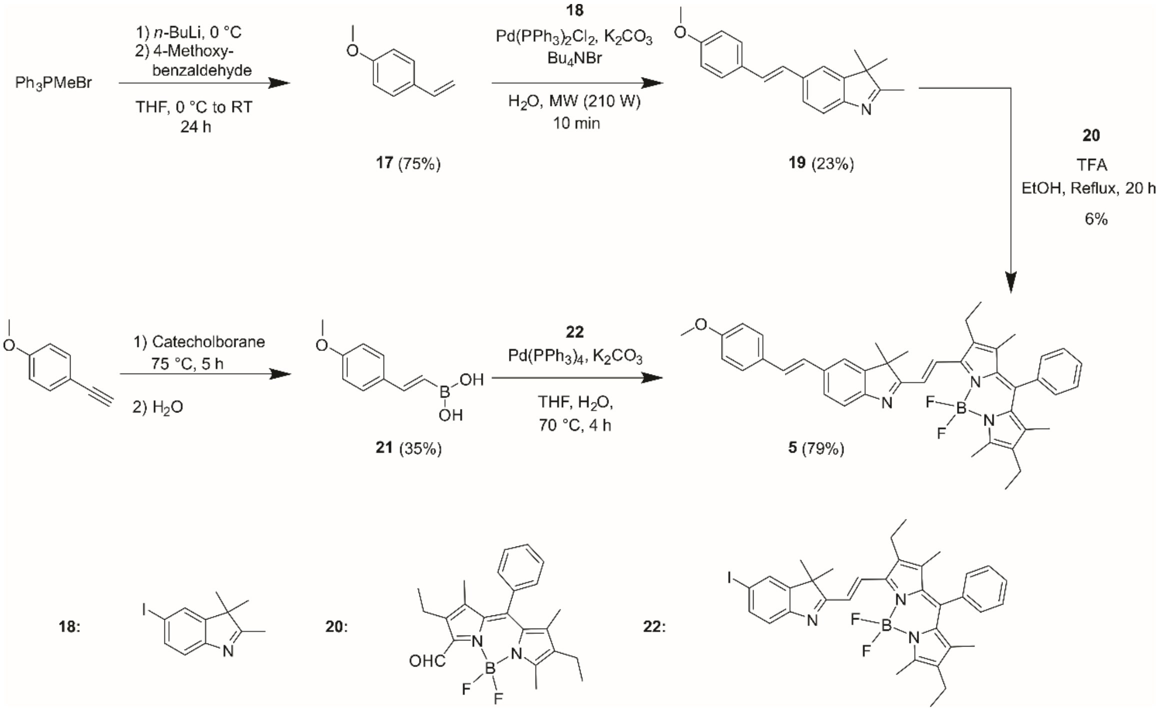

Figure 2.7. Synthesis of **5**.

6. $Pd(OAc)_2$ (3.37 mg, 15 µmol) was added to a degassed solution of **22** (50 mg, 76 µmol) and TEA (12 µL, 84 µmol) in dry DMF (1 mL) maintained under Ar in a pressure vial. The vial was capped and shaken for 5 minutes. After the addition of **23** (17 mg, 114 µmol), the vial was heated in a microwave oven for 15 minutes at 210 W. After cooling down to ambient temperature, the mixture was poured into an aqueous solution of LiCl (5%, 25 mL) and extracted with CH_2Cl_2 (3 × 15 mL). The organic phase was washed with an aqueous solution of LiCl (5%, 3 × 15 mL), a saturated aqueous solution of $NaHCO_3$ (1 × 15 mL) and dried over Na_2SO_4. The solvent was distilled off under reduced pressure and the residue was purified by column chromatography [SiO_2, hexane/EtOAc (30:10, v/v)] to give **6** (10.7 mg, 21%) as a blue solid. HRESIMS: *m/z* calcd for $C_{42}H_{41}BF_2N_4O_2$: 682.3291; found: 683.3382 $[M + H]^+$; ^1H NMR (400 MHz, $CDCl_3$): $\delta = 8.23$ (d, 8.7 Hz, 2H), 8.15 (d, 17.3 Hz, 1H), 7.70–7.61 (m, 2H), 7.54 (m, 2H), 7.53–7.48 (m, 4H), 7.36 (d, 16.2 Hz, 1H), 7.33–7.28 (m, 2H), 7.28–7.21 (m, 1H), 7.18 (d, 16.2 Hz, 1H), 2.72–2.57 (m, 5H), 2.34 (q, 7.4 Hz, 2H), 1.66 (s, 6H), 1.32 (s, 3H), 1.31 (s, 3H), 1.16 (t, 7.5 Hz, 3H), 1.01 (t, 7.5 Hz, 3H).

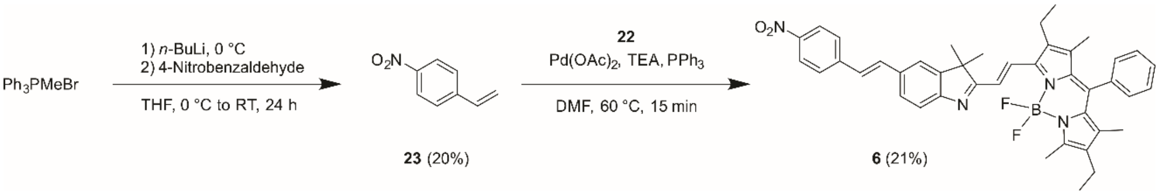

Figure 2.8. Synthesis of **6**.

7. A solution of catecholborane (0.167 mmol, 1 M) in THF (5.99 mL) was added to 4-ethynyl-*N*,*N*-dimethylaniline (22 mg, 0.152 mmol) maintained under Ar. The mixture was diluted with THF (0.5 mL) and heated at 85 °C for 1 hour. After cooling down to ambient temperature and further dilution with THF (5 mL), a solution of **22** (50 mg, 76 μmol), $Pd(PPh_3)_4$ (9 mg, 7.6 μmol) and K_2CO_3 (42 mg, 0.304 mmol) in H_2O (1 mL) were added. The mixture was heated under reflux for 4 hours and, after cooling down to ambient temperature, diluted with H_2O (15 mL) and extracted with EtOAc (3 × 15 mL). The organic phase was dried over Na_2SO_4 and the solvent was distilled off under reduced pressure. The residue was purified by column chromatography [SiO_2, hexane/CH_2Cl_2/EtOAc (30:10:10, v/v/v)] first and then by preparative thin-layer chromatography [SiO_2, hexane/EtOAc (20:10 v/v)] to give **7** (10 mg, 19%) as a blue solid. HRESIMS: *m/z* calcd for $C_{44}H_{47}BF_2N_4$: 680.3862; found: 681.3956 $[M + H]^+$; ^1H NMR (500 MHz, $CDCl_3$) δ 8.13 (d, 17.3 Hz, 1H), 7.58 (d, 8.0 Hz, 1H), 7.52–7.46 (m, 4H), 7.44 (d, 3H), 7.33–7.21 (m, 3H), 7.10 (d, 16.3 Hz, 1H), 7.00 (d, 16.2 Hz, 1H), 6.74 (d, 8.4 Hz, 2H), 3.00 (s, 6H), 2.68–2.56 (m, 5H), 2.34 (q, 7.5 Hz, 2H), 1.66 (s, 6H), 1.32 (s, 3H), 1.30 (s, 3H), 1.12 (t, 7.5 Hz, 3H), 1.01 (t, 7.5 Hz, 3H).

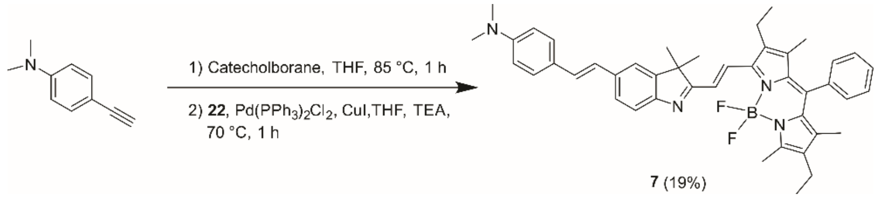

Figure 2.9. Synthesis of **7**.

9. $Pd(PPh_3)_2Cl_2$ (1.6 mg, 2.3 μmol) was added to a degassed solution of **22** (50 mg, 76 μmol) in a mixture of THF (4.5 mL) and TEA (0.5 mL) maintained under Ar. After 5 minutes of stirring, CuI (0.44 mg, 2.3 μmol) and **24** (22.4 mg, 152 μmol) were added. The mixture was heated up to 70 °C and stirred at this temperature for 1 hour. After cooling down to ambient temperature, the solvent was distilled off under reduced pressure. The residue was purified by column chromatography [SiO_2, hexane/EtOAc (40:10 → 20:10, v/v)] to give **9** (24 mg, 46%) as a blue solid. HRESIMS: *m/z* calcd for $C_{42}H_{39}BF_2N_4O_2$: 680.3134; found: 681.3215 $[M + H]^+$; ^1H NMR (400 MHz, $CDCl_3$): δ = 8.25 (d, 8.8 Hz, 2H), 8.18 (d, 17.3 Hz, 1H), 7.70 (d, 8.8 Hz, 2H), 7.65 (d, 7.9 Hz, 1H), 7.59–7.49 (m, 6H), 7.37–7.20 (m, 2H), 2.72–2.58 (m, 5H), 2.35 (q, 7.5 Hz, 2H), 1.66 (s, 6H), 1.34 (s, 3H), 1.32 (s, 3H), 1.17 (t, 7.5 Hz, 3H), 1.02 (t, 7.5 Hz, 3H).

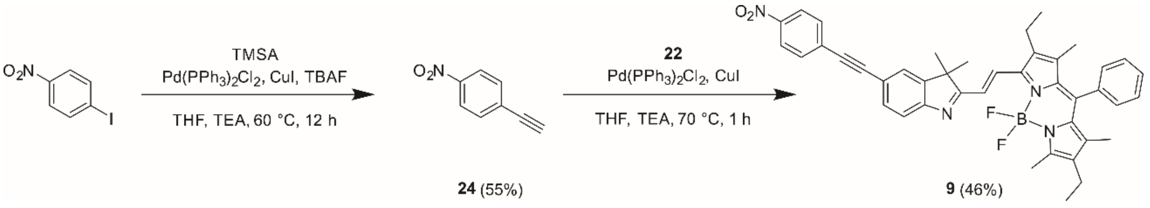

Figure 2.10. Synthesis of **9**.

10. $Pd(PPh_3)_2Cl_2$ (1.6 mg, 2.3 μmol) was added to a degassed solution of **22** (50 mg, 76 μmol) in a mixture of THF (4.5 mL) and TEA (0.5 mL) maintained under Ar. After 5 minutes of stirring, CuI (0.4 mg, 2.3 μmol) and 4-ethynyl-*N*,*N*-dimethylaniline (22 mg, 0.152 mmol) were added. The mixture was heated up to 70 °C and stirred at this temperature for 1 hour. After cooling down to ambient temperature, the solvent was distilled off and the residue was purified by column chromatography [SiO_2, hexane/EtOAc (50:10, v/v)] to give **10** (35 mg, 68%) as a dark blue solid. HRESIMS: *m/z* calcd for $C_{44}H_{45}BF_2N_4$: 678.3705; found: 679.3791 $[M + H]^+$; ^1H NMR (500 MHz, $CDCl_3$) δ = 8.14 (d, 17.3 Hz, 1H), 7.60 (d, 7.9 Hz, 1H), 7.57–7.47 (m, 5H), 7.45 (d, 8.3 Hz, 2H), 7.36–7.30 (m, 2H), 7.25–7.21 (m, 1H), 6.70 (d, 8.3 Hz, 2H), 3.02 (s, 6H), 2.72–2.58 (m, 5H), 2.35 (q, 7.5 Hz, 2H), 1.65 (s, 6H), 1.34 (s, 3H), 1.33 (s, 3H), 1.18 (t, 7.5 Hz, 3H), 1.03 (t, 7.5 Hz, 3H).

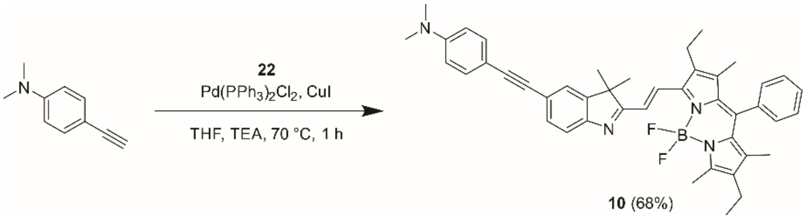

Figure 2.11. Synthesis of **10**.

11. Pd(PPh$_3$)$_2$Cl$_2$ (1.6 mg, 2.3 µmol) was added to a degassed solution of **22** (50 mg, 76 µmol) in a mixture of THF (4.5 mL) and TEA (0.5 mL) maintained under Ar. After 5 minutes of stirring, CuI (0.4 mg, 2.3 µmol) and **28** (37 mg, 0.152 mmol) were added. The mixture was heated up to 70 °C and stirred at this temperature for 1 hour. After cooling down to ambient temperature, the residue was purified by column chromatography [SiO$_2$, hexane/EtOAc (30:20, v/v)] to give **10** (28 mg, 48%) as a dark green solid. HRESIMS: *m/z* calcd for $C_{49}H_{49}BF_2N_4O_2$: 774.3917; found: 775.4030 $[M + H]^+$; ^1H NMR (400 MHz, CDCl$_3$): δ = 8.15 (d, 17.3 Hz, 1H), 7.82 (s, 1H), 7.65–7.46 (m, 6H), 7.37–7.16 (m, 4H), 6.66–6.57 (m, 1H), 6.56–6.48 (m, 1H), 3.45 (q, 7.1 Hz, 4H), 2.76–2.52 (m, 5H), 2.35 (q, 7.0 Hz, 2H), 1.64 (s, 6H), 1.33 (s, 3H), 1.31 (s, 3H), 1.24 (t, 7.9 Hz, 6H), 1.17 (t, 7.5 Hz, 3H), 1.02 (t, 7.5 Hz, 3H).

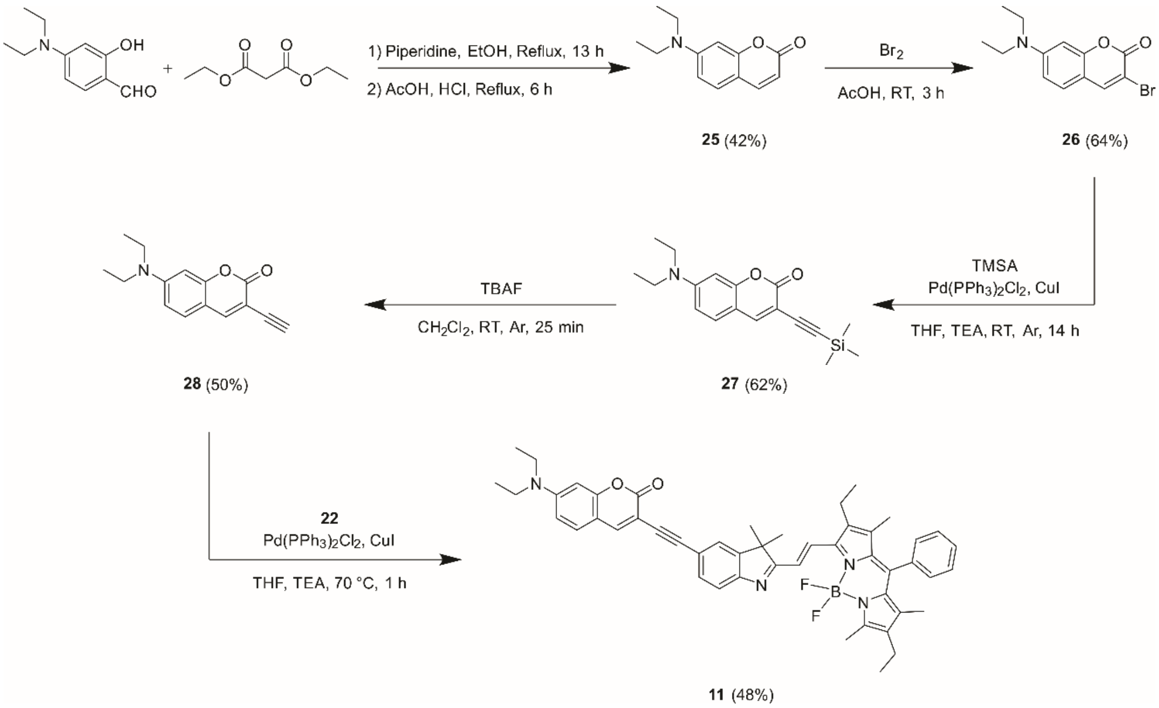

Figure 2.12. Synthesis of **11**.

12. A solution of **5** (90 mg, 135 μmol) and **29** (156 mg, 405 μmol) in MeCN (100 mL) was heated under reflux for 14 hours. After cooling down to ambient temperature, the solvent was distilled off under reduced pressure. The residue was dissolved in EtOAc and washed with a saturated aqueous solution of $NaHCO_3$ (3 × 15 mL). The organic phase was dried over Na_2SO_4 and the solvent was distilled off under reduced pressure. The residue was purified by column chromatography [SiO_2, hexane/EtOAc (50:10, v/v)] to give **12** (20 mg, 18%) as a purple solid. HRESIMS: *m/z* calcd for $C_{50}H_{49}BF_2N_4O_4$: 818.3815; found: 819.3876 $[M + H]^+$; ^{1}H NMR (500 MHz, $CDCl_3$) $\delta = 7.72$ (dd, 2.4 and 7.0 Hz, 1H), 7.53–7.46 (m, 4H), 7.43 (d, 8.6 Hz, 2H), 7.35 (d, 1.7 Hz, 1H), 7.25–7.19 (m, 5H), 6.94 (s, 2H), 6.90 (d, 8.4 Hz, 2H), 6.64 (d, 8.1 Hz, 1H), 6.42 (d, 16.6 Hz, 1H), 5.12 (d, 19.5 Hz, 1H), 4.98 (d, 18.9 Hz, 1H), 3.84 (s, 3H), 2.54 (s, 3H), 2.44 (q, 7.5 Hz, 2H), 2.31 (q, 7.5 Hz, 2H), 1.67 (m, 6H), 1.33–1.26 (m, 6H), 1.04–0.96 (m, 6H).

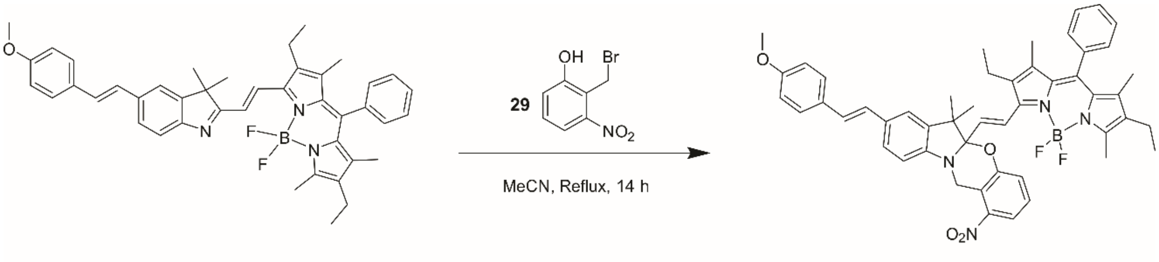

5 12 (18%)

Figure 2.13. Synthesis of **12**.

14. An ice-cold mixture of *N*,*N*-dimethylformamide (DMF, 10.25 mL, 133 mmol) and $POCl_3$ (3.82 mL, 41 mmol) was added dropwise over 20 minutes to a solution of 3-ethyl-2,4-dimethylpyrrole (5 mL, 37 mmol) in dry DMF (15 mL) maintained under Ar at – 30 °C. The resulting yellow mixture was poured onto an ice-cold aqueous solution of NaOH (5%, 30 mL) and stirred for 1 hour. The suspension was filtered and the solid residue was recrystallized from Et_2O/hexane to give **14** (4.99 g, 89%) as an orange solid. HRESIMS: *m/z* calcd for $C_9H_{13}NO$: 151.0997; found: 174.0902 $[M + Na]^+$; ^1H NMR (300 MHz, $CDCl_3$): $\delta = 10.53$ (br s, 1H), 9.45 (s, 1H), 2.40 (q, 7.5 Hz, 2H), 2.29 (s, 6H), 1.07 (t, 7.5 Hz, 3H); ^{13}C NMR (75 MHz, $CDCl_3$): $\delta = 175.47$, 136.44, 132.49, 127.81, 124.86, 16.96, 15.07, 11.44, 8.73.

15. $POCl_3$ (3.15 mL, 33.8 mmol) was added dropwise to a solution of **14** (4.27 g, 28.2 mmol) in CH_2Cl_2 (140 mL) maintained under Ar at 0 °C. The stirred mixture was allowed to warm up to ambient temperature. After 12 hours, it was cooled down to 0 °C and triethylamine (TEA, 19.6 mL, 141 mmol) was added dropwise. After 15 minutes, BF_3OEt_2 (28.4 mL, 226 mmol) was added dropwise and the mixture was stirred at ambient temperature for 36 hours. The mixture was poured over ice and allowed to warm up to ambient temperature with stirring. The organic layer was separated, washed with a saturated aqueous solution of $NaHCO_3$ (3 × 100 mL) and dried over Na_2SO_4. The solvent was distilled off under reduced pressure and the residue was purified by column chromatography [SiO_2, hexane/EtOAc (60:10, v/v)] to give **15** (3.7 g, 86%) as a dark red solid. HRESIMS: *m/z* calcd for $C_{17}H_{23}BF_2N_2$: 304.1922; found: 327.1820 $[M + Na]^+$; ^1H NMR (300 MHz, $CDCl_3$): δ = 6.97 (s, 1H), 2.52 (s, 6H), 2.40 (q, 7.5 Hz, 4H), 2.17 (s, 6H), 1.08 (t, 7.5 Hz, 6H); ^{13}C NMR (75 MHz, $CDCl_3$): δ = 154.60, 136.68, 132.42, 131.61, 118.60, 17.28, 14.61, 12.54, 9.37.

16. A degassed solution of 2,3-dichloro-5,6-dicyanoquinone-1,4-benzoquinone (DDQ, 8.95 g, 39.44 mmol) in THF (80 mL) was added dropwise to a degassed solution of **15** (3 g, 9.86 mmol) in a mixture of THF (240 mL) and H_2O (2.4 mL) maintained under Ar at 0 °C. The stirred mixture was allowed to warm up to ambient temperature. After 23 hours, the solvent was distilled off under reduced pressure. The residue was dissolved in EtOAc (100 mL), washed with H_2O (2 × 100 mL) and a saturated aqueous solution of NaCl (100 mL). The organic phase was dried over Na_2SO_4 and the solvent was distilled off under reduced pressure. The residue was purified by column chromatography [SiO_2, hexane/EtOAc (50:10, v/v)] to give **16** (0.96 g, 31%) as a red solid. HRESIMS: *m/z* calcd for $C_{17}H_{21}BF_2N_2O$: 318.1715; found: 341.1628 $[M + Na]^+$; ^1H NMR (400 MHz, $CDCl_3$): δ = 10.30 (s, 1H), 7.12 (s, 1H), 2.77 (q, 7.6 Hz, 2H), 2.62 (s, 3H), 2.44 (q, 7.6 Hz, 2H), 2.23 (s, 3H), 2.18 (s, 3H), 1.12 (t, 7.6 Hz, 3H), 1.11 (t, 7.6 Hz, 3H); ^{13}C NMR (75 MHz, $CDCl_3$): δ = 185.37, 168.06, 142.21, 140.38, 138.32, 136.93, 136.14, 133.20, 132.62, 120.37, 18.02, 17.32, 14.34, 13.98, 13.81, 9.56, 8.65.

17. A solution of *n*-BuLi (20.41 mmol, 1.6 M) in hexane (12.74 mL) was added dropwise over 10 minutes to a solution of $MePh_3PBr$ (7.29 g, 20.41 mmol) in THF (50 mL) maintained under Ar at 0 °C. After stirring at this temperature for 15 minutes, 4-methoxybenzaldehyde (2.53 g, 18.55 mmol) was added and the mixture was allowed to warm up to ambient temperature. After 24 hours, the solvent was distilled off under reduced pressure. The residue was triturated with hexane (40 mL) and passed through a silica plug. The solvent was distilled off under reduced pressure to give **17** (1.87 g, 75%) as a colorless oil. ^1H NMR (400 MHz, $CDCl_3$): $\delta = 7.37$ (d, 8 Hz, 2H), 6.88 (d, 8 Hz, 2H), 6.68 (dd, 8 and 20 Hz, 1H), 5.63 (d, 20 Hz, 1H), 5.14 (d, 8 Hz, 1H), 3.83 (s, 3 H).

19. $(Ph_3P)_2PdCl_2$ (123 mg, 0.18 mmol) was added to a degassed solution of **18** (500 mg, 1.75 mmol), K_2CO_3 (726 mg, 5.25 mmol) and Bu_4NBr (36 mg, 0.11 mmol) in H_2O (10 mL) maintained under Ar in a pressure vial. The vial was capped and shaken for 10 minutes. After the addition of **17** (353 mg, 2.63 mmol), the mixture was bubbled with Ar for a further 5 minutes and heated in a microwave oven for 10 minutes at 210 W. After cooling down to ambient temperature, the mixture was extracted with CH_2Cl_2 (3 × 10 mL). The organic phase was dried over Na_2SO_4 and the solvent was distilled off under reduced pressure. The residue was purified by column chromatography [SiO_2, CH_2Cl_2/hexane/EtOAc (60:20:10, v/v)] to give **19** (120 mg, 23%) as an orange solid. HRESIMS: *m/z* calcd for $C_{20}H_{21}NO$: 291.1623; found: 292.1701 $[M + H]^+$; ^1H NMR (400 MHz, $CDCl_3$): $\delta = 7.52–7.41$ (m, 3H), 7.47 (d, 8.0 Hz, 2H), 7.07 (d, 16 Hz, 1H), 7.03 (d, 16 Hz, 1H), 6.92 (d, 8 Hz, 1H), 3.84 (s, 3H), 2.30 (s, 3H), 1.35 (s, 6H).

21. Catecholborane (242 μL, 2.27 mmol) was added dropwise to 4-ethynylanisole (300 mg, 2.27 mmol) maintained under Ar at 0 °C. The mixture was heated up to 75 °C and stirred at this temperature for 3 hours. After cooling down to ambient temperature, the mixture was diluted with H_2O (2 mL), heated up to 80 °C and stirred at this temperature for 2 hour. The mixture was further diluted with H_2O (10 mL), heated under reflux for 5 minutes and filtered over a cotton plug. Upon cooling down to ambient temperature, crystals precipitated out of the filtrate. The crystals were filtered out and dried to give **21** (130 mg, 32%) as a white solid. ^{1}H NMR [400 MHz, $(CD_3)_2SO$]: δ = 7.67 (s, 2H), 7.39 (d, 8.3 Hz, 2H), 7.18 (d, 18.4 Hz, 1H), 6.91 (d, 8.3 Hz, 2H), 5.92 (d, 18.4 Hz, 1H), 3.75 (s, 3H).

23. A solution of *n*-BuLi (18.19 mmol, 1.6 M) in hexane (11.3 mL) was added dropwise over 10 minutes to a solution of $MePh_3PBr$ (6.50 g, 18.19 mmol) in THF (50 mL) maintained under Ar at 0 °C. After stirring at this temperature for a further for 15 minutes, 4-nitrobenzaldehyde (2.50 g, 16.54 mmol) was added and the mixture was allowed to warm up to ambient temperature. After 24 hours, the solvent was distilled off under reduced pressure. The residue was purified by column chromatography [SiO_2, hexane/MeAc (95:5 v/v)] to give **23** (493 mg, 20%) as a white solid. ^{1}H NMR (400 MHz, $CDCl_3$): δ = 8.21 (d, 8.8 Hz, 2H), 7.55 (d, 8.8 Hz, 2H), 6.80 (dd, 10.9 and 17.7 Hz, 1H), 5.94 (d, 17.7 Hz, 1H), 5.51 (d, 10.9 Hz, 1H).

24. $Pd(PPh_3)_2Cl_2$ (84 mg, 0.12 mmol) was added to a degassed solution of 1-iodo-4-nitrobenzene (1 g, 4 mmol) in a mixture of THF (49 mL) and TEA (6 mL) maintained under Ar. After 5 minutes of stirring, CuI (23 mg, 0.12 mmol) and trimethylsilylacetylene

(TMSA, 1.14 mL, 8 mmol) were added. The mixture was heated up to 60 °C, stirred at this temperature for 12 hours and filtered. The filtrate was cooled with an ice bath and a solution of tetrabutylammonium fluoride (TBAF, 8 mmol, 1 M) in THF (8 mL) was added dropwise. The mixture was allowed to warm up to ambient temperature and stirred under these conditions for 30 minutes. The solvent was distilled off under reduced pressure and the residue was purified by column chromatography [SiO_2, hexane/EtOAc (20:10, v/v)] to give **24** (324 mg, 55%) as a yellow solid. ^1H NMR (400 MHz, $CDCl_3$): $\delta = 8.21$ (d, 8.8 Hz, 2H), 7.65 (d, 8.8 Hz, 2H), 3.37 (s, 1H).

25. A solution of 4-(diethylamino)salicylaldehyde (1 g, 5.17 mmol), diethylmalonate (1.57 mL, 10.34 mmol) and piperidine (255 µL, 2.59 mmol) in EtOH (20 mL) was heated under reflux for 13 hours. After cooling down to ambient temperature, the solvent was distilled off under reduced pressure. The residue was dissolved in a mixture of glacial AcOH (10 mL) and concentrated HCl (10 mL) and heated under reflux for 6 hours. After cooling down to ambient temperature, the mixture was poured over ice-cold H_2O (50 mL) and the pH was adjusted to *ca.* 7 with aqueous KOH (1 M). The resulting precipitate was filtered off and dried to give **25** (0.57 g, 42%) as a brown solid. ^1H NMR (300 MHz, $CDCl_3$): $\delta =$ 7.55 (d, 9.4 Hz, 1H), 7.26 (d, 9.4 Hz, 1H), 6.58 (d, 9.1 Hz, 1H), 6.51 (m, 1H), 6.05 (d, 9.1 Hz, 1H), 3.43 (q, 7.2 Hz, 4H), 1.23 (t, 7.1 Hz, 6H).

26. Br_2 (131 µL, 2.55 mmol) was added dropwise to a solution of **25** (0.56 mg, 2.55 mmol) and glacial AcOH (6 mL). The mixture was stirred at ambient temperature for 3 hours. The suspension was filtered and the solid residue was recrystallized from MeCN to give **26** (0.48 mg, 64%) as white crystals. HRESIMS: *m/z* calcd for $C_{13}H_{14}BrNO_2$: 295.0208;

found: 296.0288 $[M + H]^+$; ^1H NMR [400 MHz, $(CD_3)_2SO$]: δ = 8.34 (s, 1H), 7.43 (d, 8.9 Hz, 1H), 6.74 (dd, 2.4 and 8.9 Hz, 1H), 6.62–6.50 (m, 1H), 3.43 (q, 7.0 Hz, 4H), 1.11 (t, 7.0 Hz, 6H).

27. $Pd(PPh_3)_2Cl_2$ (56.2 mg, 80 μmol) was added to a degassed solution of **26** (50 mg, 76 μmol) in a mixture of THF (18 mL) and TEA (2 mL) maintained under Ar. After 5 minutes of stirring, CuI (15.2 mg, 80 μmol) and TMSA (436 μL, 3.06 mmol) were added. The mixture was stirred at ambient temperature for 14 hours. The solvent was distilled off under reduced pressure and the residue was purified by column chromatography [SiO_2, hexane/EtOAc (40:10, v/v)] to give **27** (0.3 g, 62%) as a yellow solid. ^1H NMR (300 MHz, $CDCl_3$): *δ*= 7.78 (s, 1H), 7.23 (d, 8.7 Hz, 1H), 6.59 (d, 8.7 Hz, 1H), 6.53–6.43 (m, 1H), 3.44 (q, 7.2 Hz, 4H), 1.23 (t, 6.3 Hz, 6H), 0.28 (s, 9H).

28. A solution of TBAF (1.91 mmol, 1 M) in THF (1.91 mL) was added dropwise to a solution of **27** (0.3 g, 0.95 mmol) in CH_2Cl_2 maintained at 0 °C. The mixture was allowed to warm up to ambient temperature and stirred for 25 minutes. The solvent was distilled off under reduced pressure and the residue was purified by column chromatography [SiO_2, hexane/EtOAc (40:10, v/v)] to afford **28** (0.2 g, 87%) as a yellow solid. HRESIMS: *m/z* calcd for $C_{15}H_{15}NO_2$: 241.1103; found: 242.1192 $[M + H]^+$; ^1H NMR (400 MHz, $CDCl_3$): δ = 7.78 (s, 1H), 7.24 (d, 8.8 Hz, 1H), 6.59 (dd, 2.5 and 8.8, 2.5 Hz, 1H), 6.52–6.40 (m, 1H), 3.43 (q, 7.1 Hz, 4H), 3.26 (s, 1H), 1.22 (t, 7.1 Hz, 6H).

Crystallographic Analysis. Single crystals of **5**, suitable for diffraction analysis, grew from an EtOAc solution of the compound after the diffusion of pentane vapors at ambient temperature. The data crystal was mounted onto the end of a thin glass fiber using

Paratone-N for data collection at 100 K under N_2. X-ray intensity data were measured by using a Bruker SMART APEX2 CCD-based diffractometer using Mo Kα radiation (λ = 0.71073 Å).[84] The raw data frames were integrated with the SAINT+ program by using a narrow-frame integration algorithm.[84] Corrections for Lorentz and polarization effects were also applied with SAINT+. An empirical absorption correction based on the multiple measurement of equivalent reflections was applied using the program SADABS. All structures were solved by a combination of direct methods and difference Fourier syntheses, and refined by full-matrix least-squares on F^2, by using the SHELXTL software package.[85-86] All non-hydrogen atoms were refined with anisotropic displacement parameters. Hydrogen atoms were placed in geometrically-idealized positions and included, as standard riding atoms, during the least squares refinements. Crystal data, data collection parameters and results of the analyses are listed in Table 2.2. Compound **5** crystallized in the monoclinic crystal system. The systematic absences in the intensity data identified the unique space group $P2_1/c$.

Polymer Nanoparticles. CH_2Cl_2 solutions of **12** (0.5 mg mL^{-1} for imaging or 0.1 mg mL^{-1} for spectroscopy, 50 μL) and **13** (25 mg mL^{-1} for imaging, 2.5 mg mL^{-1} for spectroscopy, 200 μL) were combined and heated at 40 °C in an open vial. After the evaporation of the solvent, the residue was purged with air, dispersed in Dulbecco's PBS (pH = 7.2–7.6, 1.0 mL), sonicated for 5 min and flashed through a syringe filter with a pore size of 0.2 μm. The filtrate was used for the imaging and spectroscopic experiments without any further purification.

Polymer Films. Doped polymer films were prepared by spin coating CH_2Cl_2 solutions of PMMA (120 kDa, 10 mg mL^{-1}) and **12** (50 µg mL^{-1}) with a Chemat Technologies KW-4A spin coater at 1200 rpm for 30 s on glass coverslips.

Spectroscopy. Absorption spectra were recorded with a Varian Cary 100 Bio spectrometer in quartz cells with a path length of 1.0 cm. Emission spectra were recorded with a Varian Cary Eclipse spectrometer in aerated solutions. Fluorescence quantum yields were determined against a MeCN solution of **3** ($\Phi_F = 0.50$),[1] following a literature protocol.[87] Fluorescence decays were recorded at 580–780 nm with a PicoQuant Fluotime 200 time-correlated single photon counting system, using pulsed excitation at either 505 nm (10 MHz pulse repetition rate, 900 ps pulse width, ~0.3 pJ per pulse) or 596 nm (10 MHz pulse repetition rate, 950 ps pulse width, ~0.3 pJ per pulse) and a Picoquant's PMA 182-M single photon detector. The excitation source worked at a repetition rate of 10 MHz and the photon-counting frequency was kept always below 1%. Time-resolved emission signals were analyzed by fitting the convolution of the instrument's response function with a multiexponential decay model, using the PicoQuant FluoFit 4.0 software. The time resolution of the system is approximately 100 ps. The number of exponentials in the model function and the corresponding goodness of the fit was judged by the distribution of residuals and the value of the χ^2 parameter. Photolyses were performed in aerated solutions with a Luzchem Research LZC-4V photoreactor, operating at 350 nm (4.2 mW cm^{-2}), and the corresponding quantum yields were determined with a potassium ferrioxalate actinometer, according to an established procedure.[88] Chromatograms were recorded with a Phenomenex Kinetex (5 µm EVO C18 100 Å) column (4.6 × 250 mm) operated with a

Shimadzu Nexera X2 system in MeCN/H_2O (95:5 → 100:0, v/v) at a flow rate of 1.5 mL min^{-1} and detection wavelength of 350 nm.

Cyclic Voltammetry. Voltammograms were recorded with a CH Instruments 610A electrochemical analyzer in MeCN under Ar, using a three-electrode cell. The reference was a Ag/Ag^+ electrode (1 mM $AgNO_3$ in MeCN). The counter and working were a platinum wire and a glassy-carbon electrode respectively. The supporting electrolyte was Bu_4NPF_6 (0.1 M). The scan rate was 100 mV s^{-1}.

Computational Methods. DFT and TD DFT calculations were performed with Gaussian 09.[89] Geometry optimizations, frequency calculations, molecular orbitals and excitation energies were computed with the 6-311+G(d,p) basis set and the restricted B3LYP functional.[90-91] Dihedral scans were carried out with the 3-21G basis set and the same functional. The geometry with the largest energy found for each scan was optimized further with frozen dihedral, the 6-311+G(d,p) basis set and the same functional. All calculations were performed with the polarizable continuum model (PCM) for acetonitrile, using the integral equation formalism (IEF) variant.[92]

Fluorescence Imaging. *Drosophila melanogaster* embryos (Stock #30030, Bloomington *Drosophila* Stock Center NIH P40OD018537) were prepared for the imaging experiments adapting a literature protocol.[93] Specifically, fertilized egg cells were collected after 60–120 min from laying (stage 2–4), deposited on glass slides and maintained in a desiccator, together with $CaSO_4$, at ambient temperature for 8 min. The slides were covered with a mixture (7:1, v/v) of Series 700 (Sigma H8898) and Series 27 (Sigma H8773) halocarbon oils and transferred individually on the stage of a Leica DMIL LED inverted microscope.

Solutions of the doped polymer nanoparticles in Dulbecco's PBS (pH = 7.2–7.6) were injected in the embryos with a MN151 Narishige micromanipulator. The slides were mounted on the stage of a Leica SP5 confocal laser-scanning microscope and imaged.

Table 2.2. Crystallographic data for Compound 5.

	5
Empirical Formula	$C_{43}H_{44}ON_3F_2B$
Formula Weight	667.62
Crystal System	Monoclinic
Lattice Parameters	
a (Å)	18.9096(9)
b (Å)	8.3146(4)
c (Å)	24.1510(11)
β (deg)	108.948(1)
V (Å^3)	3591.4(3)
Space group	$P2_1/c$ (# 14)
Z Value	4
ρ_{calc} (g cm^{-3})	1.235
μ(Mo Kα) (mm^{-1})	0.081
T (K)	100
$2\Theta_{max}$ (°)	52.0
No. Obs. (I > 2σ(I))	5734
No. Parameters	459
Goodness of Fit	1.030
Max. Shift in Cycle	0.003
*Residuals**: R1; wR2	0.0395; 0.0929
Absorption Correction,	*Multi-Scan*
Max/Min	0.7457/0.6831
Largest Peak in Final Diff. Map (e$^-$ Å^{-3})	0.233

*R1 = $\Sigma_{hkl}(\left|\left|F_{obs}\right| - \left|F_{calc}\right|\right|)/\Sigma_{hkl}\left|F_{obs}\right|$; wR2 = $[\Sigma_{hkl}w(\left|F_{obs}\right| - \left|F_{calc}\right|)^2/\Sigma_{hkl}wF_{obs}^2]^{1/2}$; w = $1/\sigma^2(F_{obs})$; GOF = $[\Sigma_{hkl}w(\left|F_{obs}\right| - \left|F_{calc}\right|)^2/(n_{data} - n_{vari})]^{1/2}$.

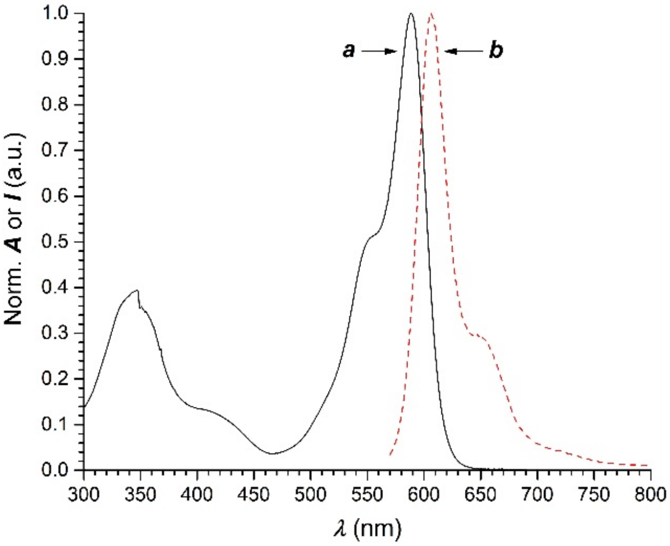

Figure 2.14. Normalized absorption (***a***) and emission (***b***, λ_{Ex} = 560 nm) spectra of **3** in MeCN at 20 °C.

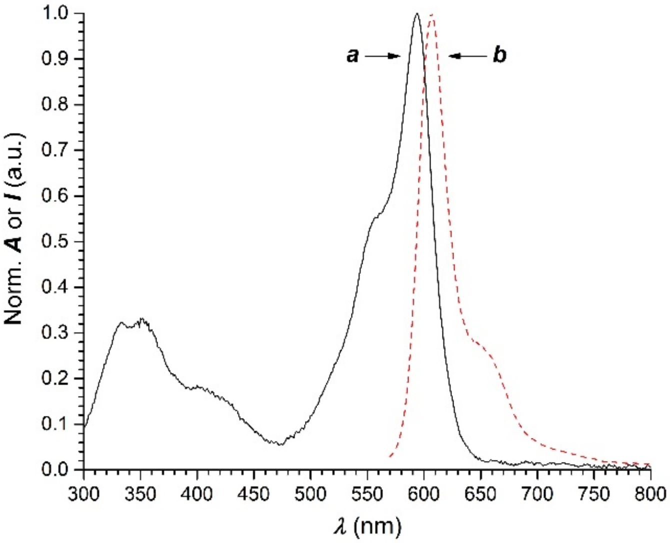

Figure 2.15. Normalized absorption (***a***) and emission (***b***, λ_{Ex} = 560 nm) spectra of **4** in MeCN at 20 °C.

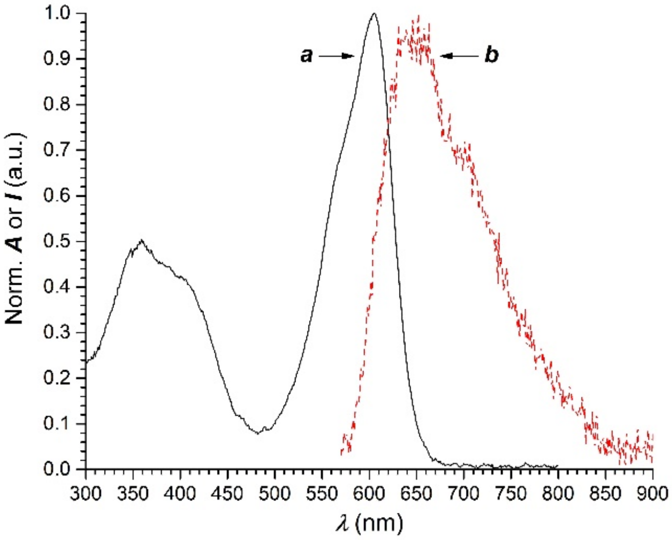

Figure 2.16. Normalized absorption (***a***) and emission (***b***, λ_{Ex} = 560 nm) spectra of **5** in MeCN at 20 °C.

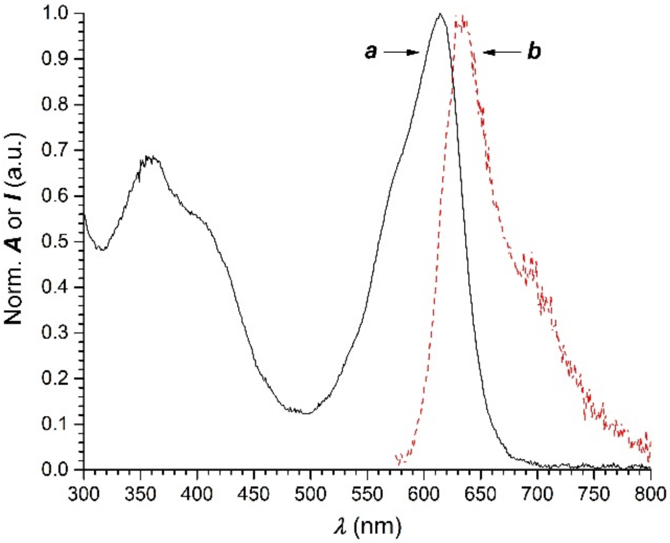

Figure 2.17 Normalized absorption (***a***) and emission (***b***, λ_{Ex} = 560 nm) spectra of nanoparticles of **13**, containing **5**, in H_2O at 20 °C.

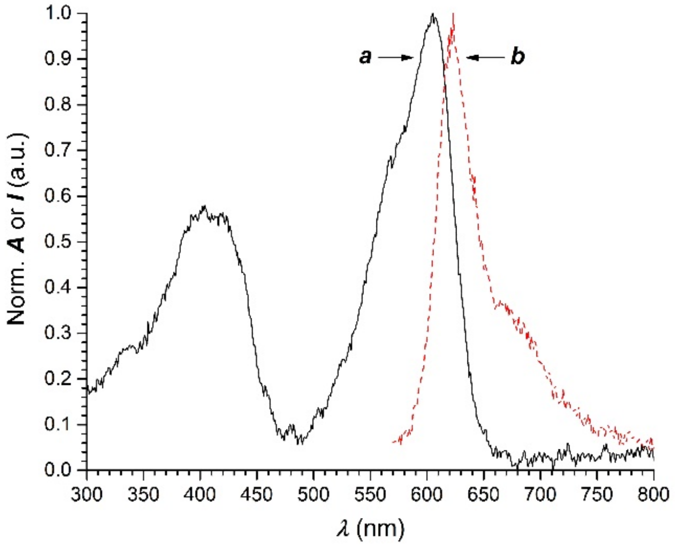

Figure 2.18. Normalized absorption (***a***) and emission (***b***, λ_{Ex} = 560 nm) spectra of **6** in MeCN at 20 °C.

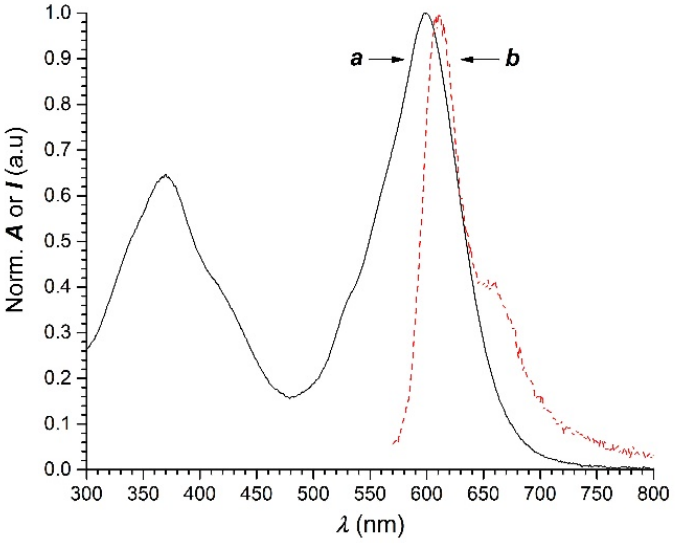

Figure 2.19. Normalized absorption (***a***) and emission (***b***, λ_{Ex} = 560 nm) spectra of **7** in MeCN at 20 °C.

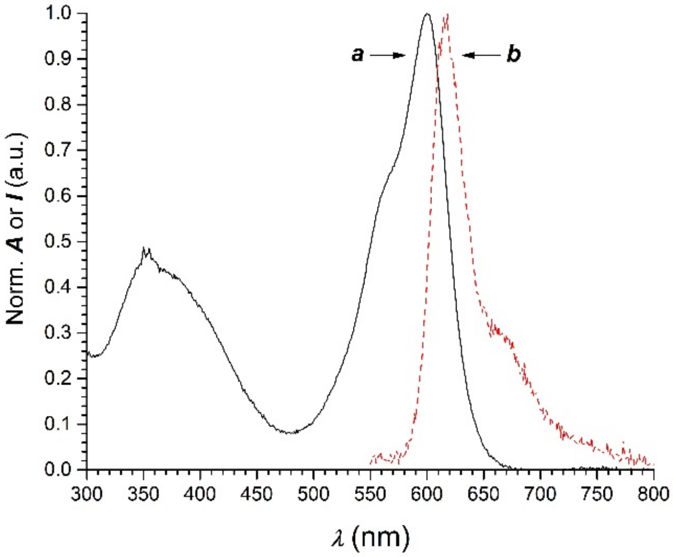

Figure 2.20. Normalized absorption (***a***) and emission (***b***, λ_{Ex} = 540 nm) spectra of **8** in MeCN at 20 °C.

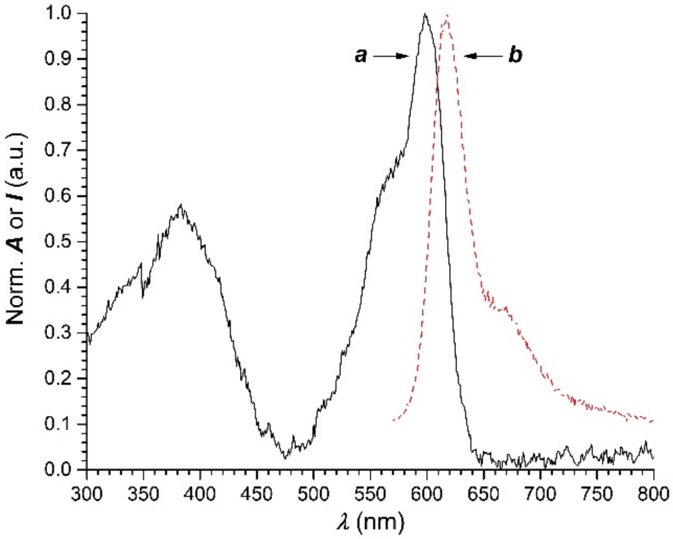

Figure 2.21. Normalized absorption (***a***) and emission (***b***, λ_{Ex} = 560 nm) spectra of **9** in MeCN at 20 °C.

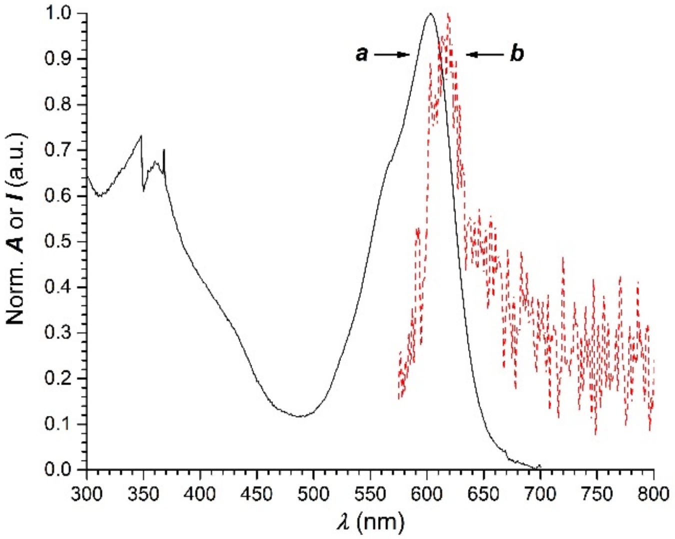

Figure 2.22. Normalized absorption (***a***) and emission (***b***, λ_{Ex} = 560 nm) spectra of **10** in MeCN at 20 °C.

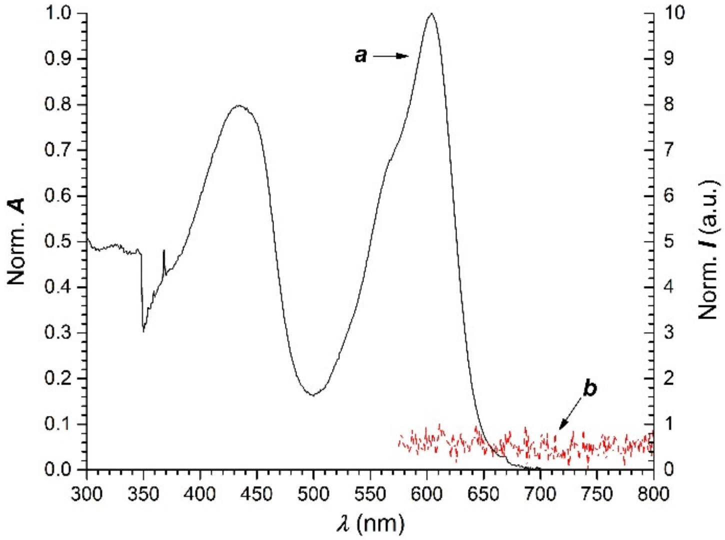

Figure 2.23. Normalized absorption (***a***) and emission (***b***, λ_{Ex} = 560 nm) spectra of **11** in MeCN at 20 °C.

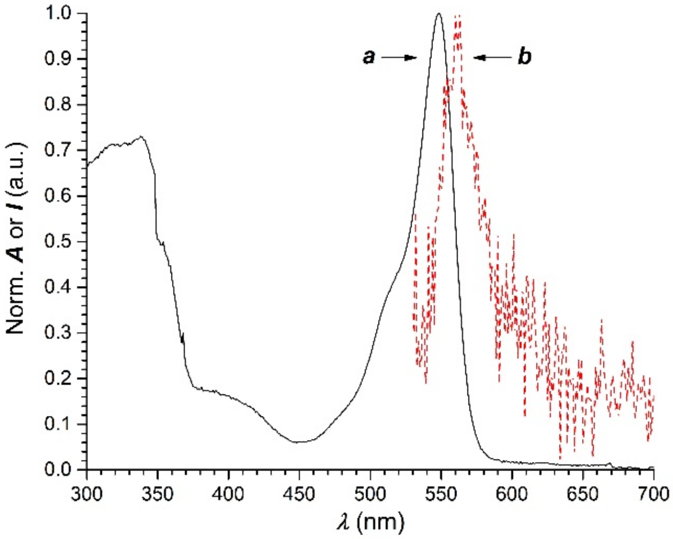

Figure 2.24. Normalized absorption (***a***) and emission (***b***, λ_{Ex} = 540 nm) spectra of **12** in MeCN at 20 °C.

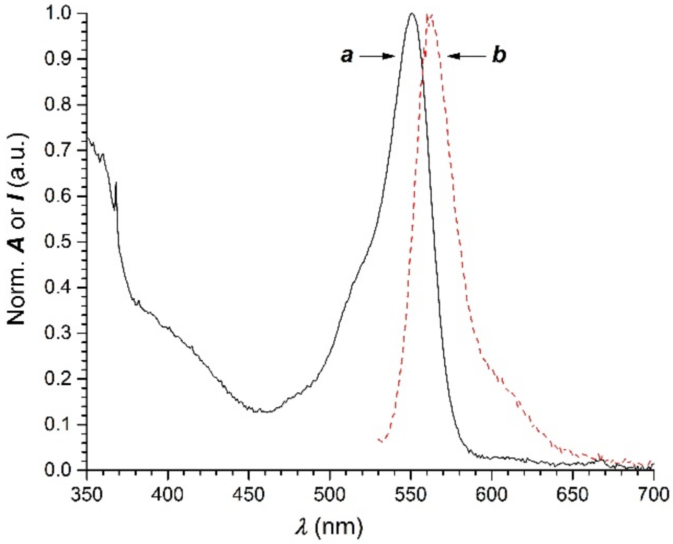

Figure 2.25. Normalized absorption (***a***) and emission (***b***, λ_{Ex} = 540 nm) spectra of nanoparticles of **13**, containing **12**, in H_2O at 20 °C.

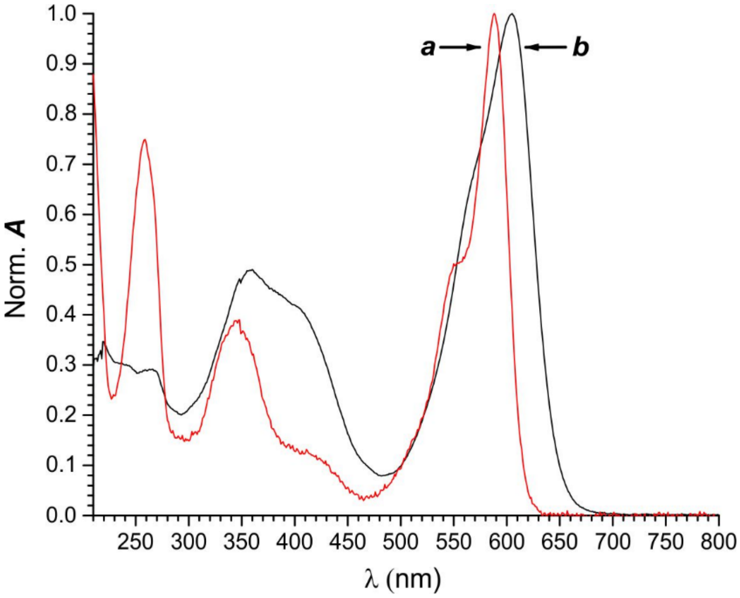

Figure 2.26. Sum (***a***) of the absorption spectra of MeCN solutions (15 µM) of **3** and 4-methoxystyrene at 20 °C together with absorption spectrum (***b***) of **5** under the same conditions.

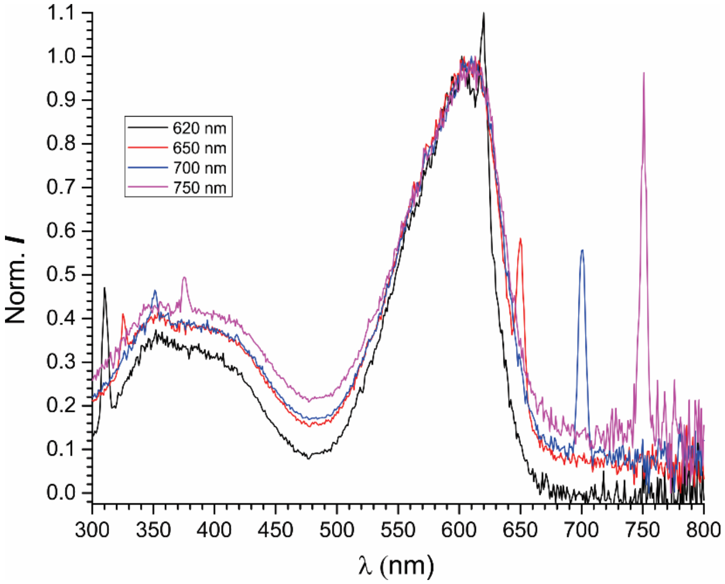

Figure 2.27. Excitation spectra of a MeCN solution (10 µM) of **5** recorded with different emission wavelengths at 20 °C.

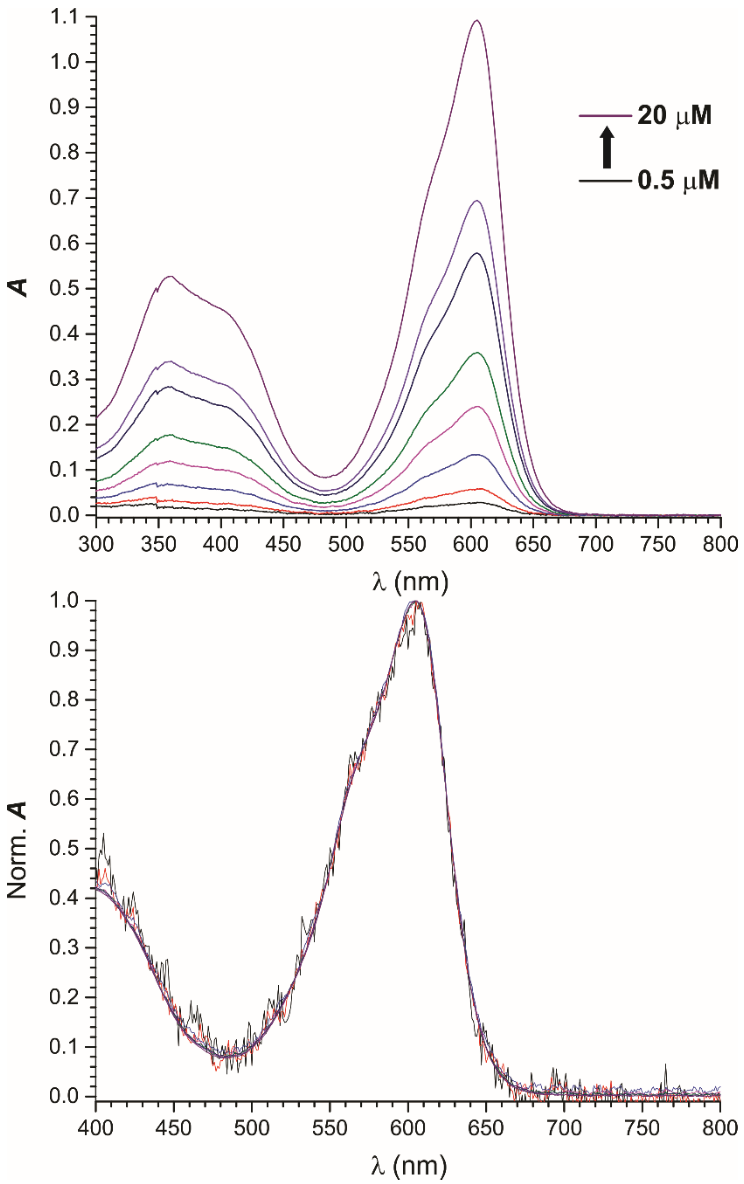

Figure 2.28. Raw and normalized absorption spectra of MeCN solutions of **5** with concentrations ranging from 0.5 to 20 μM at 20 °C.

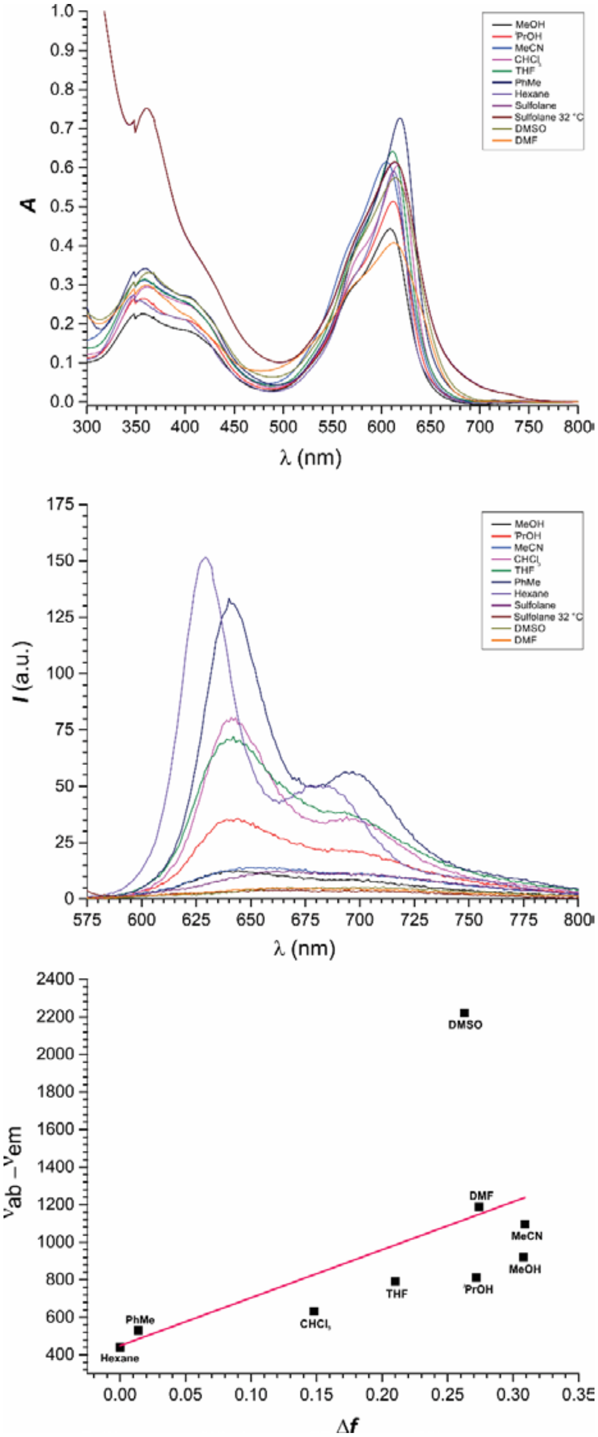

Figure 2.29. Absorption and emission (λ_{Ex} = 560 nm) spectra of **5** in different solvents at 20 °C together with the corresponding Lippert–Mataga plot.

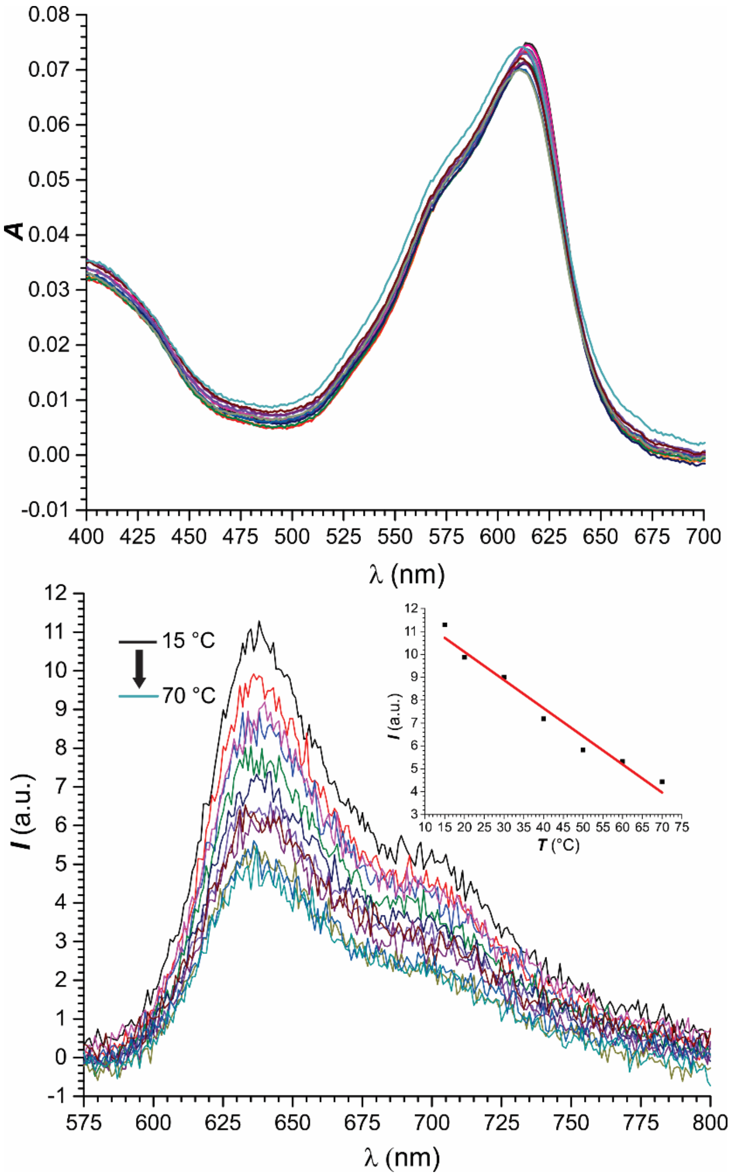

Figure 2.30. Absorption and emission (λ_{Ex} = 560 nm) spectra of a glycerol/*i*-PrOH (1:1, v/v) solution (1.4 µM) of **5** recorded at temperatures ranging from 15 to 70 °C together with the temperature dependence of the emission intensity.

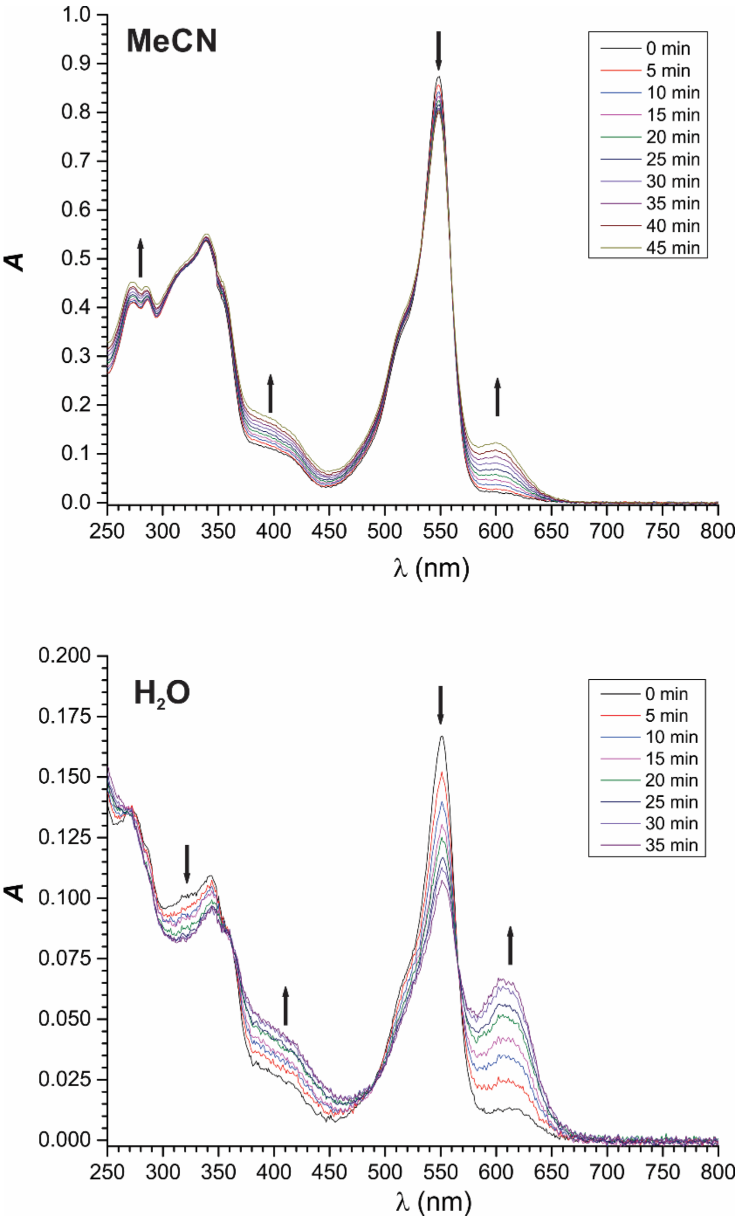

Figure 2.31. Absorption spectra of either a MeCN solution (20 μM) of **12** or a H_2O dispersion of nanoparticles of **13**, containing **12**, recorded before and after irradiation (350 nm, 4.2 mW cm–2) at 20 °C.

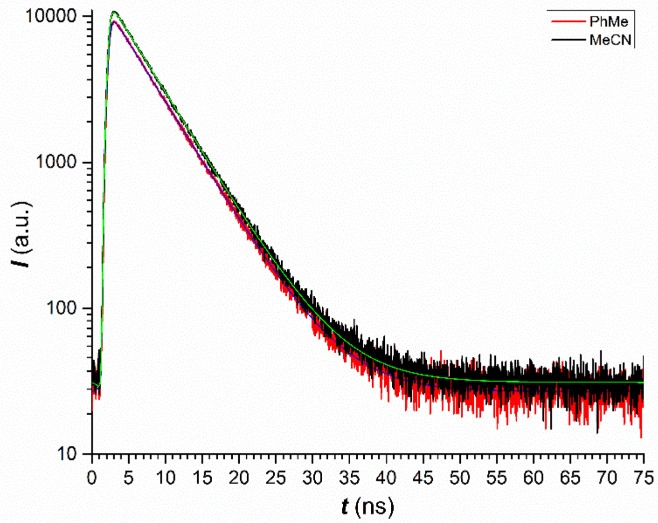

Figure 2.32. Fluorescence decays (λ_{Ex} = 596 nm, λ_{Em} = 630 nm) of MeCN and PhMe solutions (10 µM) of **3** at 20 °C.

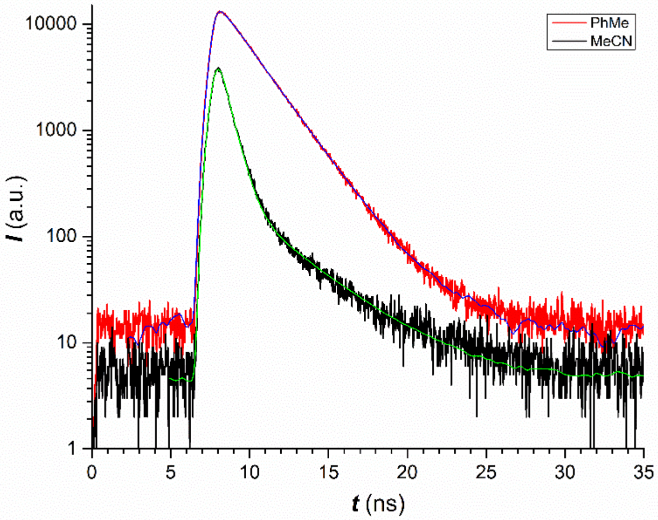

Figure 2.33. Fluorescence decays (λ_{Ex} = 505 nm, λ_{Em} = 645 nm) of MeCN and PhMe solutions (10 µM) of **5** at 20 °C.

Table 2.3. Lifetime (τ) and Pearson's chi-squared parameter (χ^2) for the fitting of the fluorescence decay of 3 and 5 in aerated solutions at 20 °C [*a*].

	Solvent	τ (ns)	χ^2
3	MeCN	5.3	1.037
	PhMe	5.3	0.993
5	MeCN	0.7	0.960
	PhMe	1.9	1.011

[*a*] Fluorescence decays of **3** were measured at 630 nm with excitation at 596 nm and were monoexponential. Those of **5** were collected at 645 nm with excitation at 505 nm and were monoexponential in PhMe and biexponential in MeCN. The value of τ reported for **5** in MeCN was determined from global analysis of the biexponential decay [0.6 ns (94%) and 3.7 ns (4%)].

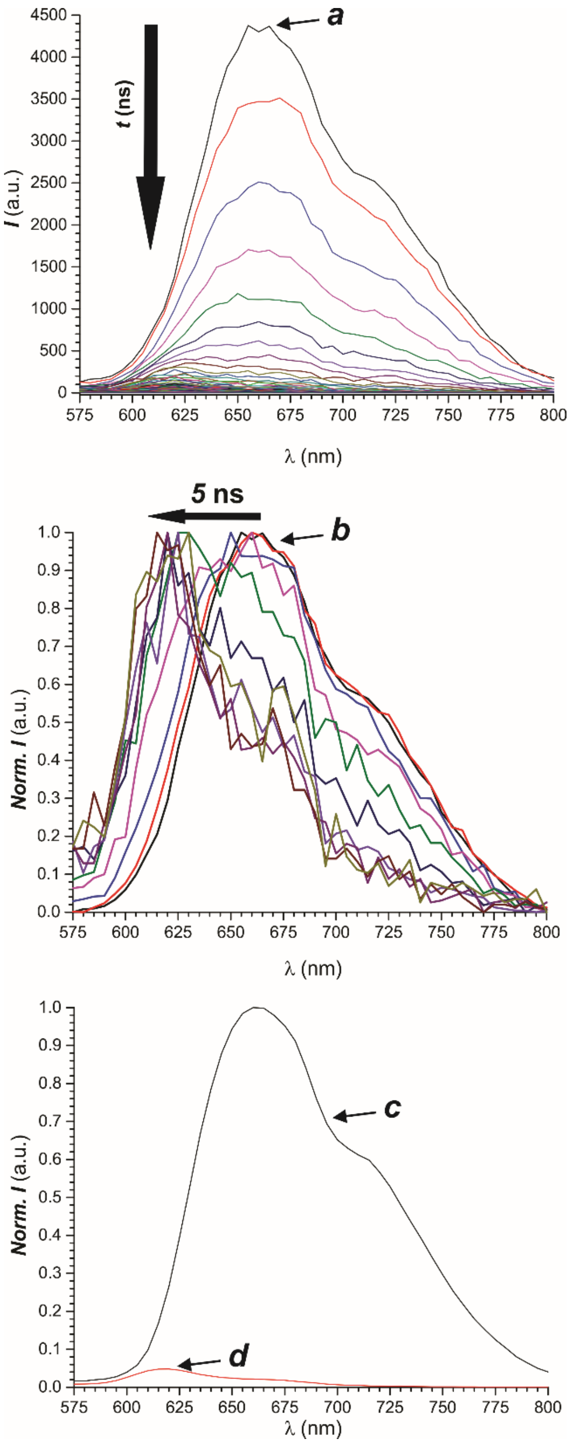

Figure 2.34. Time-resolved emission spectra of MeCN solutions (10 μM) of **5**, recorded over the course of 100 ns after the excitation pulse (λ_{Ex} = 505 nm), plotted on absolute (***a***) and normalized (***b***) scales. Emission spectra of the two components with τ of 0.6 ns (96%, ***c***) and 3.7 ns (4%, ***d***), observed in MeCN, recovered from global analysis of the fluorescence decays.

Optimized Geometry of 5 in the LE State

H	–9.591028000	–1.530514000	2.425550000
H	10.961306000	3.234257000	0.514260000
H	–7.310698000	–0.575198000	2.362852000
H	2.048371000	–0.712717000	2.291311000
C	–9.098467000	–1.375884000	1.472294000
O	13.273598000	2.206733000	0.337468000
C	10.927978000	2.166803000	0.329381000
H	2.440001000	0.926990000	1.752814000
H	8.805488000	2.081427000	0.311945000
C	–7.812990000	–0.837800000	1.438527000
H	0.768111000	0.359714000	1.705204000
H	15.288411000	2.324878000	0.362579000
C	1.806281000	0.058579000	1.556483000
C	9.718486000	1.506127000	0.214129000
H	14.655434000	0.787072000	1.002675000
C	12.138383000	1.464552000	0.207601000
F	–2.256457000	1.453061000	1.237409000

H	–10.749033000	–2.128775000	0.311652000
C	14.538226000	1.548701000	0.226473000
H	–6.351498000	–3.163758000	1.141820000
C	–9.748575000	–1.712285000	0.284981000
H	7.018790000	0.898309000	0.176242000
H	–8.442747000	1.846443000	1.006665000
H	–3.306023000	–4.690385000	0.857827000
H	–5.291779000	–4.355569000	0.388806000
H	–5.684046000	5.674526000	0.470913000
H	–2.436209000	3.761380000	0.481294000
H	–1.691719000	–4.051151000	0.778274000
H	–3.548607000	5.136792000	0.344614000
C	9.660128000	0.116335000	–0.026911000
H	4.716328000	0.832239000	0.297334000
C	12.110099000	0.088705000	–0.033064000
C	–7.165597000	–0.633652000	0.215702000
C	–5.690054000	–3.345728000	0.293225000
C	7.156910000	–0.157705000	–0.040827000

H	–7.318437000	5.067164000	0.470278000
H	14.659857000	1.092010000	–0.759900000
C	–4.574324000	–2.344954000	0.226171000
C	–2.648260000	–4.062663000	0.250986000
C	4.690208000	–0.224038000	0.047569000
H	–0.805790000	–0.154905000	0.317185000
C	–5.788048000	–0.054176000	0.176832000
C	–4.667380000	–0.917318000	0.186465000
C	–3.216053000	–2.669852000	0.196612000
H	13.023516000	–0.481498000	–0.133024000
C	–3.293773000	4.157107000	–0.060923000
B	–3.026170000	1.097031000	0.098383000
C	–5.627706000	1.331517000	0.121718000
C	8.413000000	–0.637136000	–0.155692000
N	–4.344827000	1.895701000	0.080490000
C	2.052790000	–0.449268000	0.117045000
C	–4.464824000	3.236817000	0.020440000
C	5.908343000	–0.909772000	–0.168092000

N	–3.378458000	–0.405090000	0.143999000
C	–6.364190000	5.000874000	–0.058792000
C	10.882122000	–0.562629000	–0.146928000
C	–2.488653000	–1.446249000	0.137435000
C	–6.576030000	2.412219000	0.084389000
C	–5.839129000	3.593693000	0.023640000
C	–8.072342000	2.333411000	0.102034000
C	–1.070775000	–1.181715000	0.112159000
C	3.490419000	–0.901923000	–0.056845000
H	–8.506143000	3.332272000	0.055732000
C	5.859337000	–2.284510000	–0.493799000
C	1.339802000	–1.790220000	–0.162116000
C	–9.107336000	–1.508945000	–0.936809000
C	–0.076778000	–2.067295000	–0.154310000
H	6.780780000	–2.826784000	–0.668254000
H	8.553999000	–1.694927000	–0.362231000
C	3.468537000	–2.266688000	–0.379039000
H	–6.310135000	–3.320071000	–0.605959000

H	–0.305662000	–3.093375000	–0.409181000
H	10.876272000	–1.631448000	–0.334144000
C	4.655558000	–2.969639000	–0.601486000
N	2.165242000	–2.770673000	–0.436699000
C	–7.821100000	–0.972921000	–0.972020000
H	2.309265000	1.516612000	–0.771321000
H	–8.457021000	1.762204000	–0.745781000
H	4.635531000	–4.023877000	–0.853333000
H	–2.991573000	4.300527000	–1.104096000
H	0.642774000	0.933891000	–0.847464000
C	1.687910000	0.631173000	–0.927588000
H	–9.607003000	–1.767207000	–1.863563000
F	–2.262879000	1.391703000	–1.056526000
H	–2.046395000	–5.722304000	–1.028680000
C	–2.476106000	–4.722009000	–1.130318000
H	–6.927764000	6.531650000	–1.506016000
C	–6.549161000	5.505753000	–1.501689000
H	–7.324784000	–0.816746000	–1.923299000

H	–3.439612000	–4.817189000	–1.637800000
H	–5.602723000	5.492730000	–2.048883000
H	–1.819472000	–4.135615000	–1.778504000
H	1.862432000	0.267916000	–1.943045000
H	–7.259572000	4.879210000	–2.047725000

Optimized Geometry 5 in the TICT State

H	9.754199000	–1.716276000	–2.105755000
H	–11.512947000	0.515897000	–2.629451000
H	7.516580000	–0.668110000	–2.214153000
H	–2.412710000	–2.963655000	–0.811378000
C	9.177384000	–1.583763000	–1.197489000
O	–13.582070000	0.763417000	–1.183542000
C	–11.285675000	0.479877000	–1.570307000
H	–2.959827000	–2.032621000	–2.213620000
H	–9.198488000	0.222891000	–1.871144000
C	7.916652000	–0.992750000	–1.260126000
H	–1.232473000	–2.279263000	–1.939067000

H	–15.571016000	1.001312000	–0.935705000
C	–2.188077000	–2.101226000	–1.443081000
C	–9.984713000	0.314493000	–1.131120000
H	–14.809480000	–0.001942000	0.324631000
C	–12.338673000	0.605232000	–0.649197000
F	2.330460000	1.379987000	–1.433239000
H	10.678273000	–2.455996000	0.077188000
C	–14.696936000	0.890610000	–0.297354000
H	6.379217000	–3.287324000	–0.980956000
C	9.695950000	–2.000115000	0.028661000
H	–7.247747000	–0.084615000	–1.029124000
H	8.607302000	1.716707000	–0.903208000
H	3.031043000	–4.710310000	–1.084058000
H	5.149540000	–4.467615000	–0.519808000
H	5.951641000	5.509384000	–0.762402000
H	2.657175000	3.740048000	–0.972705000
H	1.482438000	–3.921656000	–0.892302000
H	3.787279000	5.078158000	–0.688081000

C	–9.674017000	0.266184000	0.244905000
H	–4.994657000	–0.415549000	–1.406469000
C	–12.059436000	0.563126000	0.718852000
C	7.159945000	–0.820652000	–0.096476000
C	5.581867000	–3.498633000	–0.267203000
C	–7.186265000	–0.076168000	0.055945000
H	7.550733000	4.844074000	–0.564436000
H	–14.595939000	1.773839000	0.339771000
C	4.518697000	–2.440841000	–0.276757000
C	2.464306000	–4.044093000	–0.426030000
C	–4.773617000	–0.423194000	–0.343505000
H	0.629131000	–1.221172000	–1.461690000
C	5.805550000	–0.193123000	–0.163440000
C	4.665367000	–1.020871000	–0.216747000
C	3.144024000	–2.703650000	–0.357392000
H	–12.846281000	0.657025000	1.454776000
C	3.452965000	4.106288000	–0.324735000
B	3.077884000	1.056348000	–0.274380000

C	5.689580000	1.200719000	–0.179860000
C	–8.319478000	0.088897000	0.768820000
N	4.428532000	1.808150000	–0.271056000
C	–2.164713000	–0.796233000	–0.614191000
C	4.594267000	3.146385000	–0.267974000
C	–5.830782000	–0.254684000	0.580051000
N	3.386751000	–0.455942000	–0.257058000
C	6.548388000	4.846696000	–0.128250000
C	–10.741956000	0.396257000	1.145379000
C	2.480974000	–1.459499000	–0.338078000
C	6.669643000	2.247924000	–0.113964000
C	5.975019000	3.456346000	–0.177655000
C	8.158769000	2.122545000	0.007256000
C	1.024489000	–1.236353000	–0.451281000
C	–3.480132000	–0.594408000	0.114591000
H	8.607664000	3.098346000	0.193674000
C	–5.528558000	–0.266044000	1.960274000
C	–1.225828000	–0.899202000	0.605572000

C	8.945965000	–1.827801000	1.191981000
C	0.215302000	–1.097728000	0.610292000
H	–6.324256000	–0.138218000	2.684151000
H	–8.260263000	0.093322000	1.854088000
C	–3.207633000	–0.601301000	1.488716000
H	6.050377000	–3.592341000	0.716387000
H	0.645839000	–1.124608000	1.607100000
H	–10.541167000	0.365394000	2.211354000
C	–4.229735000	–0.437182000	2.424787000
N	–1.840614000	–0.786384000	1.750129000
C	7.681434000	–1.244533000	1.129953000
H	–2.593162000	0.535125000	–2.277075000
H	8.445156000	1.459046000	0.824938000
H	–4.014516000	–0.442990000	3.487251000
H	3.024976000	4.253248000	0.672524000
H	–0.863789000	0.307710000	–1.994982000
C	–1.830396000	0.423890000	–1.502403000
H	9.343124000	–2.148536000	2.148347000

F	2.325093000	1.429592000	0.863260000
H	1.785653000	–5.686273000	0.837809000
C	2.286043000	–4.719733000	0.945513000
H	7.032495000	6.447175000	1.272446000
C	6.614629000	5.436737000	1.292374000
H	7.098779000	–1.114571000	2.035010000
H	3.250717000	–4.891170000	1.430706000
H	5.620274000	5.491260000	1.743673000
H	1.682506000	–4.097518000	1.611730000
H	–1.805270000	1.343242000	–0.913109000
H	7.242838000	4.822501000	1.943205000

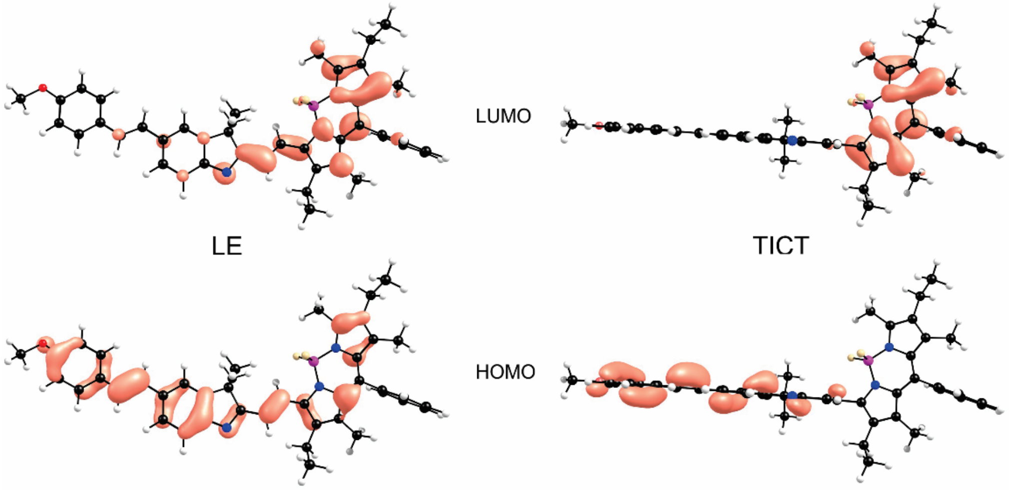

Figure 2.35. Molecular orbitals for **5** in the LE and TICT geometries computed with the with the B3LYP functional, the 6-311+G(d,p) basis set and the PCM-IEF for MeCN.

Table 2.4. Excitation energy (*E*), wavelength (λ) and oscillator strength (*f*) for the $S_0 \rightarrow S_1$ transition of 5 in the geometries associated with the LE and TICT states [*a*].

Geometry	*E* (eV)	τ (nm)	*f*
LE	1.95	634	1.31
TICT	2.40	517	0.05

[*a*] Computed with the B3LYP functional, the 6-311+G(d,p) basis set and the PCM-IEF for MeCN.

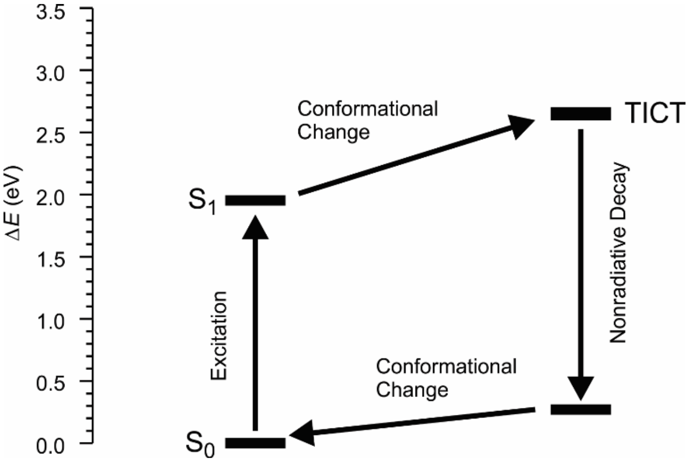

Figure 2.36. Relative energies of the ground and first-singlet excited state of **5** in the LE and TICT geometries computed with the B3LYP functional, the 6-311+G(d,p) basis set and the PCM-IEF for MeCN.

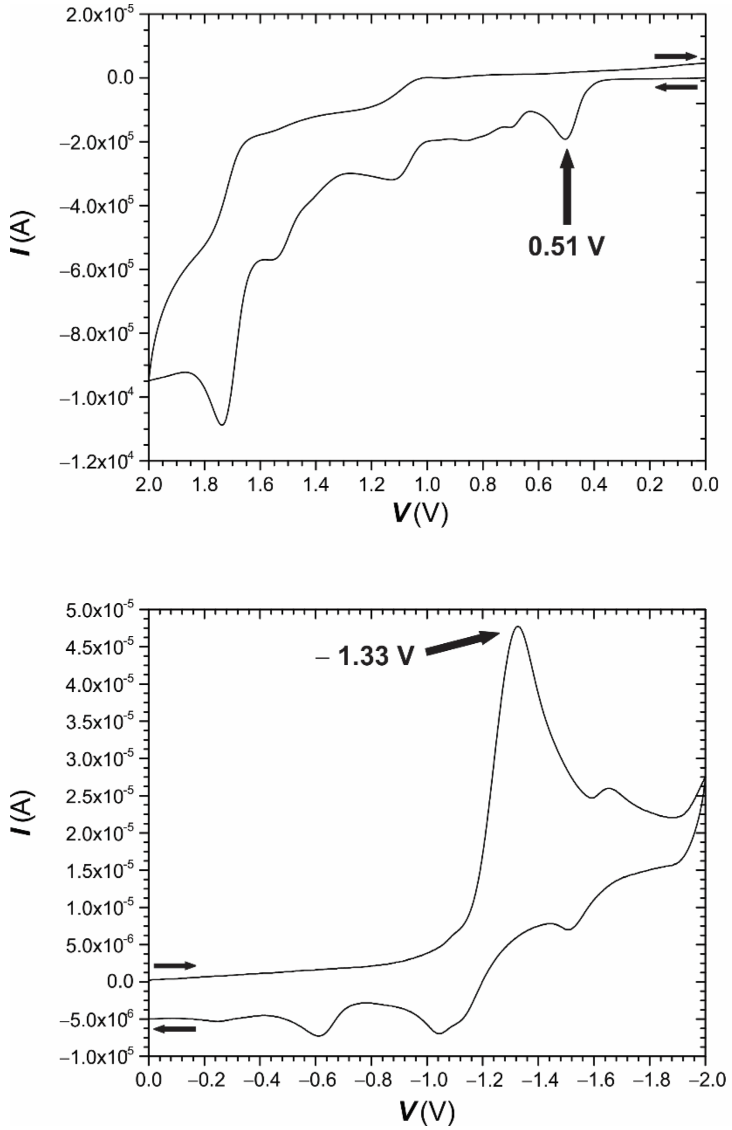

Figure 2.37. Cyclic voltammograms (100 mV s^{-1}, V *vs.* Ag/Ag^+) of a MeCN solution of **12** (1 mM) and Bu_4NPF_6 (0.1 M) at 20 °C.

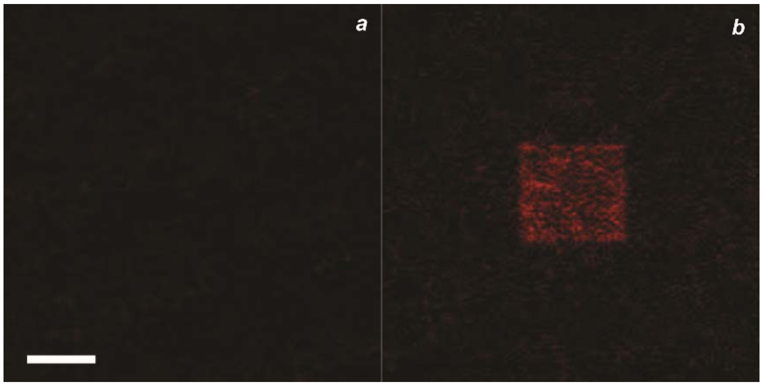

Figure 2.38. Fluorescence images (scale bar = 25 μm, λ_{Ex} = 633 nm, λ_{Em} = 660–800 nm) of a PMMA film, doped with **12** (0.15 % w/w), recorded before (*a*) and after (*b*) irradiation (λ_{Ac} = 405 nm, 0.11 mW, 60 s) of a square at the center of the imaging field.

Web Enhanced Object

Video 2.0. Sequence of overlaid fluorescence and transmittance images (456 × 456 μm^2, λ_{Ex} = 633 nm, λ_{Em} = 700–800 nm, frame time = 8 s) of two *Drosophila melanogaster* embryos, recorded over the curse of 9 min upon injection of a PBS solution of nanoparticles of **13**, containing **12**, into one of them after irradiation (λ_{Ac} = 405 nm, 22 μW, 60 s) of a selected area within the labeled embryo.

Chapter 3: 3-Heteroconjugated BODIPY Derivatives

3.1 Background and Design

As an extension of the scope of the work described in Chapter 2, we wanted to explore the effect of the carbon bearing two methyl groups at the 3 position of the indolenine moiety on the photophysical properties of the fluorophores. While locking the imine motive to the benzene ring preventing its rotation, this *sp*^{3} hybridized carbon bridge interrupts the π system channeling hampering a full aromatic communication. Replacing it with a heteroatom of *sp*^{2} nature, would establish full system aromaticity, expanding the π system as shown in Figure 3.0.

This modification should, in principle, lead to a bathochromically shifted photophysical profile for the represented derivatives.

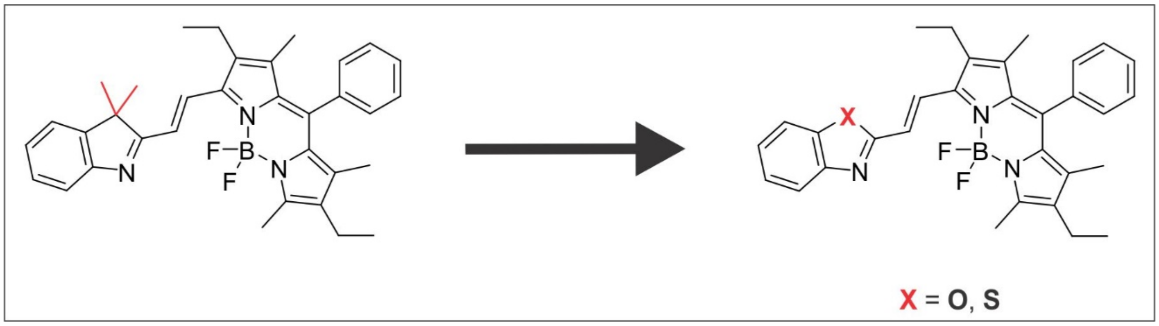

Figure 3.0. Heteroaromatic derivatives having an Oxygen or a Sulfur atom at the 3rd position of the auxochrome in place of the original Dimethylcarbon bridging system.

Specifically the 3rd position of the indolenine scaffold on the original compound (*left* in figure 3.0) was replaced with a heteroatom such as Oxygen or Sulfur. 3 analogs were synthesized and characterized (Figure 3.1).

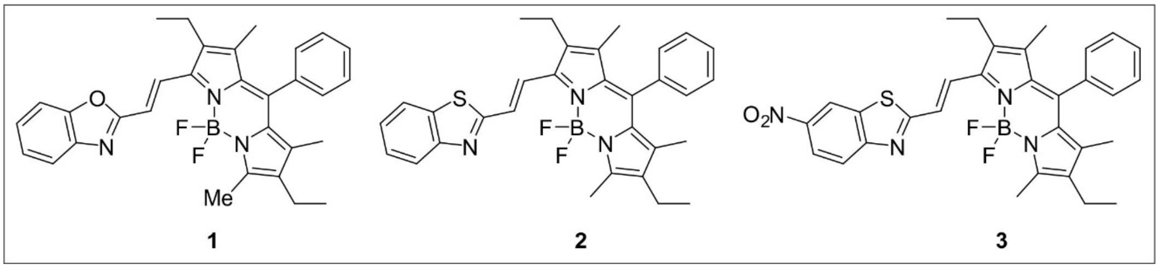

Figure 3.1 Synthesized Heteroaromatic BODIPY Derivatives

Compounds **1** and **2** have an extended bicyclic system in the form of benzoxazole or benzothiazole, respectively, while compound **3** is an analog of latter where the 6th position of the heteroaromatic auxochrome was functionalized with a nitro group to further extend the conjugation of the molecule.

3.2 Results and Discussion

3.2.1 Synthesis

The heteroaromatic analogs were synthesized exploiting phosphonium ylides chemistry.[94] 2-Methylbenzoxazole was halogenated using a Wohl-Ziegler bromination[95] affording the Bromomethyl derivative **4** that was converted to the phosphonate **5** with an Arbuzov rearrengement.[96] Finally, fluorophore **1**, in its E-configuration, was obtained in modest yield through a Horner-Wadsworth-Emmons olefination.[97] (Figure 3.2)

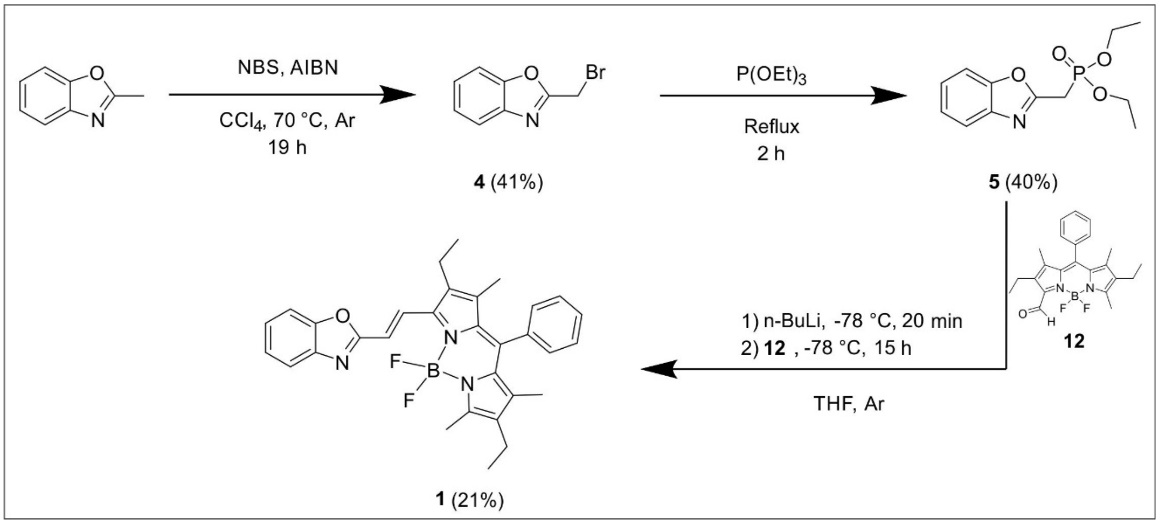

Figure 3.2. Synthetic scheme for compound **1**.

Due to the modest yield of the latter synthetic step for compound **1**, a different approach was used for the synthesis of the sulfur-containing derivative **2**. While the same bromination conditions were used to generate 2-Bromomethylbenzothiazole **6**, instead of the phosphonate **5**, we opted for the synthesis of the phosphonium salt **7**. The stable Phosphonium ylide **8** was obtained treating the salt **7** with a strong base and isolated as yellow crystals that were reacted with **12** in a Wittig coupling[98], with no need of basic conditions, to afford fluorophore **2** in its trans configuration[99] and in better yield compared to **1**. (Figure 3.3*)*. Additionally, the crystal structure of compound **2** was solved and the ORTEP representation showing 50% of Ellipsoid Probability is reported in Figure 3.4.

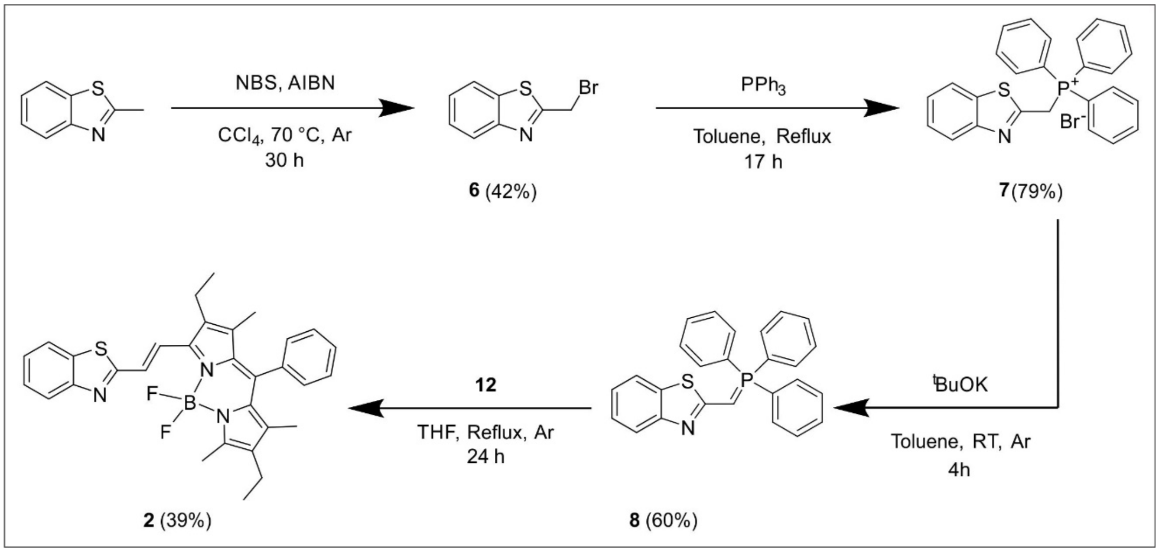

Figure 3.3. Synthetic scheme for compound **2**.

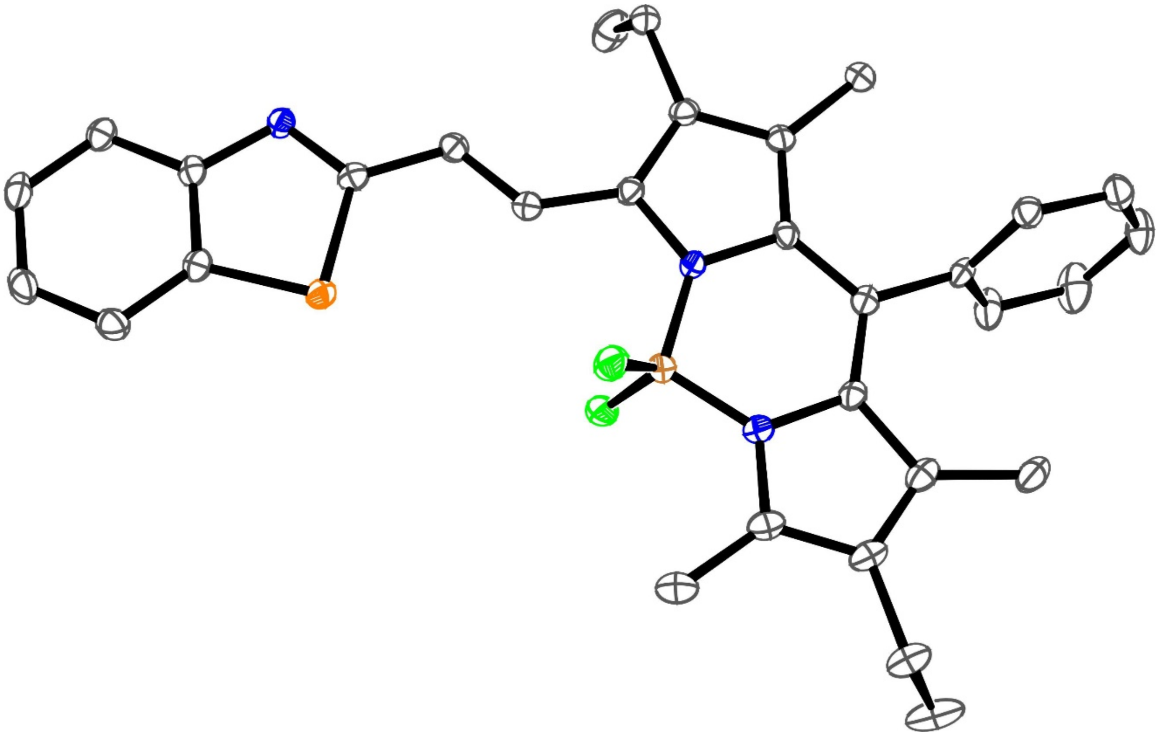

Figure 3.4. Crystal structure of compound **2** showing 50 % thermal ellipsoid probability.

The same synthetic strategy used to build compound **2** was applied for the synthesis of **3**. The only difference resides in the starting material used, being 6-Nitrobenzothiazole in place of Benzothiazole. All the reaction steps present lower yields compared to the ones performed for the unsubstituted derivative as show in Figure 3.5. The final compound **3** was obtained in 10 % yield.

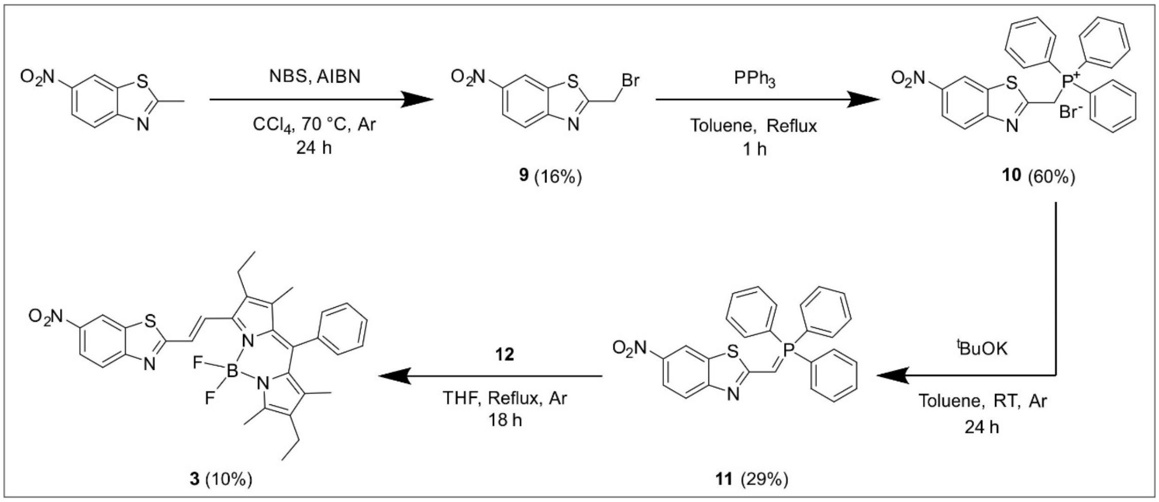

Figure 3.5. Synthetic scheme for compound **3**.

On the basis of what has been done for the indolenine BODIPY conjugates described in Chapter 2, here we attempted to synthesize photoactivatable versions of the heteroderivatives **1** and **2**. Unfortunately, all the attempts failed and a summary of the performed reactions is reported in Figure 3.6.

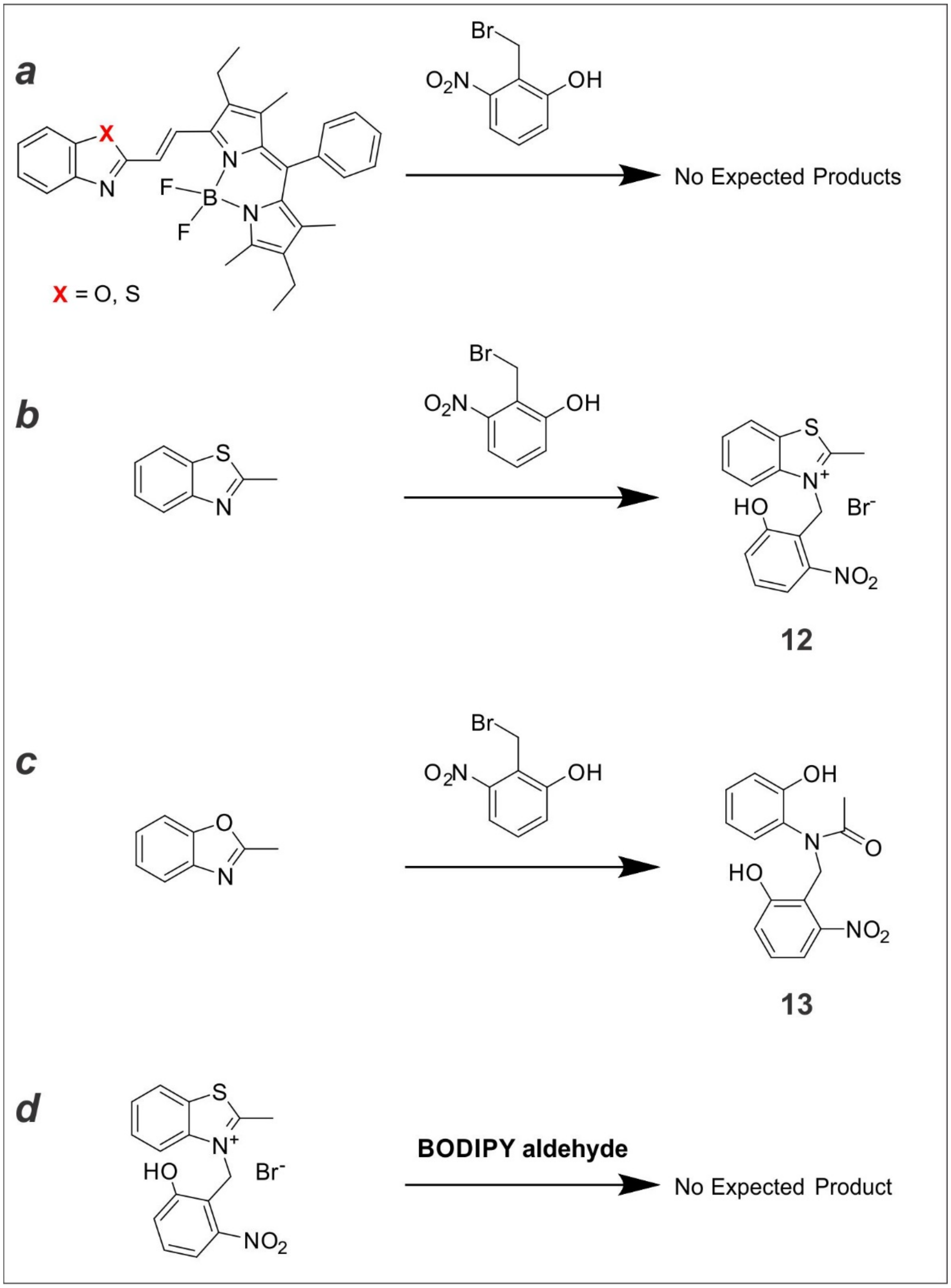

Figure 3.6. Summary of the performed attempts to generate photoactivatable analogs.

Derivatives **1** and **2** failed to provide the photoactivatable oxazines when reacted with 2-Bromomethyl-3-nitrophenol at RT or at reflux (***a*** in Figure 3.6). TLC of the reactions mixtures showed an unexpected complexity and the NMR analysis of the isolated spots didn't confirm the presence of the expected products. Surprisingly, when derivative **2** was treated with the caging group, the solution turned dark blue over time, suggesting that the analog may have been alkylated but the ring closure was somehow more difficult to happen. A possible explanation of the unusual reactivity of these analogs is that the benzoxazole or the benzothiazole are fully aromatic compared to the indolenine described previously and, while in the latter case the saturation of an imine bond is energetically acceptable, breaking the scaffold aromaticity in the former case is energetically unfavorable and the synthetic conditions tested won't allow the transition to happen. To confirm the hypothesis the same reaction was performed on the parent compounds 2-Methylbenzothiazole and 2-Methylbenzoxazole. In the first case (***b*** in Figure 3.6), as postulated before, the nitrogen of the heterocycle gets alkylated and the molecule can be easily isolated as a stable salt as confirmed by the crystal structure reported in Figure 3.7. Warming up of a solution of the isolated salt in different solvents (MeCN or EtOH), with or without base, didn't provide the expected oxazine.

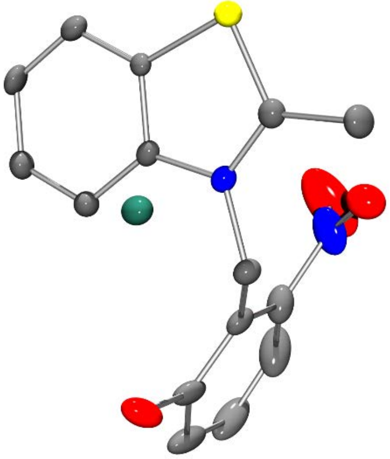

Figure 3.7. Crystal structure of **12** showing 50 % thermal ellipsoid probability.

In the second case (***c*** in Figure 3.6), a secondary amide derivative was obtained and characterized as showed in Figure 3.8. Probably, a molecule of water is responsible for the breaking up of the structure after alkylation of the nitrogen.

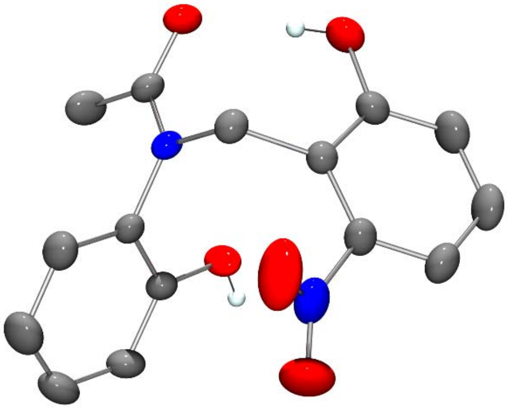

Figure 3.8. Crystal Structure of **13**.

Additionally, reaction of the isolated benzothiazolium salt **12** (***d*** in Figure 3.6) with BODIPY aldehyde (Compoud **12** in Chapter 2) in various solvents didn't provide the expected photoactivatable fluorophore.

3.2.2 Photophysical Properties

A summary of the photophysical properties for the heteroaromatic analogs described in this chapter is reported in Table 3.0. On the basis of the data obtained, a bathochromic shift in the absorption maxima was observed for all the indolenine derivatives described in Chapter 2 but not for the heteroaromatic **1**, **2** and **3** which showed an unexpected hypsochromic behavior. Surprisingly, **1** and **2** possess very high quantum yield compared to the indolenine analogs from the previous chapter that, instead, showed an increase of the non-radiative decay (Table 3.0). We postulated that, while the extended conjugation improved their absorption/emission profile, the increased degrees of conformational freedom limit the radiative decay from the excited state (Table 2.0). Possibly, the heteroatom at the 3rd position of the heterocycle occupies a key position for a full radiative decay from the photogenerated excited state of the molecule. Extension of the conjugation in the case of **3** leads to a bathochromic shift for the absorption maximum but induced a 50% decrease of the quantum yield.

Table 3.0. Wavelengths at the absorption (λ_{Ab}) and emission (λ_{Em}) maxima, Stoke's shift ($\Delta\lambda$), absorbance (A_{633}) at 633 nm reported relative to that at λAb and fluorescence quantum yield (ΦF) of **1–3** in aerated MeCN at 20 °C

	λ_{ab} [nm]	λ_{em} [nm]	Δλ (nm)	A_{633} (%)	Φ_f
1	578	593	15	2.3	0.83
2	584	597	13	1	0.85
3	592	613	21	4.7	0.44

3.3 Conclusion

A series of Heteroaromatic BODIPY conjugates was synthesized and characterized. While it was postulated that establishing a full system aromaticity would have been beneficial for the Absorption properties of the fluorophores, it has been found that the 3rd position of the auxochrome is affecting the Absorption maximum in a negative way while it raises incredibly the quantum yield. Additionally, extending the conjugation of the molecule, such in the case of **3**, leads to a red shift in the absorption but affect severely the quantum yield. Moreover, it seems that the designed analogs are incapable of being transformed into photoactivatable derivatives. Further experiments are ongoing to extend the conjugation of the aforementioned compounds and find new synthetic ways to install the oxazine photoswitch on the derivatives.

3.4 Experimental Section

Materials and Methods

Chemicals were purchased from commercial sources and used as received. CH_2Cl_2 and CH_3CN were distilled over CaH_2. THF was distilled over Na and benzophenone. H_2O (18.2 MΩ cm) was purified with a Barnstead International NANOpure Diamond analytical system. Electrospray ionization mass spectrometry (ESIMS) was performed with a Bruker micrOTO-Q II spectrometer.

NMR spectra were recorded with Bruker 300, 400 and 500 spectrometers. Absorption spectra were recorded with a Varian Cary 100 Bio spectrometer in quartz cells with a path length of 0.1 or 1.0 cm as specified. Emission spectra were recorded with a Varian Cary Eclipse spectrometer in aerated solutions. Fluorescence quantum yields were determined against a solution of **3** in MeCN (From Chapter 2) following a literature protocol.

Synthesis

1. An oven dried 25 mL round bottom flask equipped with a stirring bar was loaded with **5** (100 mg, 0.37 mmol) and sealed with a rubber septum. 5 mL of dry THF were introduced through a needle keeping the flask under Argon atmosphere. The solution was cooled to –78 °C with a liq. N_2/EtOAc bath and n-Buli (0.16 mL of 2.5 M in Hexane, 0.41 mmol) was added dropwise. After 15 min of stirring, Bodipy aldehyde (0.15 g, 0.37 mmol) dissolved in 3 mL of dry THF was added dropwise through an addition funnel and the mixture was stirred to RT for 15 h. The solvent was evaporated at reduced pressure and the residue was dissolved in EtOAc (15 mL), washed with NaCl aq. sat. (3 x 20 mL), dried over Na_2SO_4 and evaporated at reduced pressure. The crude residue was purified by column chromatography twice [SiO_2, Hexane/Dichloromethane/Ethyl Acetate (80:15:5, v/v) followed by Chloroform/Hexane (50:10, v/v)] to afford **1** as a dark gold solid (40 mg, 21%). HRESIMS: *m/z* calcd for $C_{12}H_{16}NO_4P$: 509.2450; found: 510.2529 $[M+H]^+$; ^{1}H-NMR (300 MHz, $CDCl_3$): δ= 8.29 (d, J = 16.7 Hz, 1H), 7.78 – 7.66 (m, 1H), 7.60 (dd, J = 6.8, 2.3 Hz, 1H), 7.57 – 7.46 (m, 3H), 7.44 – 7.29 (m, 4H), 7.17 (d, J = 16.7 Hz, 1H), 2.77 – 2.54 (m, 5H), 2.35 (q, J = 7.5 Hz, 2H), 1.33 (m, 6H), 1.17 (t, J = 7.5 Hz, 3H), 1.02 (t, J = 7.5 Hz, 3H).

2. Bodipy aldehyde (50 mg, 0.13 mmol) and **8** (100 mg, 0.24 mmol) were placed in a 25 mL round bottom flask equipped with stirring bar, under Argon flow, and 5 mL of dry THF were added. The mixture was stirred at RT for 5 mins and refluxed for 19 h. 0.5 additional equiv. of **8** were added and the mixture was kept at reflux for 4 h. The reaction mixture was cooled to RT and the solvent evaporated at reduced pressure. The residue was purified by column chromatography chromatography [SiO_2, Dichloromethane 100%] to afford **2** as a gold solid (27 mg, 39%). HRESIMS: *m/z* calcd for $C_{31}H_{30}BF_2N_3S$: 525.2222; found: 526.2302 $[M+H]^+$; ^{1}H-NMR (400 MHz, $CDCl_3$): δ= 8.07 (d, *J* = 16.8 Hz, 1H), 8.01 (d, *J* = 8.1 Hz, 1H), 7.87 (d, *J* = 7.9 Hz, 1H), 7.60 – 7.43 (m, 5H), 7.43 – 7.29 (m, 3H), 2.74 – 2.56 (m, 5H), 2.35 (q, *J* = 7.7 Hz, 2H), 1.39 – 1.29 (m, 6H), 1.17 (t, *J* = 7.6 Hz, 3H), 1.02 (t, *J* = 7.6 Hz, 3H).

3. Red crystals of **11** (90 mg, 0.19 mmol) and Bodipy aldehyde (50 mg, 0.13 mmol) were dissolved in 5 mL of dry THF and the reaction mixture was refluxed overnight. Upon cooling, the solvent was evaporated at reduced pressure and the reside was purified with column chromatography [SiO_2, Hexane/Ethyl Acetate/Dichloromethane (80:10:10, v/v)] to afford **3** (7.5 mg, 10%). HRESIMS: *m/z* calcd for $C_{31}H_{29}BF_2N_4O_2S$: 570.2072; found: 571.2140 $[M+H]^+$; ^{1}H-NMR (500 MHz, $CDCl_3$) δ= 8.79 (d, *J* = 2.4 Hz, 1H), 8.36 (dd, *J* = 9.0, 2.3 Hz, 1H), 8.18 (d, *J* = 16.7 Hz, 1H), 8.07 (d, *J* = 9.0 Hz, 1H), 7.73 – 7.65 (m, 1H), 7.56 – 7.52 (m, 3H), 7.36 – 7.30 (m, 2H), 2.72 – 2.60 (m, 5H), 2.37 (q, *J* = 15.0, 7.4 Hz, 2H), 1.35 (s, 3H), 1.34 (s, 3H), 1.18 (t, *J* = 7.5 Hz, 3H), 1.04 (t, *J* = 7.5 Hz, 3H).

4. 2-Methylbenzoxazole (1 g, 7.51 mmol) was placed in a 50 mL round bottom flask equipped with a stirring bar and 10 mL of CCl_4 were added. To the stirring mixture, under Argon flow, were respectively added NBS (1.34 g, 7.51 mmol) and AIBN (62.4 mg, 0.38 mmol). The reaction mixture was slowly warmed to 70 °C and stirred at the same temperature for 19 h. The resulting suspension was cooled to RT, filtered over a Büchner funnel and the filtrate was evaporated at reduced pressure. The crude product was purified by column chromatography [SiO_2, Hexane/Dichloromethane/Ethyl Acetate (30:10:1, v/v)] to afford **4** (0.65 g, 41%). LRESIMS: *m/z* calcd for C_8H_6BrNO: 211.0; found: 234.0

[M+Na]$^+$; ^{1}H-NMR (300 MHz, $CDCl_3$): δ= 7.77-7.74 (m, 1H), 7.60-7.54 (m, 1H), 7.45-7.35 (m, 2H), 4.62 (s, 2H).

5. **4** (0.63 g, 2.99 mmol) was placed in a 10 mL round bottom flask equipped with a stirring bar and dissolved in 1.02 mL of Triethylphosphite (5.98 mmol). The mixture was refluxed for 2 h, cooled to RT, added with 5 mL of EtOAc, washed with 1M HCl (3 x 10 mL), dried over Na_2SO_4 and evaporated at reduced pressure. The crude residue was purified by column chromatography [SiO_2, Dichloromethane/Ethyl Acetate (50:50, v/v)] to afford **5** (0.29 g, 36%). HRESIMS: *m/z* calcd for $C_{12}H_{16}NO_4P$: 269.0817; found: 270.0899 [M+H]$^+$; ^{1}H-NMR (300 MHz, $CDCl_3$): δ= 7.73-7.69 (m, 1H), 7.58-7.52 (m, 1H), 7.39-7.32 (m, 2H), 4.27-4.16 (m, 4H), 3.63 (s, 1H), 3.56(s, 1H), 1.35 (m, 6H).

6. 2-Methylbenzothiazole (2 g, 13.4 mmol) was placed in a 100 mL round bottom flask equipped with a stirring bar and 20 mL of CCl_4 were added. To the stirring mixture, under Argon flow, were respectively added NBS (2.39 g, 13.4 mmol) and AIBN (110 mg, 0.67 mmol). The reaction mixture was slowly warmed to 70 °C and stirred at the same temperature for 6 h. The resulting suspension was cooled to RT, filtered over a Büchner funnel and the filtrate was evaporated at reduced pressure. The crude product was purified by column chromatography [SiO_2, Hexane/Dichloromethane/Ethyl Acetate (30:10:1, v/v)] to afford **6** as yellow crystals (1.27 g, 42%). ^{1}H-NMR (400 MHz, $CDCl_3$): δ= 8.04 (d, J = 8 Hz, 1H), 7.89 (d, J = 8 Hz, 1H), 7.52 (t, J = 8 Hz, 1H), 7.44 (t, J = 8 Hz, 1H) 4.83 (s, 2H).

7. **6** (1.26 g, 5.50 mmol) and PPh_3 (1.53 g, 5.50 mmol) were placed in a 50 mL round bottom flask equipped with stirring bar and dissolved with 15 mL of dry Toluene. The mixture was refluxed for 17 h after which, it was cooled to RT and filtered over a Büchner funnel. The recovered solid was dried under vacuum to afford **7** as a beige powder (2.13 g, 79%).[100]

8. **7** (500 mg, 1.02 mmol) was placed in a 50 mL round bottom flask equipped with stirring bar and added with 10 mL of dry Toluene under Argon flow. ^{t}BuOK (137 mg, 1.22 mmol) was quickly added to the mixture that was stirred at RT for 3 h under Argon atmosphere. The yellow solution was filtered over celite, the filtrated solvent was evaporated at reduced pressure to afford a residue that was dissolved in the minimum amount of DCM (0.5 mL) and n-Hexane was added (20 mL). The flask was left in the freezer overnight to afford **8** as yellow crystals (400 mg, 59%).[101]

9, 10 and **11** were synthesized following the synthetic procedures used for **6**, **7** and **8**.

9. ^{1}H-NMR (300 MHz, $CDCl_3$) δ= 8.85 (d, J = 2.2 Hz, 1H), 8.49 – 8.32 (m, 1H), 8.14 (dd, J = 9.1, 1.2 Hz, 1H), 4.86 (s, 2H).

Crystallographic Analysis for 2. Single crystals of **2**, suitable for diffraction analysis, grew from an DCM solution of the compound after the diffusion of Pentane vapors at ambient temperature. The data crystal was mounted onto the end of a thin glass fiber using Paratone-N for data collection at 100 K under N_2. X-ray intensity data were measured by using a Bruker SMART APEX2 CCD-based diffractometer using Mo Kα radiation (λ = 0.71073 Å).[84] The raw data frames were integrated with the SAINT+ program by using a narrow-frame integration algorithm.[84] Corrections for Lorentz and polarization effects were also applied with SAINT+. An empirical absorption correction based on the multiple measurement of equivalent reflections was applied using the program SADABS. All structures were solved by a combination of direct methods and difference Fourier syntheses, and refined by full-matrix least-squares on F^2, by using the SHELXTL software package.[85-86] All non-hydrogen atoms were refined with anisotropic displacement parameters. Hydrogen atoms were placed in geometrically-idealized positions and included, as standard riding atoms, during the least squares refinements. Crystal data, data collection parameters and results of the analyses are listed in Table 3.1. Compound **2** crystallized in the monoclinic crystal system. The systematic absences in the intensity data identified the unique space group $P2_1/n$.

Crystallographic Analysis for 12. Single crystals of **12**, suitable for diffraction analysis, grew from a methanol solution of the compound after the diffusion of Et_2O vapors at ambient temperature. The data crystal was mounted onto the end of a thin glass fiber using Paratone-N for data collection at 100 K under N_2. X-ray intensity data were measured by using a Bruker SMART APEX2 CCD-based diffractometer using Mo Kα radiation (λ = 0.71073 Å).[84] The raw data frames were integrated with the SAINT+ program by using a narrow-frame integration algorithm.[84] Corrections for Lorentz and polarization effects were also applied with SAINT+. An empirical absorption correction based on the multiple measurement of equivalent reflections was applied using the program SADABS. All structures were solved by a combination of direct methods and difference Fourier syntheses, and refined by full-matrix least-squares on F^2, by using the SHELXTL software package.[85-86] All non-hydrogen atoms were refined with anisotropic displacement parameters. Hydrogen atoms were placed in geometrically-idealized positions and included, as standard riding atoms, during the least squares refinements. Crystal data, data collection parameters and results of the analyses are listed in Table 3.2. Compound **12**

crystallized in the monoclinic crystal system. The systematic absences in the intensity data identified the unique space group $P2_1/c$.

Table 3.1. Crystallographic Data for Compound **2**.

	2
Empirical formula	$C_{31}H_{30}BF_2N_3S$
Formula weight	525.45
Crystal system	Monoclinic
Lattice parameters	
a (Å)	10.8426(5)
b (Å)	21.9098(11)
c (Å)	11.8473(6)
β (deg)	106.849(1)
V (Å^3)	2693.6(2)
Space group	$P2_1/n$ (#14)
Z value	4
ρ_{calc} (g / cm^3)	1.296
μ (Mo Kα) (mm^{-1})	0.160
Temperature (K)	100
$2\Theta_{max}$ (°)	50.00
No. Obs. (I > 2σ(I))	3899
No. Parameters	348

Goodness of fit	1.024
Max. shift in cycle	0.003
Residuals*:R1; wR2	0.0402; 0.0872
Absorption Correction, Max/min	Multi-scan 0.7457/ 0.6500
Largest peak in Final Diff. Map (e^- / Å^3)	0.344

*$R1 = \Sigma_{hkl}(||F_{obs}| - |F_{calc}||)/\Sigma_{hkl}|F_{obs}|$; $wR2 = [\Sigma_{hkl}w(|F_{obs}| - |F_{calc}|)^2/\Sigma_{hkl}wF_{obs}^2]^{1/2}$, $w = 1/\sigma^2(F_{obs})$; $GOF = [\Sigma_{hkl}w(|F_{obs}| - |F_{calc}|)^2/(n_{data} - n_{vari})]^{1/2}$.

Table 3.2 Crystallographic Data for Compound **12**.	**12**
Empirical formula	$C_{15}H_{13}N_2O_3S{\bullet}Br$
Formula weight	381.24
Crystal system	Monoclinic
Lattice parameters	
a (Å)	6.9242(3)
b (Å)	12.1677(5)
c (Å)	18.0990(8)
β (deg)	90.575(1)
V (Å^3)	1524.79(11)
Space group	*P*2$_1$/*c* (#14)
Z value	4
ρ_{calc} (g / cm^3)	1.661
μ (Mo Kα) (mm^{-1})	2.846
Temperature (K)	100
$2\Theta_{max}$ (°)	56.0
No. Obs. (I > 2σ(I))	3477

No. Parameters	201
Goodness of fit	1.253
Max. shift in cycle	0.000
Residuals*:R1; wR2	0.0454; 0.1145
Absorption Correction, Max/min	Multi-scan 0.7466/ 0.4627
Largest peak in Final Diff. Map (e^- / Å^3)	1.437

*R1 = $\Sigma_{hkl}(||F_{obs}| - |F_{calc}||)/\Sigma_{hkl}|F_{obs}|$; wR2 = $[\Sigma_{hkl}w(|F_{obs}| - |F_{calc}|)^2/\Sigma_{hkl}wF_{obs}^2]^{1/2}$, w = $1/\sigma^2(F_{obs})$; GOF = $[\Sigma_{hkl}w(|F_{obs}| - |F_{calc}|)^2/(n_{data} - n_{vari})]^{1/2}$.

Absorption and Emission Spectra

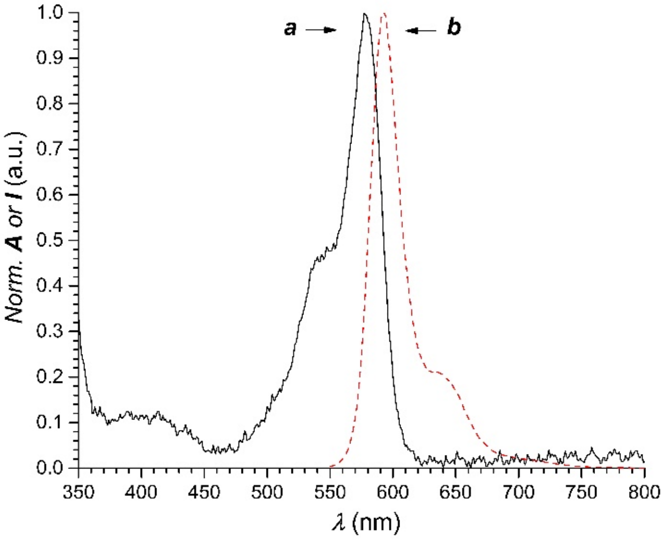

Figure 3.9. Normalized absorption (***a***) and emission (***b***, λ_{Ex} = 540 nm) spectra of **1** in MeCN at 20 °C.

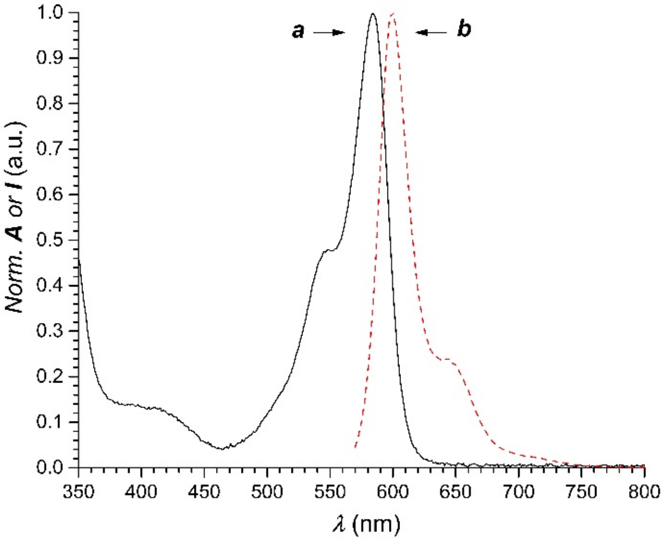

Figure 3.10. Normalized absorption (***a***) and emission (***b***, λ_{Ex} = 560 nm) spectra of **2** in MeCN at 20 °C

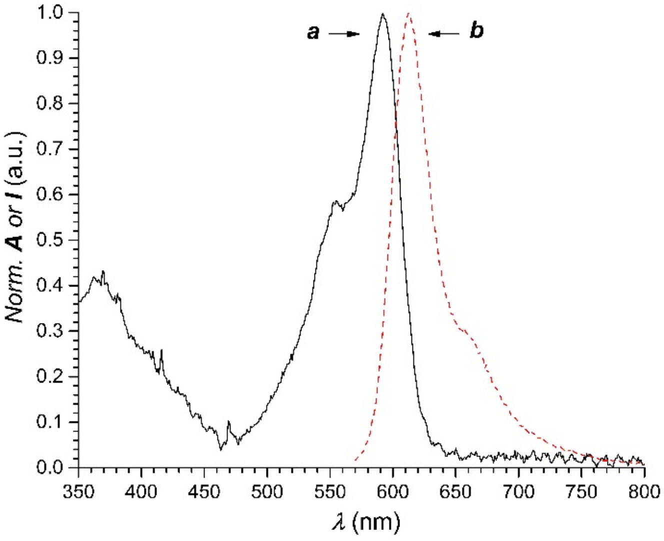

Figure 3.11. Normalized absorption (***a***) and emission (***b***, λ_{Ex} = 560 nm) spectra of **3** in MeCN at 20 °C

Chapter 4: The First Photoactivatable Diazepam: A Neuropharmacological Tool

4.1 Background

While many brain functions are well known,[102] many aspects of the most common central nervous system(CNS)-related diseases such as Schizophrenia, Depression, Epilepsy, Parkinson's and Alzheimer's Diseases are still poorly understood.[103] Understanding the exact physiology of neurons, in particular neuronal subpopulations involved in pathologic processes, is fundamental to develop the proper treatment while limiting unwanted side effects.[104] Animals and translational models are essentials to the understanding of the mechanisms underlying CNS-related diseases[105] but the *selective delivery* of neuroactive molecules to brain-specific areas is not easily achievable without the use of special techniques.[106-107] In fact, the oral or the intravenous administration routes, granted the fact that the molecule crosses the blood brain barrier, would lead to a distribution of the same molecule in the entire CNS. Delivery of the drug to neurons' subpopulations can be achieved using invasive surgery techniques, and while relatively effective, it requires adequate surgical expertise.

It wasn't until the beginning of 2000 that new approaches became available to Neuroscientists, namely Optogenetics and Chemogenetics. Both relying on genetic modification, the first technique offers the opportunity to generate light-responsive ionic channels in specific neuronal populations[108] while the second one is most exploited using the DREADDs approach (Designer Receptors Exclusively Activated by Designer Drugs)[109-111] where genetically cell-generated receptors are responsive to just synthetic ligands but not to the endogenous ligands. Even if these techniques are powerful tools in the hands of neuroscientists, the genetic manipulation doesn't simplify the scenario. In search of valid alternatives, the field of Optopharmacology is now growing fast: the remote light-induced activation of a neuroactive molecule at a specific time is a very promising technique to achieve a selective delivery. The field of Photopharmacology, pioonered by Erlanger and co-workers around 1969,[112] has shown incredible potential in the last decade.[113-115] In fact, a photocaged, and *inactive molecule*, can be irradiated at a specific time and wavelength to release the active molecule in the region of interest, either a particular cell subregion or a neuronal subpopulation. This approach could shine light on the poorly understood processes that happen in defined cell types intermingled with populations having different or opposite functions in the brain as depicted in Figure 4.0.

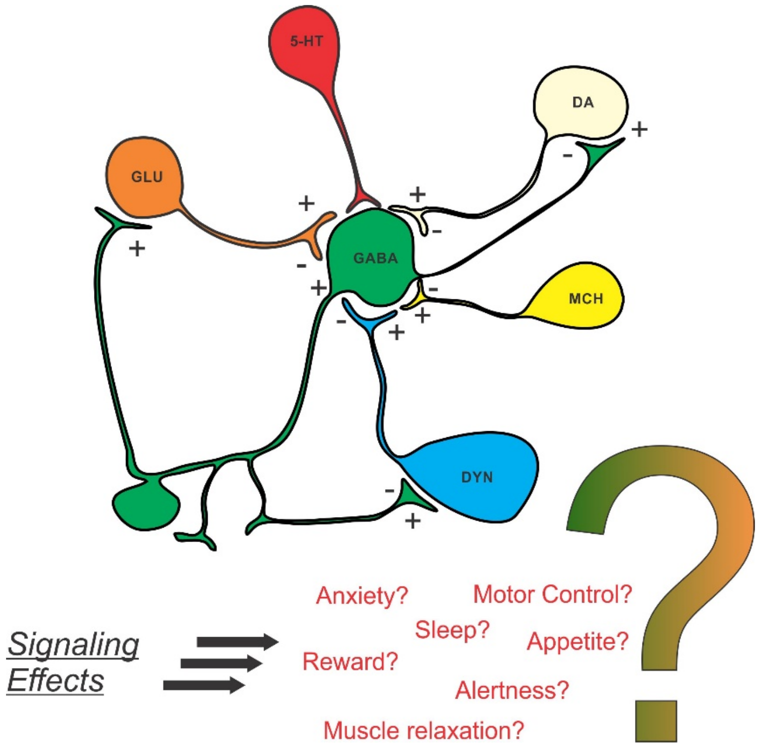

Figure 4.0. Figure showing a complex neural circuit where different neuronal pathways are intermingled to balance specific effects. (GLU: Glutamate, 5-HT: Serotonin, DA: Dopamine, MCH: Melanin-concentrating hormone, DYN: Dynorphine, GABA: γ-aminobutyric acid)

Thus, the development of photoactivatable CNS signaling molecules could be key to the understanding of numerous and important brain functionalities not yet understood. Specifically, manipulating those neuronal transmissions having a large impact on the whole CNS, such as the glutamatergic or gabaergic way, is of fundamental importance.

Among the many signaling molecules in the CNS,[116-117] GABA (γ-aminobutyric acid) is one of the most important inhibitory neurotransmitter acting on GABA receptors in vertebrate brains.[118-119] About 25% of the synapses in the CNS (cortex, hippocampus, thalamus and cerebellum) are GABAergic thus affecting their activity has a huge impact on the whole system physiology. GABA acts on three different families of receptors: GABA$_{\mathbf{a}}$, GABA$_{\mathbf{a\text{-}\rho}}$ and GABA$_{\mathbf{b}}$. While the first two are ligand-gated ionic channels, the last one belongs to the family of G-Protein Coupled Receptors (GPCRs). Clinically, GABA$_{\mathbf{a}}$ has been the most studied and this is well shown by the large number of FDA approved drugs acting on these synapses such as Benzodiazepines.[103-104] Some of these molecules are still nowadays therapeutic milestones for the treatment of insomnia, anxiety and epilepsy. GABA$_{\mathbf{a\text{-}\rho}}$, sometimes mistakenly referred as GABA$_{\mathbf{c}}$, is the least known and, while its agonists and antagonists have been defined, its complete role hasn't been fully determined and no drug is available for clinical use. GABA$_{\mathbf{b}}$**,** a heterodimeric GPRC that activates K^{+} channels and blocks Ca^{2+} channels, is the target of Baclofen, a well-known drug to treat muscle spasticity. In this extent only the GABA$_{a}$ receptor will be briefly described:

GABA$_{\mathbf{a}}$ receptors are heteropentameric channels permeable to Chloride ions made from 19 known subunits (α1–6, β1–3, γ1–3, δ, ε, θ, π and ρ1–3). Most of the GABA$_{\mathbf{a}}$ receptors present a 2α:2β:1γ subunit association stoichiometry with two GABA binding sites generated at the interface between the α and β subunits. 60% of all GABA$_{\mathbf{a}}$ receptors have the subunit subtype α1β2γ2, 15–20% have the α2β3γ2 combination, 10–15% have the α3βnγ2 combination, 5% have the α4βnγ or α4βnδ combination and less than 5% have the α5β2γ2 combination or the α6β2/3γ2 combination. The binding of two GABA molecules with the receptor dictates a conformational change that induces the channel opening with the subsequent inward flux of chloride anions that leads to hyperpolarization of postsynaptic neurons and, ultimately, inhibition of impulse transmission. (Figure 4.1)

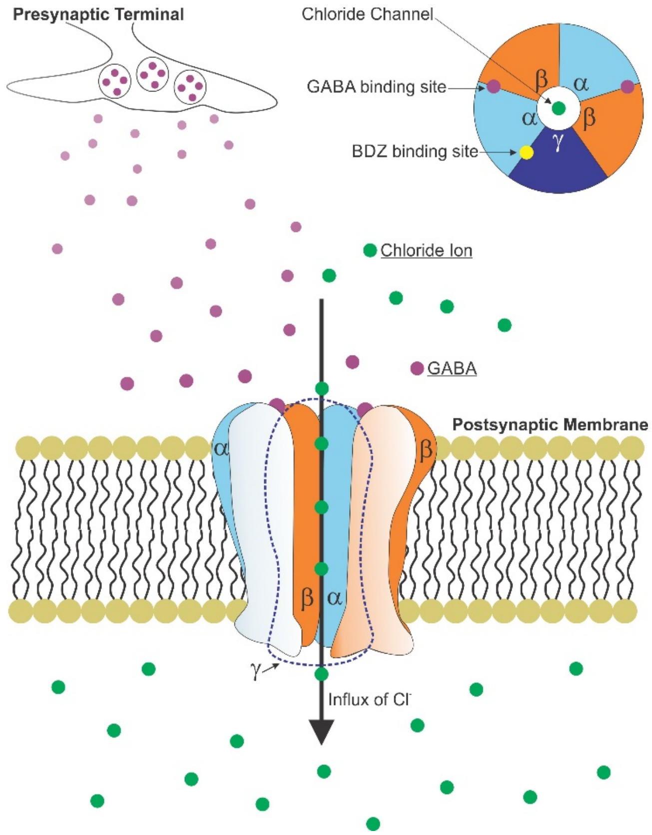

Figure 4.1. GABA molecules diffusing from the pre- to the postsynaptic terminal where they bind to the receptor inducing the channel opening that allows the chloride ions to permeate through the membrane generating a hyperpolarization.

The binding site for benzodiazepines is in between an α (α1, α2, α3 or α5) and a γ subunit (generally γ2). GABA$_a$ receptors containing α4 or α6 subunits are not sensitive to benzodiazepines. Ligands at the benzodiazepine binding site of the receptor are allosteric modulators: they modify the efficacy and/or affinity of the endogenous agonist (i.e. GABA) and thus regulate their activity. The direction of the modulation can be positive, negative or neutral. Benzodiazepines are the most studied and used modulators but the receptor is also a major target for the hypnotic z-drugs (zolpidem, zopiclone and zaleplon) for barbiturates and for many general anaesthetics.[119]

While positive allosteric modulators increase the extent of membrane hyperpolarization, their mechanism of action can be different. Specifically, BDZs are positive allosteric modulators of the receptor and they have no effect in the absence of GABA that is indeed required for the action. Upon binding to the receptor, BDZs increase the opening frequency of the channel compared to GABA alone[120] (Figure 4.2) leading to a potentiated hyperpolarization.

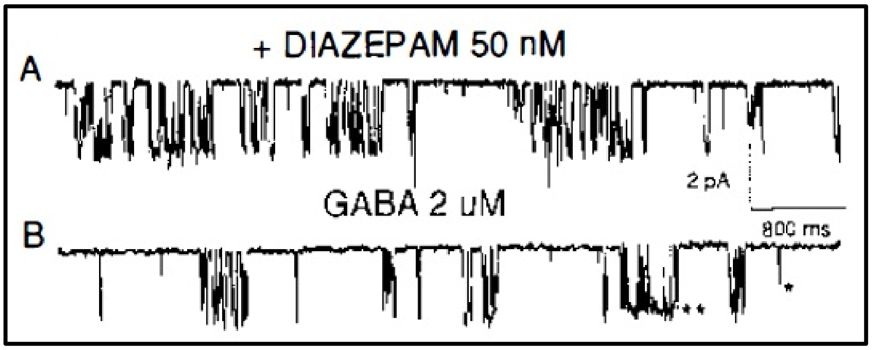

Figure 4.2. The application of GABA + Diazepam (A) increases the frequency opening of GABA$_a$ receptors compared to the application of GABA alone (B) to patches obtained from mouse spinal cord neurons in cell culture (Adapted from Annu. Rev. Neurosci. 1994, © Annual Reviews Inc.)

Clinically, the pharmacological effect exerted by BDZ leads to hypnosis or sedation, anxiolysis and muscle relaxation and they are used to treat insomnia, anxiety and epilepsy respectively but the description of such would deviate from the main purpose of this chapter and the reader can fine the very fine details in the many exquisite textbooks covering the topic.[121]

4.2 Results and Discussion

4.2.1 Design and Synthesis

While various groups synthesized different versions of photocaged GABA,[122-124] none of them was used to study the physiology of specific neuronal subpopulations. Photocaging of Benzodiazepines would provide a completely new photoactivatable molecule (prodrug) with the following advantages over photocaged GABA (upon photoactivation):

1. Binding selectivity towards the different α-containing GABA$_\mathbf{a}$ receptors. The selectivity of the different members of the class towards specific α subunits can be used to target neuronal subpopulations known to be involved in specific pathologies. In fact, point mutations in mice showed that the pharmacological effects are closely related to the α subunit subtypes. Specifically, the sedative, anterograde, amnestic and partly the anticonvulsant actions of diazepam are mediated by α1-containing GABA$_\mathbf{a}$ receptors; the anxiolytic-like and, to a large extent, the myorelaxant actions are mediated by α2-containing GABA$_\mathbf{a}$ receptors while the myorelaxant action is mediated in part by α3- and α5-containing GABA$_\mathbf{a}$ receptors.[119]

2. Suppressed interaction with $GABA_b$ and $GABA_{a-\rho}$ receptors. This would shut down collateral pathways arising from the activation of the other GABA receptors and allow one to focus on just one GABAergic pathway.
3. Extremely potent compared to GABA. Dramatic increase in ionic current compared to the use of GABA alone that translates into a very noticeable effect (Figure 4.2).

Valium® is the commercial name of Diazepam. FDA approved in 1963,[125] its effectiveness for the treatment of Insomnia, Anxiety and Epilepsy made it a pharmacological milestone over the years. Due to its well known pharmacological properties and the extensive clinical history in animals and humans, Diazepam was chosen as model compound for this work. The choice of Diazepam offers two main advantages: i) The drug can be easily synthesized in 3 total steps from readily available starting materials ii) The presence of an imine motive between the 4th and 5th positions makes it appealing for a further functionalization into prodrug derivatives. Here, a photoresponsive benzoxazine derivative of Diazepam was synthesized. Specifically, an o-Nitrobenzyl group, well exploited as photoremovable group,[66] was installed onto the molecule in the masked form of benzoxazine (Figure 4.3).

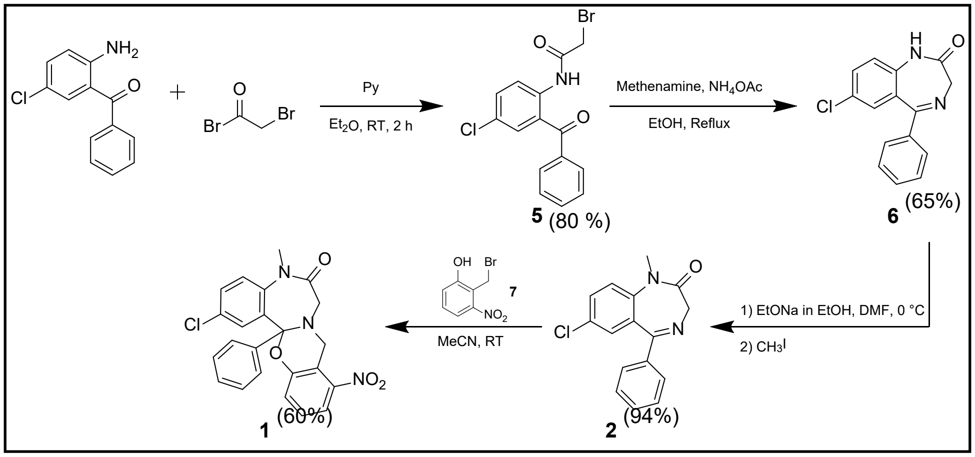

Figure 4.3. Synthetic route to **1**.

The synthesis of **1** is achievable in 3 simple steps: commercially available 2-Amino-5-chlorobenzophenone was reacted with Bromo acetyl bromide in the presence of Pyridine to afford **5** in 80% yield. The aromatic bromomethyl derivative was then reacted with methenamine to generate a quaternary ammonium salt intermediate that, upon acidic reflux, underwent the Delépine reaction to an aminomethyl intermediate which cyclizes to Nordazepam **6** in 65% yield. Diazepam (**2**) was obtained in 94% yield upon methylation of the lactam amino functionality; subsequent reflux with 2-Bromomethyl-3-nitrophenol afforded the final compound **1** in good yield.

4.2.2 Photophysical Properties

Compound **1** was further characterized by X-Ray diffraction and the crystal structure obtained reported in Figure 4.4 is showing 40% of Thermal Ellipsoid Probability. Due to the very well known properties of o-Nitrobenzyl caging groups, as explained in chapter 1, the irradiation of **1** with UV light (350 nm) generates two photoproducts: the uncaged version of **1** or Diazepam (**2**) and the Nitroso hydroxy benzaldehyde **3** (*Top part*, Figure 4.4). The photophysical process can be followed spectrophotometrically with the absorption spectrum in Figure 4.4 (*Middle part*) showing the result of a 3 minutes irradiation (350 nm, 4.2 mW cm^{-2}) of a MeCN solution of **1**. Although the evolution of two new bands is clearly visible and indicated by the arrows (320 and 375 nm), a complication arises due to the UV-absorbing nature of all 3 compounds. It's impossible to clearly distinguish the temporal evolution of the singles species with a certainty. Hence, a HPLC analysis was carried out to clarify the photochemical reaction. A 100 µM solution of **1** in Toluene was photolyzed for two minutes (350 nm, 4.2 mW cm^{-2}) and, every 30 seconds, an aliquot of the reaction mixture was injected into a HPLC system coupled with a spectrophotometer detector (Figure 4.4, *bottom part*). Upon Irradiation, the photochemical reaction is essentially complete in two minutes with the disappearing of **1** and the concomitant evolution of two new bands corresponding to **2** and **3**, proving that **1** can be cleanly and efficiently converted to Diazepam. Moreover, the same process is reproducible in a water solution of **1** (see Figure 4.8).

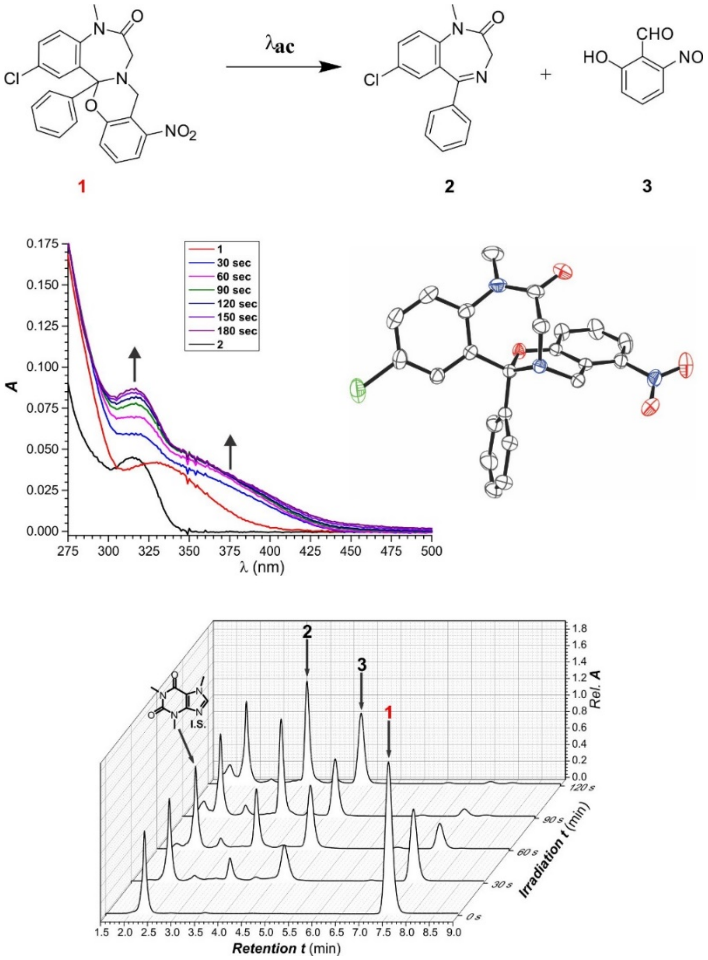

Figure 4.4. *Top*, Chemical structures of the reactant (**1**) and the photoproducts (**2** and **3**) obtained upon irradiation. *Middle left*, Absorption spectra (MeCN, 20 °C, 20 μM) recorded before (**1** and **2**) and during the photolysis of **1** for 3 minutes. *Middle right*, ORTEP representation of the geometry of **1** adopted in a single crystal. *Bottom*, HPLC traces [1.0 mL min^{-1}, C18 EVO, MeCN/H_2O (70:30, v/v), 254 nm] recorded before and during the photolysis (350 nm, 4.2 mW^{-2}) of a solution of **1** (0.1 mM, PhMe, 20 °C).

4.2.3 Biological Testing

Zebrafish is an established model in the Neurobiological community and various groups have reported the effects of Benzodiazepines on the fish[126-127]. While it remains a preliminary model, the Zebrafish offers the opportunity of a simple, economic and high throughput testing. Hence, it was chosen to test the effect of **1**: the light can be shined directly on the fish larvae (7 dpf) due to the transparency of their skin that would lead to the photoactivation in their brain and behavioral differences compared to a control will be recorded to assess the efficacy of the prodrug. In fact, Diazepam can affect the following parameters in zebrafishes: i) Locomotion ii) Shoal cohesion iii) Tank height iv) Color. Specifically, it has been shown that Diazepam counteracts the effect of the well known convulsant Pentylenetetrazole (PTZ) in Zebrafish. Thus, upon photoactivation, the Zebrafish should behave as they obtained a dose of Diazepam due to the conversion of **1** in **2** as represented in Figure 4.5: Schematically, the GABA and the GABA + CD group (*Top part*) should not show any major differences due to the fact that **1** is not active on the GABA$_{\mathbf{a}}$ receptor but, upon irradiation, the caged drug is converted into Diazepam that would bind to the receptor and elicits its effect (*Bottom part*).

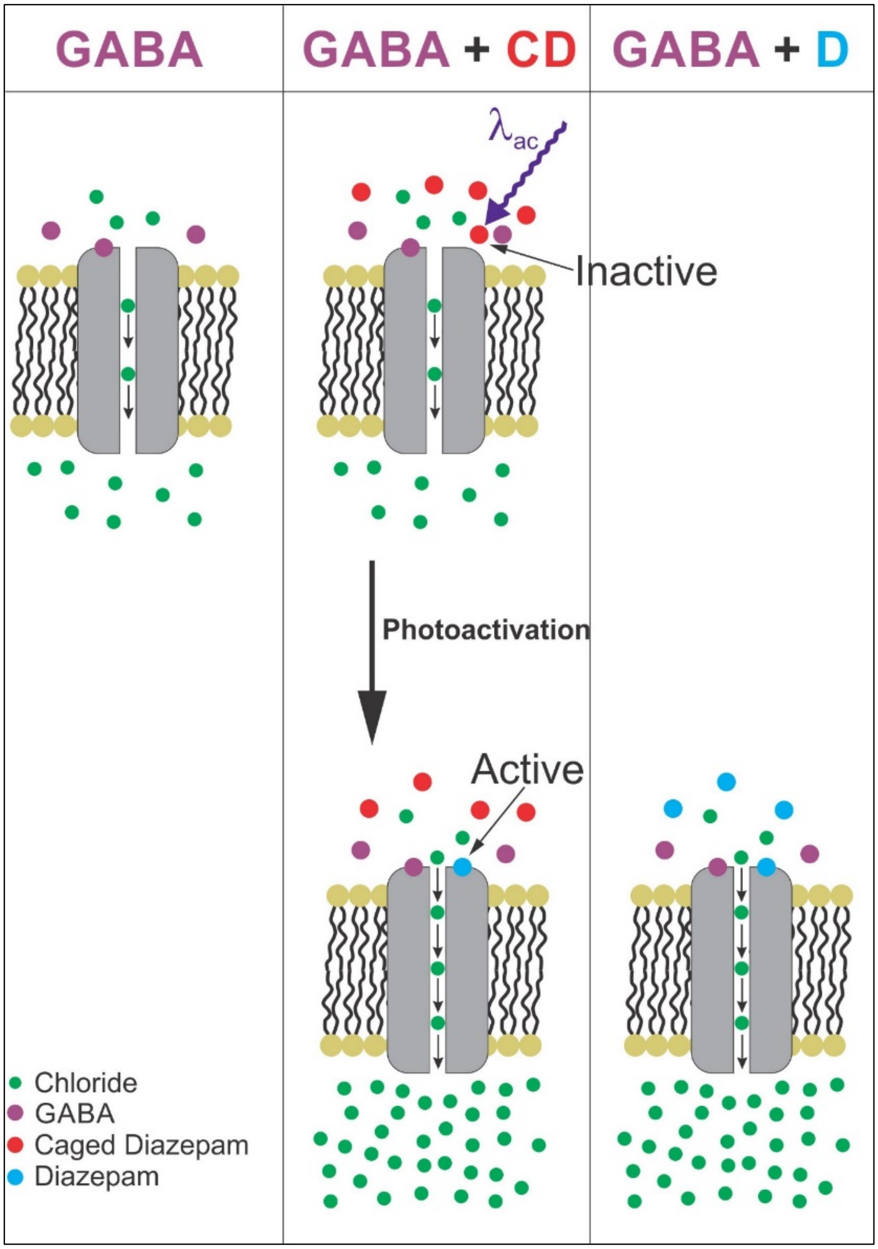

Figure 4.5. Schematic mechanism of modulation of the GABA$_a$ receptor activity upon photoconversion of **1** in Diazepam.

While Diazepam is fairly water soluble (5 mg/100mL), its prodrug **1** is harder to solubilize but its delivery can be achieved with the use of amphiphilic polymers described Chapter 1. Moreover, one potential drawback can be the inability of the drug to cross the blood brain barrier (BBB) of Zebrafish when administered in the same water they swim into. In order to proof this fundamental concept, Zebrafish were divided in two groups of 30 each (**D** or **CD**) and treated for 1 h with either Diazepam or its prodrug. The brains from the groups were dissected, homogenized and an aliquot of each group was injected into a HPLC system to assess the presence of **1** in the CNS. As shown in Figure 4.6, both compounds **1** and **2** were found in the dissected brains (as they overlap with the injected standards of **1** and **2** that present retention times of 7.4 and 3.6 minutes respectively) which indicates that **1** is able to cross the BBB in Zebrafish Larvae when administered in the same water they swim in.

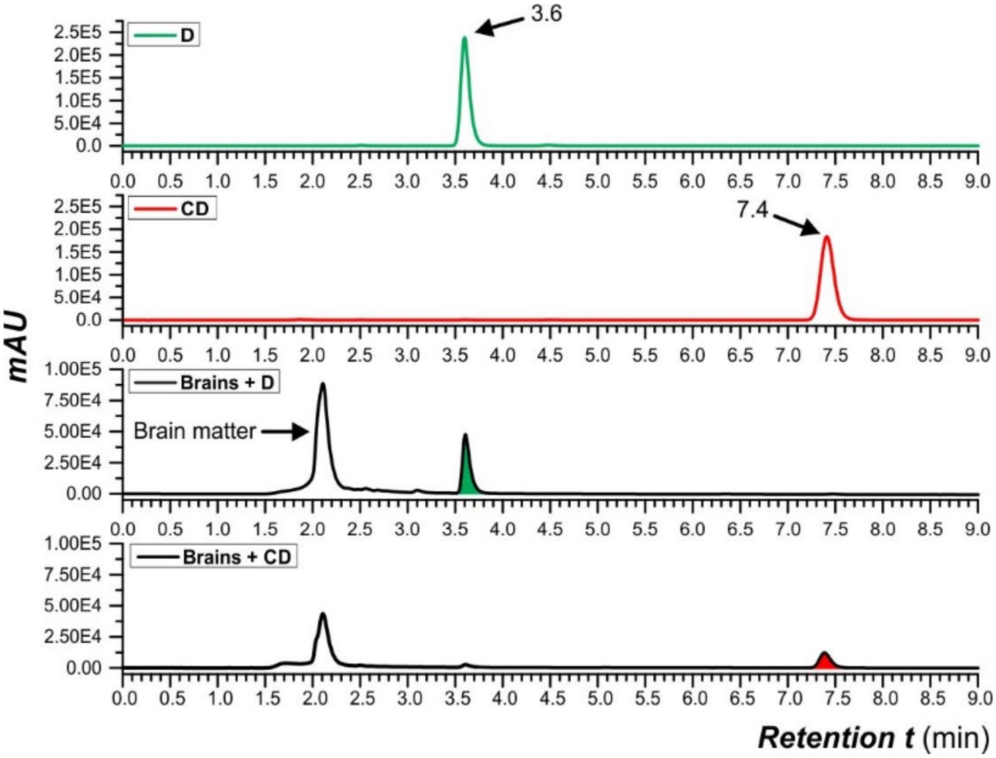

Figure 4.6. HPLC traces [1.0 mL min^{-1}, C18 EVO, MeCN/H$_2$O (70:30, v/v), 254 nm] of a solution of **1** or **2** (**CD** or **D**, 0.1 mM, MeCN, 20 °C) and homogeneized dissected brains of Zebrafish (n=30) pretreated with **1** or **2** for 1 h (see Experimental Section).

In Zebrafish, epileptic-like behavior can be induced by treatment with $GABA_a$ receptor antagonists and suppressed with the concomitant administration of anticonvulsant drugs such as Diazepam, Valproic acid, Carbamazepine, Zonisamide and many others.[128] One of the most common convulsant agent, PTZ (*top part,* Figure 4.7),[129] has been shown to induce seizure-like behavior in Zebrafish such as ictal, twitching, loss of posture, spiraling and uncoordinated jerky movement. Specifically 3 concentration-dependent seizure stages have been described with the fish experiencing clonus convulsions and loss of posture in Stage 3.[130] Nevertheless, the effect is reversible upon administration of $GABA_a$ receptor agonists.[128] In this instance, because of the well-known properties of Diazepam as antiepileptic agent, we designed an experiment to probe the efficacy of photoactivated **1** against PTZ-treated Zebrafish. The top part of Figure 4.7 shows a schematic timeline for the experiment: Zebrafish were treated for 35 minutes with either **1** or **2**, then irradiated with UV light for 5 minutes (350 nm, 4.2 mW cm^{-2}) and PTZ was added. The locomotor recording was started 2 minutes after PTZ addition.

Specifically, Zebrafish were divided in 8 groups: Control, PTZ (15 mM), D (15 μM), CD (15 μM) and the same four groups irradiated with UV light. Treatment with PTZ induced seizure-like behavior with the animals experiencing a sudden increase of movement in a matter of seconds upon addition. The locomotor recording showed a 61% increase of movement in the PTZ group compared to the Control one, as expected. The Diazepam group showed a 26 % decrease compared to the PTZ group, proving the efficacy of the anticonvulsant drug while the caged Diazepam group showed a less than 5% difference compared to the PTZ group, suggesting that the drug is not active. Upon irradiation and photoactivation, the 4 groups experienced a similar trend with the PTZ group still showing hyperactivity compared to the control one and the Diazepam group experiencing a 49% decrease compared to the PTZ group still assessing the efficacy of **2.**

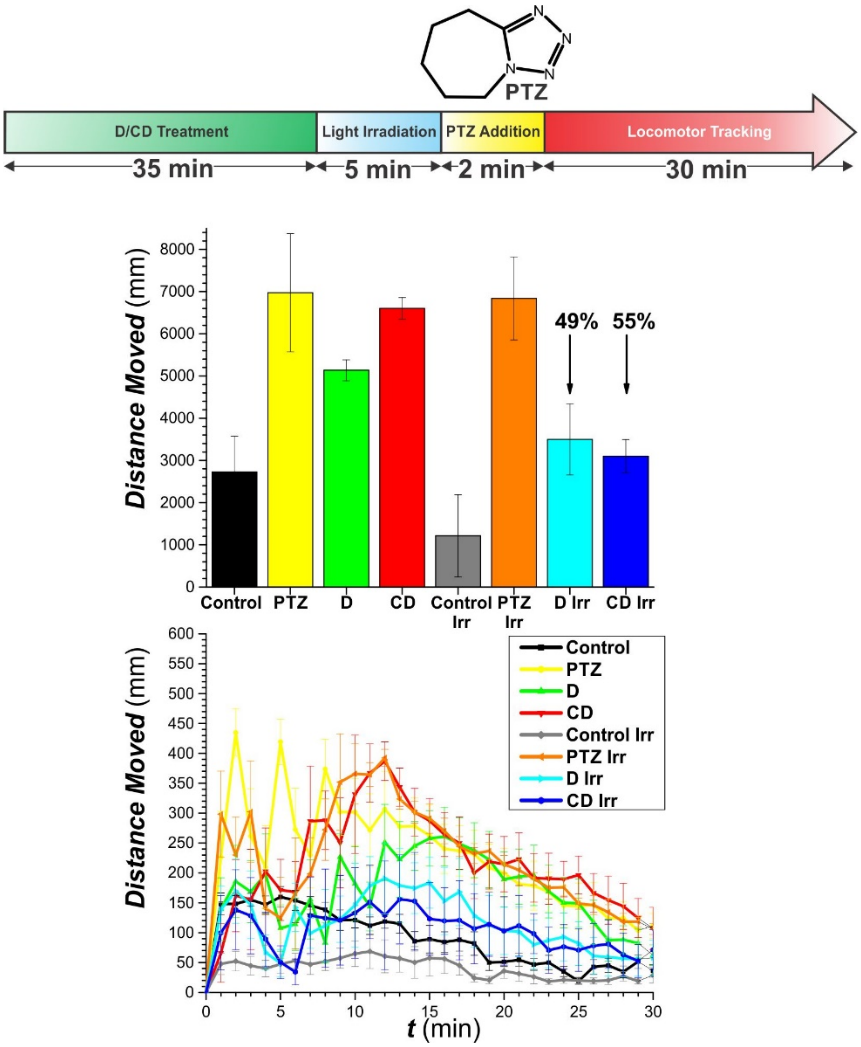

Figure 4.7. *Top*, schematic protocol timeline. *Middle*, total distance moved recorded in each Zebrafish group over 30 minutes of locomotor recording with relative error bars. *Bottom*, distance moved every minute for each Zebrafish group with relative error bars.

With our delight, the CD Irr group (Uncaged **1** or photogenerated Diazepam) showed a 55% decrease compared to the PTZ one and resulted more efficient than Diazepam itself suggesting that the uncaging process is efficient enough to counteract the effect of the convulsant agent. Specifically, the timeline trend of the recording process is represented in the *bottom part* of Figure 4.7 that shows the distance moved every minute for each group. Astonishingly, the CD Irr group trend is more similar to the D or D Irr than the CD group, suggesting that the photoconversion is working properly. Thus, this proves that **1** can be used as a photoactivatable prodrug of Diazepam.

4.3 Conclusion

This work could provide a completely new investigational tool to the neuroscientific community and set the basis for a new type of research: easy, effective and cheap compared to the actual methods. A photoactivatable version of Diazepam was easily obtained and can be activated with any kind of UV lamp centered at 350 nm, a very common tool in research labs. Not only it brings with it a huge potential, but it would simplify enormously neuroscience research avoiding the needs for genetic manipulation as opposed to optogenetics or chemogenetics. To further extend the scope of the project and study in depth the activation of specific neuronal subpopulations and their role in the CNS, **1** will be tested using mouse brain slices[131]. In fact, fixed doses of the aforementioned molecule can be delivered to very specific neural circuits while studying the influence of the same on the entire brain slice. Electrophysiological techniques (Patch Clamp) will be used for the purpose.

4.4 Experimental Section

Synthesis. Chemicals were purchased from commercial sources and used as received. CH_2Cl_2 and MeCN were distilled over CaH_2. Tetrahydrofuran (THF) was distilled over Na and benzophenone. H_2O (18.2 MΩ cm) was purified with a Barnstead International NANOpure Diamond analytical system. Compound **7** was prepared following literature protocols.[1] EISMS was performed with a Bruker micrOTO-Q II spectrometer. NMR spectra were recorded with Bruker 300, 400 and 500 spectrometers.

5. 2-Amino-5-chlorobenzophenone (10 g, 43.16 mmol) was dissolved in 195 ml of Et_2O and Pyridine (Py, 3.48 mL, 43.16 mmol) was added. Bromo acetyl bromide (4.51 mL, 51.79 mmol) was added dropwise and the mixture was stirred at RT for 2 h. The reaction mixture was filtered over a büchner funnel and the filtrate was washed with DI H_2O (3 x 150 mL), dried over Na_2SO_4 and evaporated at reduced pressure to afford a white powder. Recrystallization from DCM afforded **5** as white crystals (12.2 g, 80 %). HRESIMS: *m/z* calcd for $C_{15}H_{11}BrClNO_2$: 350.9662; found: 373.9554 $[M + Na]^+$; ^1H NMR (400 MHz, $CDCl_3$) δ = 11.32 (s, 1H), 8.60 – 8.56 (m, 1H), 7.77 – 7.71 (m, 2H), 7.69 – 7.61 (m, 1H), 7.60 – 7.48 (m, 4H), 4.03 (s, 2H).

6. To a solution of **5** (5 g, 14.18 mmol) in 90 mL of EtOH were added Methenamine (4.38 g, 31.21 mmol) and Ammonium acetate (2.4 g, 31.21 mmol). The reaction mixture was refluxed for 6 h. After cooling and evaporation at reduced pressure, 55 mL of DI H_2O were added to the reaction flask and the mixture was stirred at 60 °C for 30 min. Upon cooling, the suspension was filtered over a büchner funnel to recover a pink solid that was dissolved in 15 mL of Toluene and stirred at 70 °C for 30 min. Upon evaporation, **6** was obtained as a light pink powder (2.5 g, 65 %). HRESIMS: *m/z* calcd for $C_{15}H_{11}ClN_2O$: 270.0560; found: 271.0642 $[M + 1]^+$; ^1H NMR (400 MHz, $CDCl_3$) $\delta = 9.55$ (s, 1H), 7.57 – 7.52 (m, 2H), 7.52 – 7.45 (m, 2H), 7.44-7.40 (m, 2H), 7.31 (d, *J* = 2.4 Hz, 1H), 7.17 (d, *J* = 8.7 Hz, 1H), 4.34 (s, 2H).

2. To a cooled solution of **6** (2 g, 7.39 mmol) in 15 mL of dry DMF was added Sodium ethoxide (EtONa, 3.03 mL, 8.13 mmol, 21% w/w) and the mixture was stirred at 0 °C for 20 min. Upon reaching RT, Methyl iodide (CH_3I, 1.4 mL, 22.17 mmol) was added dropwise and the reaction mixture was stirred at RT for 1 h. The suspension was filtered and the filtrate was added with DI H_2O (150 mL) and extracted with EtOAc (3 x 100 mL). The pooled organic layers were washed with a LiCl sat. aq. (5 x 200 mL), dried over Na_2SO_4 and evaporated at reduced pressure. The residue was purified by column chromatography [SiO_2, Dichloromethane/n-Hexane (40:10, v/v)] to afford **2** (1.97 g, 94%) as a white powder. HRESIMS: *m/z* calcd for $C_{16}H_{13}ClN_2O$: 284.0716; found: 285.0802 $[M + H]^+$; ^1H NMR (400 MHz, $CDCl_3$) $\delta = 7.65$ – 7.57 (m, 2H), 7.56 – 7.38 (m, 4H), 7.35 – 7.27 (m, 2H), 4.84 (d, *J* = 10.8 Hz, 1H), 3.78 (d, *J* = 10.8 Hz, 1H), 3.40 (s, 3H).

1. To a solution of **2** (200 mg, 0.7 mmol) in 10 mL of dry MeCN was added **7** (195 mg, 0.84 mmol). The reaction mixture was stirred at RT for 24 h. The solvent was evaporated at reduced pressure and the residue was dissolved in 20 mL of DCM, washed with $NaHCO_3$ aq. sat. (3 x 20 mL), dried over Na_2SO_4 and evaporated at reduced pressure. The residue was purified by column chromatography [SiO_2, Dichloromethane/n-Hexane/Ethyl acetate (30:20:10, v/v) + 1% TEA] to afford **1** (181 mg, 59 %) as a white solid. HRESIMS: *m/z* calcd for $C_{23}H_{18}ClN_3O_4$: 435.0986; found: 436.1087 $[M + H]^+$; ^1H NMR (300 MHz,

$CDCl_3$) δ = 8.04 – 7.35 (m, 7H), 7.33 – 7.21 (m, 2H), 7.16 (d, *J* = 8.1 Hz, 1H), 6.55 (s, 1H), 4.55 (dd, *J* = 19.1 Hz, 2H), 3.90 (d, *J* = 14.6 Hz, 1H), 3.48 (d, *J* = 14.5 Hz, 1H), 3.35 (s, 3H).

Crystallographic Analysis. Single crystals of **1**, suitable for diffraction analysis, grew from a $CHCl_3$ solution of the compound after the diffusion of pentane vapors at ambient temperature. The data crystal was mounted onto the end of a thin glass fiber using Paratone-N for data collection. X-ray intensity data were measured by using a Bruker SMART APEX2 CCD-based diffractometer using Mo Kα radiation (λ = 0.71073 Å).[84] The raw data frames were integrated with the SAINT+ program by using a narrow-frame integration algorithm.[84] Corrections for Lorentz and polarization effects were also applied with SAINT+. An empirical absorption correction based on the multiple measurement of equivalent reflections was applied using the program SADABS. All structures were solved by a combination of direct methods and difference Fourier syntheses, and refined by full-matrix least-squares on F^2, by using the SHELXTL software package.[85-86] All non-hydrogen atoms were refined with anisotropic displacement parameters. Hydrogen atoms were placed in geometrically-idealized positions and included, as standard riding atoms, during the least squares refinements. Crystal data, data collection parameters and results of the analyses are listed in Table 4.0. Compound **1** crystallized in the triclinic crystal system. The space group $P\bar{1}$ was assumed and confirmed by the successful refinement of the structure.

Table 4.0. Crystallographic Data for Compound **1**.

	1
Empirical formula	$C_{23}H_{18}ClN_3O_4$
Formula weight	435.85
Crystal system	Triclinic
Lattice parameters	
a (Å)	10.6449(5)
b (Å)	10.6689(4)
c (Å)	11.3241(5)
α (deg)	113.845(1)
β (deg)	99.835(1)
γ (deg)	110.206(1)
V (Å^3)	1029.17(8)
Space group	$P\bar{1}$ (#2)
Z value	2
ρ_{calc} (g / cm^3)	1.406
μ (Mo Kα) (mm^{-1})	0.222
Temperature (K)	296
$2\Theta_{max}$ (°)	58.0
No. Obs. ($I > 2\sigma(I)$)	4605
No. Parameters	282
Goodness of fit	1.032
Max. shift in cycle	0.000
Residuals*:R1; wR2	0.0487; 0.1322
Absorption Correction, Max/min	Multi-scan 0.7462/0.4313
Largest peak in Final Diff. Map (e$^-$ / Å^3)	0.335

*$R1 = \Sigma_{hkl}(\left|\,|F_{obs}| - |F_{calc}|\,\right|)/\Sigma_{hkl}|F_{obs}|$; $wR2 = [\Sigma_{hkl}w(|F_{obs}| - |F_{calc}|)^2/\Sigma_{hkl}wF_{obs}{}^2]^{1/2}$, $w = 1/\sigma^2(F_{obs})$; $GOF = [\Sigma_{hkl}w(|F_{obs}| - |F_{calc}|)^2/(n_{data} - n_{vari})]^{1/2}$.

Polymer Nanoparticles. A CH_2Cl_2 solution of **1** (6.5 µg mL^{-1} for biological studies, 10 µg mL^{-1} for spectroscopy, 0.4 mg mL^{-1} for brains dissections) and **4** (0.5 mg mL^{-1} for spectroscopy, 5 mg mL^{-1} for biological studies) was heated at 40 °C in an open vial. After the evaporation of the solvent, the residue was purged with air, dispersed in system-water (SW) (KCl 0.05g/L, NaHCO3 0.025g/L, NaCl 3.5g/L and CaCl2 0.1g/L, pH 7.0-7.2), sonicated for 5 min and flashed through a syringe filter with a pore size of 0.2 µm. The filtrate was used for the biological and spectroscopic experiments without any further purification.

Spectroscopy. Absorption spectra were recorded with a Varian Cary 100 Bio spectrometer in quartz cells with a path length of 1.0 cm. Emission spectra were recorded with a Varian Cary Eclipse spectrometer in aerated solutions. Photolyses were performed in aerated solutions with a Luzchem Research LZC-4V photoreactor, operating at 350 nm (4.2 mW cm^{-2}), and the corresponding quantum yields were determined with a potassium ferrioxalate actinometer, according to an established procedure.[1] Chromatograms were recorded with a Phenomenex Kinetex (5 µm EVO C18 100 Å) column (4.6 × 250 mm) operated with a Shimadzu Nexera X2 system in MeCN/H_2O (70:30 v/v) at a flow rate of 1.0 mL min^{-1} and detection wavelength of 350 nm.

Animals. Experiments were conducted on offspring from Danio rerio wild-type strains AB, Tubingen, and BWT (a fish store strain from Long Island). Zebrafish were maintained on a 14-hr light and 10-hr dark cycle at 28.5 °C and fed twice daily. Fertilized eggs were obtained by natural crossing after removing a divider at first light. Embryos were raised in glass petri dishes with system water at 28.5 8C in an incubator with the same light/dark cycle, and staged properly.[132] Zebrafish embryos were collected between 24 hpf and Zebrafish larvae were used at 7 dpf. All animal protocols were approved by the Institutional Animal Care and Use Committee of University of Miami.

Brain Dissections. Zebrafish 7 dpf (20) were treated for 1 h with either **1** (1 mM, polymer aided dissolution) or **2** (1 mM, aqueous solution). After rinsing them thoroughly with SW, they were placed in a basket and immersed in a liquid nitrogen bath to sacrifice them. Brains were surgically dissected out and kept at 0 °C in a 4:1 MeCN – system-water. The suspension was homogenized in an eppendorf tube, centrifuged (10,000g at 4° for 20 min) and 20 uL of the surnatant were injected into the HPLC.

Locomotor Tracking. Zebrafish larvae 7 dpf were divided into 8 groups and placed in a 48-well plate (6 larvae each group, Control, Control Irr., PTZ, PTZ Irr, D, D Irr, CD, CD Irr.). Control groups were placed in 1 mL of SW. The larvae in the D and CD groups were preincubated for 35 minutes with either **1** (15 μM, polymer aided dissolution) or **2** (15 μM, aqueous solution) and rinsed thoroughly with SW before being placed in the wells with 0.5 mL of SW. PTZ groups were placed in 0.5 mL of SW. The Non-irradiated groups were covered with a protecting mask and the 48-well plate was placed in a Luzchem Research LZC-4V photoreactor, operating at 350 nm (4.2 mW cm^{-2}) for 5 minutes. Then, PTZ (30 mM, 0.5 mL) was added to all the groups beside the Control and the plate was placed in the dark chamber of an automated tracking device (Noldus Daniovision). The total locomotor activity was quantified using the EthoVision XT software.

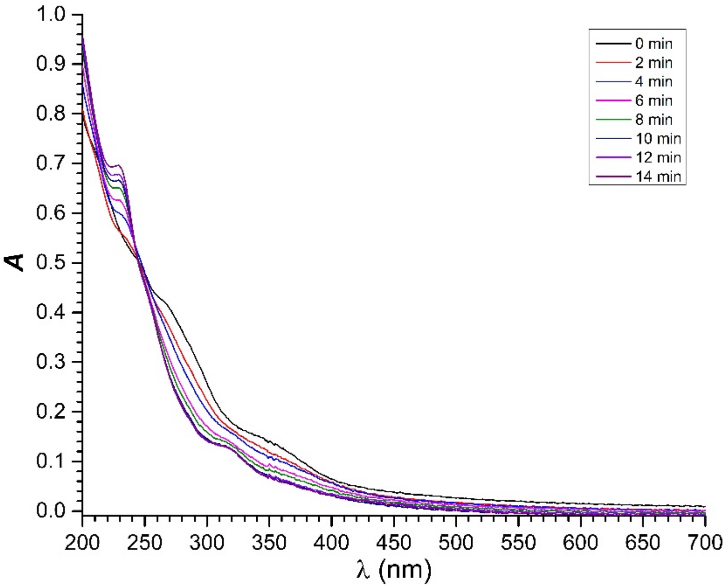

Figure 4.8. Absorption spectra (H_2O, 20 °C, 20 μM) recorded before and during the photolysis of **1** for 14 minutes.

References

1. Zhang, Y.; Swaminathan, S.; Tang, S.; Garcia-Amorós, J.; Boulina, M.; Captain, B.; Baker, J. D.; Raymo, F. M., Photoactivatable Bodipys Designed to Monitor the Dynamics of Supramolecular Nanocarriers. *Journal of the American Chemical Society* **2015,** *137* (14), 4709-4719.

2. Zhang, Y.; Tang, S.; Sansalone, L.; Baker, J. D.; Raymo, F. M., A Photoswitchable Fluorophore for the Real-Time Monitoring of Dynamic Events in Living Organisms. *Chemistry – A European Journal* **2016,** *22* (42), 15027-15034.

3. Weber, G., [1] Fluorescence in Biophysics: Accomplishments and Deficiencies. In *Methods in Enzymology*, Academic Press: 1997; Vol. 278, pp 1-15.

4. Eftink, M. R., [11] Fluorescence Methods for Studying Equilibrium Macromolecule-Ligand Interactions. In *Methods in Enzymology*, Academic Press: 1997; Vol. 278, pp 221-257.

5. Shahzad, A.; Edetsberger, M.; Koehler, G., Fluorescence Spectroscopy: An Emerging Excellent Diagnostic Tool in Medical Sciences. *Applied Spectroscopy Reviews* **2010,** *45* (1), 1-11.

6. Kobayashi, H.; Choyke, P. L., Target-Cancer-Cell-Specific Activatable Fluorescence Imaging Probes: Rational Design and in Vivo Applications. *Accounts of Chemical Research* **2011,** *44* (2), 83-90.

7. Kosaka, N.; Ogawa, M.; Choyke, P. L.; Kobayashi, H., Clinical Implications of near-Infrared Fluorescence Imaging in Cancer. *Future Oncology* **2009,** *5* (9), 1501-1511.

8. Wilson, J. N., Fluorescent Neurotransmitter Analogs. In *Fluorescent Analogues of Biomolecular Building Blocks: Design and Applications*, John Wiley & Sons, Inc.: 2016; pp 393-407.

9. Connolly, G. P., Fibroblast Models of Neurological Disorders: Fluorescence Measurement Studies. *Trends in Pharmacological Sciences* **1998,** *19* (5), 171-177.

10. Mirasoli, M.; Guardigli, M.; Roda, A., Chemiluminescence in Biomedicine. In *Applied Photochemistry: When Light Meets Molecules*, Bergamini, G.; Silvi, S., Eds. Springer International Publishing: Cham, 2016; pp 427-458.

11. Wilson, T.; Hastings, J. W., Bioluminescence. *Annual Review of Cell & Developmental Biology* **1998,** *14* (1), 197.

12. Contag, C. H.; Bachmann, M. H., Advances in in Vivo Bioluminescence Imaging of Gene Expression. *Annual Review of Biomedical Engineering* **2002,** *4* (1), 235-260.

13. Owens, E. A.; Lee, S.; Choi, J.; Henary, M.; Choi, H. S., Nir Fluorescent Small Molecules for Intraoperative Imaging. *Wiley Interdisciplinary Reviews: Nanomedicine and Nanobiotechnology* **2015,** *7* (6), 828-838.

14. Zhang, J.; Campbell, R. E.; Ting, A. Y.; Tsien, R. Y., Creating New Fluorescent Probes for Cell Biology. *Nature Reviews Molecular Cell Biology* **2002,** *3* (12), 906.

15. Lippincott-Schwartz, J.; Patterson, G. H., Development and Use of Fluorescent Protein Markers in Living Cells. *Science* **2003,** *300* (5616), 87.

16. Wolfbeis, O. S., An Overview of Nanoparticles Commonly Used in Fluorescent Bioimaging. *Chemical Society Reviews* **2015,** *44* (14), 4743-4768.

17. Introduction to Fluorescence. In *Principles of Fluorescence Spectroscopy*, Lakowicz, J. R., Ed. Springer US: Boston, MA, 2006; pp 1-26.

18. Valeur, B.; Berberan-Santos, M. N., Structural Effects on Fluorescence Emission. In *Molecular Fluorescence*, Wiley-VCH Verlag GmbH & Co. KGaA: 2012; pp 75-107.

19. Valeur, B.; Berberan-Santos, M. N., Environmental Effects on Fluorescence Emission. In *Molecular Fluorescence*, Wiley-VCH Verlag GmbH & Co. KGaA: 2012; pp 109-140.

20. Valeur, B.; Berberan-Santos, M. N., Effects of Intermolecular Photophysical Processes on Fluorescence Emission. In *Molecular Fluorescence*, Wiley-VCH Verlag GmbH & Co. KGaA: 2012; pp 141-179.

21. Valeur, B.; Berberan-Santos, M. N., Fluorescence Polarization: Emission Anisotropy. In *Molecular Fluorescence*, Wiley-VCH Verlag GmbH & Co. KGaA: 2012; pp 181-212.

22. Valeur, B.; Berberan-Santos, M. N., Excitation Energy Transfer. In *Molecular Fluorescence*, Wiley-VCH Verlag GmbH & Co. KGaA: 2012; pp 213-261.

23. Quenching of Fluorescence. In *Principles of Fluorescence Spectroscopy*, Lakowicz, J. R., Ed. Springer US: Boston, MA, 2006; pp 277-330.

24. Mechanisms and Dynamics of Fluorescence Quenching. In *Principles of Fluorescence Spectroscopy*, Lakowicz, J. R., Ed. Springer US: Boston, MA, 2006; pp 331-351.

25. Energy Transfer to Multiple Acceptors in One,Two, or Three Dimensions. In *Principles of Fluorescence Spectroscopy*, Lakowicz, J. R., Ed. Springer US: Boston, MA, 2006; pp 507-528.

26. Fabre, R., Application of the Phenomena of Fluorescence in Biological Chemistry. *Bulletin de la Societe de Chimie Biologique* **1925,** *7*, 1024-1038.

27. Albani, J. R., Phosphorescence, Fluorescence, and Chemiluminescence in Clinical Chemistry. In *Encyclopedia of Analytical Chemistry*, John Wiley & Sons, Ltd: 2006.

28. Möckl, L.; Lamb, D. C.; Bräuchle, C., Super-Resolved Fluorescence Microscopy: Nobel Prize in Chemistry 2014 for Eric Betzig, Stefan Hell, and William E. Moerner. *Angewandte Chemie International Edition* **2014,** *53* (51), 13972-13977.

29. Garland, M.; Yim, Joshua J.; Bogyo, M., A Bright Future for Precision Medicine: Advances in Fluorescent Chemical Probe Design and Their Clinical Application. *Cell Chemical Biology* **2016,** *23* (1), 122-136.

30. Becker, M. M.; Wang, Z., Origin of Ultraviolet Damage in DNA. *Journal of Molecular Biology* **1989,** *210* (3), 429-438.

31. Davies, R. J. H., Ultraviolet Radiation Damage in DNA. *Biochemical Society Transactions* **1995,** *23* (2), 407.

32. Teale, F. W. J.; Weber, G., Ultraviolet Fluorescence of the Aromatic Amino Acids. *Biochemical Journal* **1957,** *65* (3), 476.

33. Steven, L. J., Optical Properties of Biological Tissues: A Review. *Physics in Medicine & Biology* **2013,** *58* (11), R37.

34. Frangioni, J. V., In Vivo near-Infrared Fluorescence Imaging. *Current Opinion in Chemical Biology* **2003,** *7* (5), 626-634.

35. Hilderbrand, S. A.; Weissleder, R., Near-Infrared Fluorescence: Application to in Vivo Molecular Imaging. *Current Opinion in Chemical Biology* **2010,** *14* (1), 71-79.

36. Guo, Z.; Park, S.; Yoon, J.; Shin, I., Recent Progress in the Development of near-Infrared Fluorescent Probes for Bioimaging Applications. *Chemical Society Reviews* **2014,** *43* (1), 16-29.

37. Yuan, L.; Lin, W.; Zheng, K.; He, L.; Huang, W., Far-Red to near Infrared Analyte-Responsive Fluorescent Probes Based on Organic Fluorophore Platforms for Fluorescence Imaging. *Chemical Society Reviews* **2013,** *42* (2), 622-661.

38. Lord, S. J.; Conley, N. R.; Lee, H.-l. D.; Samuel, R.; Liu, N.; Twieg, R. J.; Moerner, W. E., A Photoactivatable Push−Pull Fluorophore for Single-Molecule Imaging in Live Cells. *Journal of the American Chemical Society* **2008,** *130* (29), 9204-9205.

39. Fleming, I., Molecular Orbital Theory. In *Molecular Orbitals and Organic Chemical Reactions*, John Wiley & Sons, Ltd: 2010; pp 1-67.

40. Deniz, E.; Tomasulo, M.; Cusido, J.; Yildiz, I.; Petriella, M.; Bossi, M. L.; Sortino, S.; Raymo, F. M., Photoactivatable Fluorophores for Super-Resolution Imaging

Based on Oxazine Auxochromes. *The Journal of Physical Chemistry C* **2012,** *116* (10), 6058-6068.

41. Raymo, F.; #xe7; M., i., Photoactivatable Fluorophores. *ISRN Physical Chemistry* **2012,** *2012*, 15.

42. Staras, K.; Mikulincer, D.; Gitler, D., Monitoring and Quantifying Dynamic Physiological Processes in Live Neurons Using Fluorescence Recovery after Photobleaching. *Journal of Neurochemistry* **2013,** *126* (2), 213-222.

43. Ishikawa-Ankerhold, H. C.; Ankerhold, R.; Drummen, G. P. C., Advanced Fluorescence Microscopy Techniques—Frap, Flip, Flap, Fret and Flim. *Molecules* **2012,** *17* (4).

44. Loudet, A.; Burgess, K., Bodipy Dyes and Their Derivatives: Syntheses and Spectroscopic Properties. *Chemical Reviews* **2007,** *107* (11), 4891-4932.

45. Boens, N.; Leen, V.; Dehaen, W., Fluorescent Indicators Based on Bodipy. *Chem Soc Rev* **2012,** *41* (3), 1130-72.

46. Klan, P.; Solomek, T.; Bochet, C. G.; Blanc, A.; Givens, R.; Rubina, M.; Popik, V.; Kostikov, A.; Wirz, J., Photoremovable Protecting Groups in Chemistry and Biology: Reaction Mechanisms and Efficacy. *Chem Rev* **2013,** *113* (1), 119-91.

47. Barltrop, J. A.; Plant, P. J.; Schofield, P., Photosensitive Protective Groups. *Chemical Communications (London)* **1966,** (22), 822-823.

48. Schmierer, T.; Laimgruber, S.; Haiser, K.; Kiewisch, K.; Neugebauer, J.; Gilch, P., Femtosecond Spectroscopy on the Photochemistry of Ortho-Nitrotoluene. *Phys Chem Chem Phys* **2010,** *12* (48), 15653-64.

49. Il'ichev, Y. V.; Schworer, M. A.; Wirz, J., Photochemical Reaction Mechanisms of 2-Nitrobenzyl Compounds: Methyl Ethers and Caged Atp. *J Am Chem Soc* **2004,** *126* (14), 4581-95.

50. Garcia-Amoros, J.; Tang, S.; Zhang, Y.; Thapaliya, E. R.; Raymo, F. M., Self-Assembling Nanoparticles of Amphiphilic Polymers for in Vitro and in Vivo Fret Imaging. *Top Curr Chem* **2016,** *370*, 29-59.

51. Ziessel, R.; Ulrich, G.; Harriman, A., The Chemistry of Bodipy: A New El Dorado for Fluorescence Tools. *New Journal of Chemistry* **2007,** *31* (4), 496-501.

52. Ulrich, G.; Ziessel, R.; Harriman, A., The Chemistry of Fluorescent Bodipy Dyes: Versatility Unsurpassed. *Angewandte Chemie International Edition* **2008,** *47* (7), 1184-1201.

53. Benstead, M.; Mehl, G. H.; Boyle, R. W., 4,4′-Difluoro-4-Bora-3a,4a-Diaza-S-Indacenes (Bodipys) as Components of Novel Light Active Materials. *Tetrahedron* **2011,** *67* (20), 3573-3601.

54. Kamkaew, A.; Lim, S. H.; Lee, H. B.; Kiew, L. V.; Chung, L. Y.; Burgess, K., Bodipy Dyes in Photodynamic Therapy. *Chemical Society Reviews* **2013,** *42* (1), 77-88.

55. Lu, H.; Mack, J.; Yang, Y.; Shen, Z., Structural Modification Strategies for the Rational Design of Red/Nir Region Bodipys. *Chemical Society Reviews* **2014,** *43* (13), 4778-4823.

56. Ni, Y.; Wu, J., Far-Red and near Infrared Bodipy Dyes: Synthesis and Applications for Fluorescent Ph Probes and Bio-Imaging. *Organic & Biomolecular Chemistry* **2014,** *12* (23), 3774-3791.

57. Kobayashi, T.; Komatsu, T.; Kamiya, M.; Campos, C.; González-Gaitán, M.; Terai, T.; Hanaoka, K.; Nagano, T.; Urano, Y., Highly Activatable and Environment-Insensitive Optical Highlighters for Selective Spatiotemporal Imaging of Target Proteins. *Journal of the American Chemical Society* **2012,** *134* (27), 11153-11160.

58. Shaban Ragab, S.; Swaminathan, S.; Deniz, E.; Captain, B.; Raymo, F. M., Fluorescence Photoactivation by Ligand Exchange around the Boron Center of a Bodipy Chromophore. *Organic Letters* **2013,** *15* (12), 3154-3157.

59. Ragab, S. S.; Swaminathan, S.; Baker, J. D.; Raymo, F. M., Activation of Bodipy Fluorescence by the Photoinduced Dealkylation of a Pyridinium Quencher. *Physical Chemistry Chemical Physics* **2013,** *15* (36), 14851-14855.

60. Amamoto, T.; Hirata, T.; Takahashi, H.; Kamiya, M.; Urano, Y.; Santa, T.; Kato, M., Spatiotemporal Activation of Molecules within Cells Using Silica Nanoparticles Responsive to Blue-Green Light. *Journal of Materials Chemistry B* **2015,** *3* (37), 7427-7433.

61. Goswami, P. P.; Syed, A.; Beck, C. L.; Albright, T. R.; Mahoney, K. M.; Unash, R.; Smith, E. A.; Winter, A. H., Bodipy-Derived Photoremovable Protecting Groups Unmasked with Green Light. *Journal of the American Chemical Society* **2015,** *137* (11), 3783-3786.

62. Wysocki, L. M.; Lavis, L. D., Advances in the Chemistry of Small Molecule Fluorescent Probes. *Current Opinion in Chemical Biology* **2011,** *15* (6), 752-759.

63. Puliti, D.; Warther, D.; Orange, C.; Specht, A.; Goeldner, M., Small Photoactivatable Molecules for Controlled Fluorescence Activation in Living Cells. *Bioorganic & Medicinal Chemistry* **2011,** *19* (3), 1023-1029.

64. Li, W.-h.; Zheng, G., Photoactivatable Fluorophores and Techniques for Biological Imaging Applications. *Photochemical & Photobiological Sciences* **2012,** *11* (3), 460-471.

65. Raymo, F. M., Photoactivatable Synthetic Dyes for Fluorescence Imaging at the Nanoscale. *The Journal of Physical Chemistry Letters* **2012,** *3* (17), 2379-2385.

66. Klán, P.; Šolomek, T.; Bochet, C. G.; Blanc, A.; Givens, R.; Rubina, M.; Popik, V.; Kostikov, A.; Wirz, J., Photoremovable Protecting Groups in Chemistry and Biology: Reaction Mechanisms and Efficacy. *Chemical Reviews* **2013,** *113* (1), 119-191.

67. Raymo, F. M., Photoactivatable Synthetic Fluorophores. *Physical Chemistry Chemical Physics* **2013,** *15* (36), 14840-14850.

68. Dirks, R. W.; Molenaar, C.; Tanke, H. J., Methods for Visualizing Rna Processing and Transport Pathways in Living Cells. *Histochemistry and Cell Biology* **2001,** *115* (1), 3-11.

69. Ellis-Davies, G. C. R., Caged Compounds: Photorelease Technology for Control of Cellular Chemistry and Physiology. *Nature Methods* **2007,** *4*, 619.

70. Xu, Y.; Melia, T. J.; Toomre, D. K., Using Light to See and Control Membrane Traffic. *Current Opinion in Chemical Biology* **2011,** *15* (6), 822-830.

71. Betzig, E., Single Molecules, Cells, and Super-Resolution Optics (Nobel Lecture). *Angewandte Chemie International Edition* **2015,** *54* (28), 8034-8053.

72. Hell, S. W., Nanoscopy with Focused Light (Nobel Lecture). *Angewandte Chemie International Edition* **2015,** *54* (28), 8054-8066.

73. Moerner, W. E., Single-Molecule Spectroscopy, Imaging, and Photocontrol: Foundations for Super-Resolution Microscopy (Nobel Lecture). *Angewandte Chemie International Edition* **2015,** *54* (28), 8067-8093.

74. Thapaliya, E. R.; Zhang, Y.; Raymo, F. M., Fluorescence Patterning with Mild Illumination in Polymer Films of Photocleavable Oxazines. *Journal of Materials Chemistry C* **2017,** *5* (5), 1179-1183.

75. Turro , N. J. R., V.; Scaiano, J.C., *Principles of Molecular Photochemistry: An Introduction*. University Science Book: Herndon: 2009.

76. Parr, R. G. In *Density Functional Theory of Atoms and Molecules*, Horizons of Quantum Chemistry, Dordrecht, 1980//; Fukui, K.; Pullman, B., Eds. Springer Netherlands: Dordrecht, 1980; pp 5-15.

77. Furche, F.; Ahlrichs, R., Adiabatic Time-Dependent Density Functional Methods for Excited State Properties. *The Journal of Chemical Physics* **2002,** *117* (16), 7433-7447.

78. Woodward, R. B. A., W. A.; Beaton, J. M.; Bickelhaupt, F.; Bonnett, R.; Buchschacher, P.; Closs, G. L.; Dutler, H.; Hannah, J.; Hauck, F. P.; Itŏ, S.; Langemann, A.; Le Goff, E.; Leimgruber, W.; Lwowski, W.; Sauer, J.; Valenta, Z.; Volz, H. , The Total Synthesis of Chlorophyll A. *Tetrahedron* **1990,** *46*.

79. Wu, L.; Burgess, K., A New Synthesis of Symmetric Boraindacene (Bodipy) Dyes. *Chemical Communications* **2008,** (40), 4933-4935.

80. Faler, C. A.; Joullié, M. M., The Kulinkovich Reaction in the Synthesis of Constrained N,N-Dialkyl Neurotransmitter Analogues. *Organic Letters* **2007,** *9* (10), 1987-1990.

81. Clegg, W.; Scott, A. J.; Wiesauer, C.; Weissensteiner, W.; Marder, T. B., (E)-2-[2-(4-Methylphenyl)Ethenyl]-1,3,2-Benzodioxaborole. *Acta Crystallographica Section E* **2004,** *60* (7), o1172-o1174.

82. Oslob, J. D. M., R. S.; Johnson, R.; Yang, H.; Evanchik, M.; Zaharia, C. A.; Cai, H.; Hu, L. W. Us20150210688 A1. **2015**.

83. Nguyen, A. H.; Sim, S. J., Nanoplasmonic Biosensor: Detection and Amplification of Dual Bio-Signatures of Circulating Tumor DNA. *Biosensors and Bioelectronics* **2015,** *67*, 443-449.

84. Bruker Analytical X-ray Systems, I., Madison: Wisconsin, USA, 2007 *Apex2 Version 2.2-0 and Saint+ Version 7.46a*, 2007.

85. Sheldrick, G., Crystal Structure Refinement with Shelxl. *Acta Crystallographica Section C* **2015,** *71* (1), 3-8.

86. Bruker Analytical X-ray Systems, I., Madison: Wisconsin, USA *Shelxtl Version 6.1*, 2000.

87. Würth, C.; Grabolle, M.; Pauli, J.; Spieles, M.; Resch-Genger, U., Relative and Absolute Determination of Fluorescence Quantum Yields of Transparent Samples. *Nature Protocols* **2013,** *8*, 1535.

88. Scaiano, J. C., *Handbook of Organic Photochemistry*. CRC Press: Boca Raton: **1989**.

89. Frisch, M. J. T., G. W.; Schlegel, H. B.; Scuseria, G. E.; Robb, M. A.; Cheeseman, J. R.; Scalmani, G.; Barone, V.; Mennucci, B.; Petersson, G. A.; Nakatsuji, H.; Caricato, M.; Li, X.; Hratchian, H. P.; Izmaylov, A. F.; Bloino, J.; Zheng, G.; Sonnenberg, J. L.; Hada, M.; Ehara, M.; Toyota, K.; Fukuda, R.; Hasegawa, J.; Ishida,

M.; Nakajima, T.; Honda, Y.; Kitao, O.; Nakai, H.; Vreven, T.; Montgomery, J. A. Jr.; Peralta, J. E.; Ogliaro, F.; Bearpark, M.; Heyd, J. J.; Brothers, E.; Kudin, K. N.; Staroverov, V. N.; Keith, T.; Kobayashi, R.; Normand, J.; Raghavachari, K.; Rendell, A.; Burant, J. C.; Iyengar, S. S.; Tomasi, J.; Cossi, M.; Rega, N.; Millam, J. M.; Klene, M.; Knox, J. E.; Cross, J. B.; Bakken, V.; Adamo, C.; Jaramillo, J.; Gomperts, R.; Stratmann, R. E.; Yazyev, O.; Austin, A. J.; Cammi, R.; Pomelli, C.; Ochterski, J. W.; Martin, R. L.; Morokuma, K.; Zakrzewski, V. G.; Voth, G. A.; Salvador, P.; Dannenberg, J. J.; Dapprich, S.; Daniels, A. D.; Farkas, Ö.; Foresman, J. B.; Ortiz, J. V.; Cioslowski, J.; Fox, D. J. *Gaussian 09*, Wallingford CT, **2013**.

90. Becke, A. D., Density-Functional Exchange-Energy Approximation with Correct Asymptotic Behavior. *Physical Review A* **1988,** *38* (6), 3098-3100.

91. Lee, C.; Yang, W.; Parr, R. G., Development of the Colle-Salvetti Correlation-Energy Formula into a Functional of the Electron Density. *Physical Review B* **1988,** *37* (2), 785-789.

92. Tomasi, J.; Mennucci, B.; Cammi, R., Quantum Mechanical Continuum Solvation Models. *Chemical Reviews* **2005,** *105* (8), 2999-3094.

93. Spradling, A. C.; Rubin, G. M., Transposition of Cloned P Elements into Drosophila Germ Line Chromosomes. *Science* **1982,** *218* (4570), 341.

94. Robiette, R.; Richardson, J.; Aggarwal, V. K.; Harvey, J. N., On the Origin of High E Selectivity in the Wittig Reaction of Stabilized Ylides: Importance of Dipole−Dipole Interactions. *Journal of the American Chemical Society* **2005,** *127* (39), 13468-13469.

95. Ziegler, K.; Späth, A.; Schaaf, E.; Schumann, W.; Winkelmann, E., Die Halogenierung Ungesättigter Substanzen in Der Allylstellung. *Justus Liebigs Annalen der Chemie* **1942,** *551* (1), 80-119.

96. Bhattacharya, A. K.; Thyagarajan, G., Michaelis-Arbuzov Rearrangement. *Chemical Reviews* **1981,** *81* (4), 415-430.

97. Blanchette, M. A.; Choy, W.; Davis, J. T.; Essenfeld, A. P.; Masamune, S.; Roush, W. R.; Sakai, T., Horner-Wadsworth-Emmons Reaction: Use of Lithium Chloride and an Amine for Base-Sensitive Compounds. *Tetrahedron Letters* **1984,** *25* (21), 2183-2186.

98. Maryanoff, B. E.; Reitz, A. B., The Wittig Olefination Reaction and Modifications Involving Phosphoryl-Stabilized Carbanions. Stereochemistry, Mechanism, and Selected Synthetic Aspects. *Chemical Reviews* **1989,** *89* (4), 863-927.

99. Maryanoff, B. E.; Reitz, A. B.; Duhl-Emswiler, B. A., Stereochemistry of the Wittig Reaction. Effect of Nucleophilic Groups in the Phosphonium Ylide. *Journal of the American Chemical Society* **1985,** *107* (1), 217-226.

100. Ribeiro Morais, G.; Vicente Miranda, H.; Santos, I. C.; Santos, I.; Outeiro, T. F.; Paulo, A., Synthesis and in Vitro Evaluation of Fluorinated Styryl Benzazoles as Amyloid-Probes. *Bioorganic & Medicinal Chemistry* **2011,** *19* (24), 7698-7710.

101. Dondoni, A.; Fantin, G.; Fogagnolo, M.; Medici, A.; Pedrini, P., Thiazolylmethylenetriphenylphosporane and Its Benzo Derivative: Stable and Practical Wittig Reagents for the Synthesis of Vinylthiazoles and Vinylbenzo: Two-Carbon Homologation of Aldehydes. *Tetrahedron* **1988,** *44* (7), 2021-2031.

102. Faingold, C. L.; Blumenfeld, H., Neuronal Networks in Brain Function, Cns Disorders, and Therapeutics. Academic Press,: London, 2014; pp. 1 online resource (xiv, 497 p.).

103. Brunton, L. L.; Knollmann, B. C.; Hilal-Dandan, R., Goodman & Gilman's the Pharmacological Basis of Therapeutics. Thirteenth edition. ed.; McGraw Hill Medical,: New York, 2018.

104. Abraham, D. J.; Rotella, D. P.; Burger, A., Burger's Medicinal Chemistry, Drug Discovery and Development. 7th ed.; Wiley,: Hoboken, N.J., 2010; p. 1 online resource (8 v.).

105. Chesselet, M.-F.; Carmichael, S. T., Animal Models of Neurological Disorders. *Neurotherapeutics* **2012,** *9* (2), 241-244.

106. McArthur, R. A., Translational Neuroimaging Tools for Cns Drug Discovery, Development and Treatment. Academic Press,: London ; Waltham, MA, 2013; p. 1 online resource.

107. Steinbach, K.; Merkler, D., Neuropathological Techniques to Investigate Cns Pathology in Experimental Autoimmune Encephalomyelitis (Eae). *Methods Mol Biol* **2016,** *1304*, 189-209.

108. Boyden, E. S.; Zhang, F.; Bamberg, E.; Nagel, G.; Deisseroth, K., Millisecond-Timescale, Genetically Targeted Optical Control of Neural Activity. *Nat Neurosci* **2005,** *8* (9), 1263-1268.

109. Roth, B. L., Dreadds for Neuroscientists. *Neuron* **2016,** *89* (4), 683-694.

110. Urban, D. J.; Roth, B. L., Dreadds (Designer Receptors Exclusively Activated by Designer Drugs): Chemogenetic Tools with Therapeutic Utility. *Annu Rev Pharmacol Toxicol* **2015,** *55*, 399-417.

111. Sternson, S. M.; Roth, B. L., Chemogenetic Tools to Interrogate Brain Functions. *Annu Rev Neurosci* **2014,** *37*, 387-407.

112. Lerch, M. M.; Hansen, M. J.; van Dam, G. M.; Szymanski, W.; Feringa, B. L., Emerging Targets in Photopharmacology. *Angewandte Chemie International Edition* **2016,** *55* (37), 10978-10999.

113. Broichhagen, J.; Frank, J. A.; Trauner, D., A Roadmap to Success in Photopharmacology. *Acc Chem Res* **2015,** *48* (7), 1947-60.

114. Velema, W. A.; Szymanski, W.; Feringa, B. L., Photopharmacology: Beyond Proof of Principle. *Journal of the American Chemical Society* **2014,** *136* (6), 2178-2191.

115. Fehrentz, T.; Kuttruff, C. A.; Huber, F. M. E.; Kienzler, M. A.; Mayer, P.; Trauner, D., Exploring the Pharmacology and Action Spectra of Photochromic Open-Channel Blockers. *ChemBioChem* **2012,** *13* (12), 1746-1749.

116. Fagg, G. E.; Foster, A. C., Amino Acid Neurotransmitters and Their Pathways in the Mammalian Central Nervous System. *Neuroscience* **1983,** *9* (4), 701-719.

117. von Bohlen und Halbach, O.; Dermietzel, R., Neurotransmitters. In *Neurotransmitters and Neuromodulators*, Wiley-VCH Verlag GmbH & Co. KGaA: 2003; pp 40-115.

118. Barnard, E. A.; Skolnick, P.; Olsen, R. W.; Mohler, H.; Sieghart, W.; Biggio, G.; Braestrup, C.; Bateson, A. N.; Langer, S. Z., International Union of Pharmacology. Xv. Subtypes of Γ-Aminobutyric Acid≪Sub≫a≪/Sub≫ Receptors: Classification on the Basis of Subunit Structure and Receptor Function. *Pharmacological Reviews* **1998,** *50* (2), 291.

119. Rudolph, U.; Knoflach, F., Beyond Classical Benzodiazepines: Novel Therapeutic Potential of Gabaa Receptor Subtypes. *Nat Rev Drug Discov* **2011,** *10* (9), 685-97.

120. Macdonald, R. L.; Olsen, R. W., Gabaa Receptor Channels. *Annual Review of Neuroscience* **1994,** *17* (1), 569-602.

121. Davies, J. E., The Pharmacological Basis of Therapeutics. *Occupational and Environmental Medicine* **2007,** *64* (8), e2.

122. Fan, L.; Lewis, R. W.; Hess, G. P.; Ganem, B., A New Synthesis of Caged Gaba Compounds for Studying Gabaa Receptors. *Bioorganic & Medicinal Chemistry Letters* **2009,** *19* (14), 3932-3933.

123. Amatrudo, J. M.; Olson, J. P.; Lur, G.; Chiu, C. Q.; Higley, M. J.; Ellis-Davies, G. C. R., Wavelength-Selective One- and Two-Photon Uncaging of Gaba. *ACS Chemical Neuroscience* **2014,** *5* (1), 64-70.

124. Shi, D. D.; Trigo, F. F.; Semmelhack, M. F.; Wang, S. S. H., Synthesis and Biological Evaluation of Bis-Cnb-Gaba, a Photoactivatable Neurotransmitter with Low

Receptor Interference and Chemical Two-Photon Uncaging Properties. *Journal of the American Chemical Society* **2014,** *136* (5), 1976-1981.

125. Sternbach, L. H.; Reeder, E., Quinazolines and 1,4-Benzodiazepines. Ii.1 the Rearrangement of 6-Chloro-2-Chloromethyl-4-Phenylquinazoline 3-Oxide into 2-Amino Derivatives of 7-Chloro-5-Phenyl-3h-1,4-Benzodiazepine 4-Oxide. *The Journal of Organic Chemistry* **1961,** *26* (4), 1111-1118.

126. Gupta, P.; Khobragade, S. B.; Shingatgeri, V. M., Effect of Various Antiepileptic Drugs in Zebrafish Ptz-Seizure Model. *Indian J Pharm Sci* **2014,** *76* (2), 157-163.

127. Gebauer, D. L.; Pagnussat, N.; Piato, A. L.; Schaefer, I. C.; Bonan, C. D.; Lara, D. R., Effects of Anxiolytics in Zebrafish: Similarities and Differences between Benzodiazepines, Buspirone and Ethanol. *Pharmacol Biochem Behav* **2011,** *99* (3), 480-486.

128. Afrikanova, T.; Serruys, A.-S. K.; Buenafe, O. E. M.; Clinckers, R.; Smolders, I.; de Witte, P. A. M.; Crawford, A. D.; Esguerra, C. V., Validation of the Zebrafish Pentylenetetrazol Seizure Model: Locomotor Versus Electrographic Responses to Antiepileptic Drugs. *PLOS ONE* **2013,** *8* (1), e54166.

129. Löscher, W., Critical Review of Current Animal Models of Seizures and Epilepsy Used in the Discovery and Development of New Antiepileptic Drugs. *Seizure* **2011,** *20* (5), 359-368.

130. Baraban, S. C.; Taylor, M. R.; Castro, P. A.; Baier, H., Pentylenetetrazole Induced Changes in Zebrafish Behavior, Neural Activity and C-Fos Expression. *Neuroscience* **2005,** *131* (3), 759-68.

131. Cho, S.; Wood, A.; Bowby, M. R., Brain Slices as Models for Neurodegenerative Disease and Screening Platforms to Identify Novel Therapeutics. *Curr Neuropharmacol* **2007,** *5* (1), 19-33.

132. Kimmel, C. B.; Ballard, W. W.; Kimmel, S. R.; Ullmann, B.; Schilling, T. F., Stages of Embryonic Development of the Zebrafish. *Developmental Dynamics* **1995,** *203* (3), 253-310.